



Evolved Climates and Observational Discriminants for the TRAPPIST-1 Planetary System

Andrew P. Lincowski^{1,2}, Victoria S. Meadows^{1,2}, David Crisp^{2,3}, Tyler D. Robinson^{2,4}, Rodrigo Luger^{1,2}, Jacob Lustig-Yaeger^{1,2}, and Giada N. Arney^{2,5}

¹ Department of Astronomy and Astrobiology Program, University of Washington, Box 351580, Seattle, Washington 98195, USA; alinc@uw.edu

² NASA Astrobiology Institute's Virtual Planetary Laboratory, Box 351580, University of Washington, Seattle, WA 98195, USA

³ Jet Propulsion Laboratory, California Institute of Technology, Earth and Space Sciences Division, Pasadena, CA 91011, USA

⁴ Department of Physics and Astronomy, Northern Arizona University, Flagstaff, AZ 86011, USA

⁵ NASA/Goddard Space Flight Center, Greenbelt, MD 20771, USA

Received 2018 February 27; revised 2018 September 17; accepted 2018 September 19; published 2018 November 1

Abstract

The TRAPPIST-1 planetary system provides an unprecedented opportunity to study terrestrial exoplanet evolution with the *James Webb Space Telescope (JWST)* and ground-based observatories. Since M dwarf planets likely experience extreme volatile loss, the TRAPPIST-1 planets may have highly evolved, possibly uninhabitable atmospheres. We used a versatile, 1D terrestrial planet climate model with line-by-line radiative transfer and mixing length convection (VPL Climate) coupled to a terrestrial photochemistry model to simulate environmental states for the TRAPPIST-1 planets. We present equilibrium climates with self-consistent atmospheric compositions and observational discriminants of postrunaway, desiccated, 10–100 bar O₂- and CO₂-dominated atmospheres, including interior outgassing, as well as for water-rich compositions. Our simulations show a range of surface temperatures, most of which are not habitable, although an aqua planet TRAPPIST-1 e could maintain a temperate surface given Earth-like geological outgassing and CO₂. We find that a desiccated TRAPPIST-1 h may produce habitable surface temperatures beyond the maximum greenhouse distance. Potential observational discriminants for these atmospheres in transmission and emission spectra are influenced by photochemical processes and aerosol formation and include collision-induced oxygen absorption (O₂–O₂), and O₃, CO, SO₂, H₂O, and CH₄ absorption features, with transit signals of up to 200 ppm. Our simulated transmission spectra are consistent with *K2*, *Hubble Space Telescope*, and *Spitzer* observations of the TRAPPIST-1 planets. For several terrestrial atmospheric compositions, we find that TRAPPIST-1 b is unlikely to produce aerosols. These results can inform *JWST* observation planning and data interpretation for the TRAPPIST-1 system and other M dwarf terrestrial planets.

Key words: planets and satellites: atmospheres – planets and satellites: detection – planets and satellites: individual (TRAPPIST-1) – planets and satellites: terrestrial planets

1. Introduction

M dwarfs are the most common type of star (Henry et al. 2006), with a high occurrence rate of both multiplanet systems (e.g., Ballard & Johnson 2016; Gillon et al. 2017) and Earth-sized planets in the habitable zone (Dressing & Charbonneau 2015). Here, we define the classical habitable zone (HZ) as that region around the star where a planet with an Earth-like environment could maintain liquid water on its surface (Kasting et al. 1993). Consequently, M dwarfs host the most HZ planets of any stellar type by a large margin and are therefore key to understanding the broader evolution of HZ terrestrial planets and the distribution of life beyond the solar system. Although numerous, M dwarf HZ planets likely face significant challenges to habitability, as their parent stars exhibit high stellar activity (Tarter et al. 2007) and intense, protracted stellar evolution (Baraffe et al. 2015). These stellar characteristics could strip the primordial atmosphere and cause significant volatile loss (Khodachenko et al. 2007; Lammer et al. 2007, 2011; Luger & Barnes 2015; Luger et al. 2015; Tian 2015; Ribas et al. 2016; Airapetian et al. 2017; Dong et al. 2017; Garcia-Sage et al. 2017) or destroy ozone, which

can protect exposed life on the surface from UV radiation (Segura et al. 2010). In particular, the superluminous pre-main-sequence phase of an M dwarf could drive an ocean-bearing terrestrial planet into a runaway greenhouse state for hundreds of millions of years until the planet enters the habitable zone, as the star dims and enters the main sequence (Luger & Barnes 2015; Meadows et al. 2018a).

Determining whether these abundant M dwarf HZ planets are in fact habitable is therefore a key focus in astrobiology and exoplanet science (see, e.g., Shields et al. 2016; Meadows et al. 2018a, for reviews). M dwarf terrestrial planets are likely to experience very different evolutionary paths compared to those in our solar system. Their HZ planets may therefore have atmospheres that have evolved considerably from their primordial composition. Reflecting their extreme evolution, these atmospheres may not be Earth-like or N₂-dominated, and the planets may not be habitable (Meadows et al. 2018a).

Soon the targets and technical capabilities will be available that are needed to observe M dwarf planets, detect and characterize their atmospheric compositions, and search for signs of planetary evolution and habitability. Several planets that are likely to be terrestrial have been found orbiting M dwarfs, including within the habitable zone (Berta-Thompson et al. 2015; Anglada-Escudé et al. 2016; Dittmann et al. 2017; Gillon et al. 2017; Shvartzvald et al. 2017). Facilities available in the near future, such as the *James Webb Space Telescope (JWST)*



Original content from this work may be used under the terms of the [Creative Commons Attribution 3.0 licence](#). Any further distribution of this work must maintain attribution to the author(s) and the title of the work, journal citation and DOI.

and ground-based extremely large telescopes (ELTs), may be capable of probing M dwarf planetary atmospheres, including a handful of HZ planets (Rodler & López-Morales 2014; Cowan et al. 2015; Quanz et al. 2015; Snellen et al. 2015; Greene et al. 2016; Lovis et al. 2017). For the best targets, these facilities may have the precision required to undertake the first spectroscopic search for atmospheric water vapor and biosignature gases, such as O₂ and CH₄ (Des Marais et al. 2002; Rodler & López-Morales 2014; Catling et al. 2018; Fujii et al. 2018; Meadows 2017; Meadows et al. 2018b; Schwieterman et al. 2018; Walker et al. 2018).

The seven transiting planets of the nearby TRAPPIST-1 system provide a natural laboratory to study planetary atmospheric evolution and the associated impact on habitability. The semimajor axes of these planets' orbits encompass and extend beyond both the inner and outer boundaries of the habitable zone, enabling a test of evolutionary processes as a function of distance from the star. TRAPPIST-1 is a very-late-type M dwarf star (M8V; Liebert & Gizis 2006) and so is an ideal target for characterization with *JWST* because its planets have very-short-period orbits, facilitating repeated observations, and comparatively small star-to-planet size ratios, which increase the signal-to-noise ratio of transit observations. To plan and support the interpretation of these *JWST* observations, numerical models are being used to study the possible evolutionary pathways and resultant climates of these planets (Wolf 2017; Turbet et al. 2018), and to generate simulated thermal emission and transit transmission spectra (Morley et al. 2017). These models and simulated observations can be used to predict observable phenomena that may help discriminate between habitable and uninhabitable planetary environmental states and help identify the evolutionary processes that generated them.

Exoplanet models for H₂-dominated worlds (e.g., Miller-Ricci et al. 2009; Hu & Seager 2014) may not be applicable for small M dwarf planets, which may be more terrestrial in composition and are therefore likely to have solid or liquid surfaces and secondary outgassed (i.e., high molecular weight) atmospheres. There is growing evidence that the bulk properties of planets with radii $\lesssim 1.5R_{\oplus}$ are more similar to our solar system terrestrials than to sub-Neptune planets with H₂-dominated atmospheres (e.g., Rogers 2015; de Wit et al. 2016; Fulton et al. 2017; de Wit et al. 2018). The densities of nearby M dwarf HZ planets (e.g., GJ1132 b, $6.0 \pm 2.5 \text{ g cm}^{-3}$, Berta-Thompson et al. 2015; and LHS1140 b, $12.5 \pm 3.4 \text{ g cm}^{-3}$, Dittmann et al. 2017) are similar to or greater than the densities of Earth (5.5 g cm^{-3}) or Venus (5.3 g cm^{-3}), consistent with mixtures of silicate rock and iron. The TRAPPIST-1 planets have currently measured densities that span 0.6 to 1.0 times Earth's density (i.e., $3.3\text{--}5.5 \text{ g cm}^{-3}$; see Table 1). The generally lower densities of the TRAPPIST-1 planets (Gillon et al. 2017; Grimm et al. 2018), along with their resonant orbits, suggest migration (Luger et al. 2017b; Unterborn et al. 2018). If this is the case, they may have formed at larger distances from the star with a more volatile-rich composition.

If these small HZ M dwarf planets are terrestrial, considerable host star evolution and planetary migration processes may have caused changes in the bulk and atmospheric compositions, resulting in evolutionary paths unlike those seen in our solar system. For example, Ribas et al. (2016), Barnes et al. (2018), and Coleman et al. (2017) assessed evolutionary outcomes for a

single planet in the habitable zone of an M5.5 dwarf star, Proxima Centauri b. Their work suggests that these evolutionary paths could produce desiccated planets that rapidly lost their oceans by evaporation, photolysis, and subsequent hydrogen loss to space, leaving massive O₂-dominated atmospheres (Kasting 1995; Luger & Barnes 2015; Barnes et al. 2018) or runaway greenhouse conditions with CO₂-dominated atmospheres (i.e., Venus-like; Kasting 1995; Meadows et al. 2018a). The former hypothesized planetary environment assumes O₂ build-up as a result of the superluminous pre-main-sequence phase and subsequent water loss, with inefficient atmospheric loss or surface sinks for oxygen. Processes other than extreme ultraviolet (XUV)-driven hydrodynamic escape may cause O₂ loss, such as surface interactions (Hamano et al. 2013; Schaefer et al. 2016; Wordsworth et al. 2018) and nonthermal processes favoring ion escape (Collinson et al. 2016; Airapetian et al. 2017; Dong et al. 2017; Garcia-Sage et al. 2017). Our current understanding of the history of Venus suggests that oxygen loss may be efficient. If so, a CO₂-dominated atmosphere is also a likely case that may evolve from the loss processes that the TRAPPIST-1 planets may have experienced, since these planets could continue to outgas volatiles (Donahue & Pollack 1983), eventually producing Venus-like atmospheric conditions. These planets could also have migrated inward to their current positions (Luger et al. 2017a; Unterborn et al. 2018), which would have allowed primordial H₂ envelopes to be stripped by the young star to reveal a terrestrial core (Lammer et al. 2011; Luger et al. 2015) that may be volatile-rich and result in a more Earth-like H₂O- or N₂-rich atmosphere.

The stellar spectra of M dwarfs are redder and far more variable at UV wavelengths than those of G-type stars like the Sun. The combined effects of these spectral differences and planetary semimajor axis on the climate and chemistry for M dwarf terrestrial atmospheres have been previously explored in work that focused mostly on Earth-like planets in the habitable zone. Segura et al. (2005) modeled the effects of M dwarf stellar spectra on Earth-like atmospheres with incoming host-star stellar radiation (instellation) levels similar to Earth and found robust O₃ production and increased CH₄ levels. Grenfell et al. (2007) explored the effect of orbital semimajor axis on the atmospheric lifetime of biosignature gases and their detectability for Earth-like HZ planets around F-G-K stars, finding increased O₃ and CH₄ for larger semimajor axes. This trend is due both to colder temperatures at larger semimajor axes and to the reduction in radicals derived from H₂O photolysis, which destroys both O₃ and CH₄. More recently, comprehensive studies of Proxima Centauri b were undertaken by Turbet et al. (2016) using 3D general circulation models (GCMs) and by Meadows et al. (2018a) using 1D coupled climate-photochemical models. These studies provided a range of plausible atmospheric compositions and climates, including non-Earth-like cases, for planets in the HZ of M dwarfs.

There have been a number of efforts to model aspects of the TRAPPIST-1 planetary system that might affect habitability. These have included the effects of stellar evolution (Bolmont et al. 2017) and planet formation (Quarles et al. 2017). Planetary atmospheric models have been used to assess climate and atmospheric composition. Simple energy-balance climate models (EBMs) were used to assess the climate response to globally parameterized variables such as albedo and vegetation coverage (Alberti et al. 2017) and identified TRAPPIST-1 d as

Table 1
Stellar and Planetary System Parameters as Model Inputs for TRAPPIST-1

| Parameter | Modeled | Measured ^a | | | | | |
|--|---------------------------|--|---------------------------|---------------------------|---------------------------|---------------------------|---------------------------|
| Star | | TRAPPIST-1—2MASS J23062928-0502285 | | | | | |
| Magnitudes ^b | | $V = 18.80 \pm 0.08, R = 16.47 \pm 0.07, I = 14.0 \pm 0.1, J = 11.35 \pm 0.02, K = 10.30 \pm 0.02$ | | | | | |
| Mass (M_{\odot}) | | 0.0802 ± 0.0073 | | | | | |
| Radius (R_{\odot}) | 0.117 | 0.117 ± 0.0036 | | | | | |
| Luminosity (L_{\odot}) | 0.000524 | 0.000524 ± 0.000034 | | | | | |
| Effective temperature (K) | 2500 | $2,559 \pm 50$ | | | | | |
| Metallicity [Fe/H] | 0 | $+0.04 \pm 0.08$ | | | | | |
| Log g | 5 | 4.8 | | | | | |
| Planets ^a | b | c | d | e | f | g | h ^c |
| Period (days) | 1.510870 | 2.42182 | 4.0496 | 6.0996 | 9.2067 | 12.353 | 18.767 |
| Semimajor axis (au) | 0.01111 | 0.01521 | 0.02144 | 0.02817 | 0.0371 | 0.0451 | 0.0595 |
| Irradiation (S_{\odot}) | 4.245 | 2.265 | 1.140 | 0.6603 | 0.381 | 0.258 | 0.148 |
| Radius ^d (R_{\oplus}) | $1.121^{+0.032}_{-0.031}$ | $1.095^{+0.031}_{-0.030}$ | 0.784 ± 0.023 | $0.910^{+0.027}_{-0.026}$ | $1.046^{+0.030}_{-0.029}$ | $1.148^{+0.033}_{-0.032}$ | $0.773^{+0.027}_{-0.026}$ |
| Mass ^d (M_{\oplus}) | $1.107^{+0.143}_{-0.154}$ | $1.156^{+0.131}_{-0.142}$ | $0.297^{+0.035}_{-0.039}$ | $0.772^{+0.075}_{-0.079}$ | $0.934^{+0.078}_{-0.080}$ | $1.148^{+0.095}_{-0.098}$ | $0.331^{+0.049}_{-0.056}$ |
| Density ^d (ρ_{\oplus}) | $0.726^{+0.091}_{-0.092}$ | $0.883^{+0.078}_{-0.083}$ | $0.616^{+0.062}_{-0.067}$ | $1.024^{+0.070}_{-0.076}$ | $0.816^{+0.036}_{-0.038}$ | $0.759^{+0.033}_{-0.034}$ | $0.719^{+0.102}_{-0.117}$ |
| Gravity ^d (m/s^2) | 7.94 | 9.46 | 4.74 | 9.15 | 8.37 | 8.55 | 5.43 |
| Impact parameter b (R_{\ast}) | $0.126^{+0.092}_{-0.078}$ | $0.161^{+0.076}_{-0.084}$ | 0.17 ± 0.11 | $0.12^{+0.11}_{-0.09}$ | 0.382 ± 0.035 | 0.42 ± 0.031 | $0.45^{+0.06}_{-0.08}$ |

Notes. We use nominal values for our modeling. Error bars (1σ) are shown for reference. Standard errors on the period are smaller than the precision reported here. The error on the semimajor axis is approximately 3% of the quoted values. Irradiation is computed from the reported semimajor axis, assuming the luminosity quoted here. Gravity is given without error bars and is for the nominal values of mass and radius.

^a Data from Gillon et al. (2017) unless otherwise noted.

^b Data from Gillon et al. (2016).

^c Data from Luger et al. (2017b).

^d Data from Grimm et al. (2018).

the planet most likely to maintain surface water over a large range of albedo and vegetation parameters, with f, g, and h unlikely to host surface liquid water. To explore potential atmospheric states of the TRAPPIST-1 planets as a function of semimajor axis, Morley et al. (2017) distilled the bulk atmospheric compositions of Earth, Venus, and Titan into their lowest Gibbs free energy components using thermochemistry. They used this approximation to explore a broad parameter space of atmospheric pressures spanning 0.0001–100 bar, with prescribed atmospheric thermal profiles and surface temperatures adjusted to be consistent with planetary equilibrium temperatures for different assumed values of planetary Bond albedo. Morley et al. (2017) assessed the observational signatures of these atmospheres in transmission and emission and concluded that planet b would require fewer than 10 eclipse observations with *JWST/MIRI* to detect thermal emission and constrain the planetary emission temperature. They suggested that planets d–f could have surface liquid water and that their environments may be probed using *JWST* photometry. Wolf (2017) and Turbet et al. (2018) used 3D GCMs to model climates for HZ and outer TRAPPIST-1 planets with N_2 and pure CO_2 atmospheres and surface pressures up to 10 bar. In contrast with the EBM study (Alberti et al. 2017), Wolf (2017) concluded that only planet e resided within the classical habitable zone and that it would require substantially more CO_2 than Earth to maintain an Earth-like surface temperature. Turbet et al. (2018) assessed the outer planets and found that atmospheres consisting of N_2 , CO, or O_2 are resistant to collapse, even for synchronously rotating planets. They argued that greenhouse gases like CO_2 , NH_3 , and CH_4 would be difficult to maintain in the atmospheres of the TRAPPIST-1 planets after outgassing, due to easy condensation of CO_2 on the

night side and the likely photochemical destruction of NH_3 and CH_4 . They noted that if the planet started with larger amounts of CO_2 (>10 bar), then the greenhouse effect and heat redistribution would allow CO_2 to remain stable in the atmosphere. Turbet et al. (2018) agreed with Wolf that TRAPPIST-1 e has the highest potential for habitability, although they concluded that several bar of CO_2 would be sufficient for TRAPPIST-1 f and g to also support liquid surface water.

The above studies do not include photochemistry and are largely insensitive to the effect of TRAPPIST-1’s redder, more variable stellar spectrum on planetary atmospheric composition, which can be significant for terrestrial atmospheres at the range of instellation levels received by the TRAPPIST-1 planets (e.g., Segura et al. 2005, 2007; Grenfell et al. 2014; Meadows et al. 2018a). Without coupled climate–photochemistry models forced by the incoming stellar spectrum, it is not possible to obtain self-consistent solutions for planetary atmospheric composition and corresponding temperature structures. This could have large effects on predicted spectra, especially for emission spectra at MIR wavelengths, which are strongly dependent on the vertical temperature structure of the atmosphere.

To help guide and interpret current (e.g., de Wit et al. 2016, 2018; Delrez et al. 2018) and upcoming observations that will attempt to determine the nature of the TRAPPIST-1 exoplanetary environments, here we use self-consistent 1D coupled climate–chemistry models for terrestrial planets to explore the effects of stellar distance on atmospheric properties for a selection of possible environmental states. Given the stellar evolution of the host star, we suggest that evolved, post-ocean-loss or post-atmospheric-loss states may be more likely for the TRAPPIST-1 planets than Earth-like atmospheres. Specifically, we model the atmospheric composition and

climate of all seven TRAPPIST-1 planets for postrunaway O₂- and CO₂-dominated atmospheres, with and without continuous outgassing and for surface pressures up to 100 bar. For comparison, we also model an Earth-like, ocean-covered environment (aqua planet) for TRAPPIST-1 e only.

Our climate, photochemistry, and radiative transfer models were developed specifically for terrestrial planets with secondary outgassed atmospheres. They have been validated against solar system planets (Meadows & Crisp 1996; Tinetti et al. 2005; Robinson et al. 2011; Arney et al. 2014; Robinson & Crisp 2018) and have been used to model O₂- and CO₂-based atmospheric compositions for Proxima Centauri b (Meadows et al. 2018a). Together, these models explicitly account for the photochemical and climate impacts of the redder, more active stellar spectrum. We consider initial atmospheric compositions that may plausibly result from evolutionary processes, with Earth-like outgassing rates and a range of volatile inventory levels. These atmospheres are then iterated forward in time until they reach coupled climate–photochemical equilibrium. We then use a line-by-line radiative transfer model to generate high-spectral-resolution transmission, emission, and reflectance spectra of the resulting planetary states, which may be used as forward-model predictions for upcoming observations with *JWST*, ground-based telescopes, and a future direct-imaging mission such as the Habitable Exoplanet Imaging Mission (HabEx) or Large UV/Optical/IR surveyor (LUVOIR) concepts. From these synthetic spectra, we identify observable properties of these highly evolved atmospheres that may be used to discriminate among these environments. For TRAPPIST-1 e, we determine whether a potentially habitable atmosphere could be detected and discriminated from possible desiccated atmospheres. These evolutionary and spectral studies may also inform target selection for other late M dwarf systems, including planets yet to be discovered by the Transiting Exoplanet Survey Satellite (TESS; Sullivan et al. 2015).

In Section 2, we give a description of our coupled climate–photochemical and atmospheric escape modeling suite, along with necessary input data. In Section 3, we present the results of our atmospheric escape calculations, which inform the results of coupled climate–chemistry simulations of several different atmospheric compositions, and the associated simulated direct-imaging and transmission spectra. In Section 4, we discuss the significance of the atmospheric escape results and the associated oxygen produced, discuss the climate–photochemistry results, identify observational discriminants for the modeled environments, compare our results with other recent work, and assess recent observations. We summarize our findings in Section 5. Detailed descriptions of our climate–photochemical models and their validations are given in the appendices.

2. Model and Input Descriptions

At the core of our simulations of the TRAPPIST-1 planetary environments and spectra is a 1D coupled climate–chemistry model, which we use to calculate climate–photochemical states that are self-consistent with the spectrum of the host star. As input to this model, we use an atmospheric escape and evolution model to determine likely surface volatile inventories and initial O₂ abundance as a function of semimajor axis. These models inform the initial assumptions for the present-day atmospheric composition used by the coupled climate–photochemical model. The self-consistent environments generated by the coupled

climate–photochemical model are used by our radiative transfer model to generate synthetic spectra as an aid to predicting observational discriminants for these different environmental outcomes.

Specifically, we use a 1D terrestrial radiative–convective equilibrium climate model, VPL Climate, which is capable of modeling the wide variety of potential atmospheres for these planets and can implement stellar types very different from the Sun. VPL Climate has been validated against Venus, Earth, and Mars (Robinson & Crisp 2018) and integrates SMART (Meadows & Crisp 1996; Crisp 1997) as its radiative transfer core, the same line-by-line radiative transfer code we use to generate high-resolution spectra. Here, we couple this new climate model to a 1D atmospheric chemistry model that has been used in a variety of terrestrial exoplanet studies (e.g., Segura et al. 2005; Arney et al. 2016; Meadows et al. 2018a), which we update for this study (see Appendix B). We use an updated version of the atmospheric evolution model of Luger & Barnes (2015) to produce plausible inventories of oxygen accumulation that justify some of the posited environmental states we use in our climate–photochemical modeling. These models and their inputs are discussed in more detail below and in the appendices.

2.1. Radiative Transfer

We use the Spectral Mapping and Atmospheric Radiative Transfer code (SMART), originally developed by David Crisp (Meadows & Crisp 1996; Crisp 1997), for both high-resolution spectra and within the climate model to compute radiative fluxes and heating rates. SMART is capable of producing accurate synthetic planetary spectra (e.g., Robinson et al. 2011). SMART uses the Discrete Ordinate Radiative Transfer code (DISORT; Stamnes et al. 1988, 2000) to numerically compute the radiation field. SMART can combine the radiative fluxes from overlapping stellar and thermal sources and includes the extinction in each layer from absorbing gases (due to visible-to-far-infrared vibrational–rotational transitions, collision-induced absorption, and UV predissociation bands), Rayleigh scattering, cloud and aerosol scattering, a wavelength-dependent surface albedo, and a stellar source spectrum. We also use SMART to produce transit transmission spectra, including refraction (Robinson 2017).

2.2. The Climate Model

We use VPL Climate, a general-purpose, 1D radiative–convective equilibrium, terrestrial planet climate model (Meadows et al. 2018a; Robinson & Crisp 2018). This model uses SMART for rigorous spectrum-resolving (line-by-line) radiative transfer, coupled to a mixing-length convection parameterization. As input, VPL Climate requires an initial atmospheric state (consisting of a temperature profile and gas mixing ratios), physical parameters, and fundamental laboratory and experimental data.

We use a 1D coupled climate–photochemical model in this work, rather than a 3D GCM, to more rigorously and self-consistently explore both the radiative and photochemical effects of the TRAPPIST-1 stellar spectrum on atmospheric composition and climate for non-Earth-like terrestrial planet atmospheres. For Proxima Centauri b, Meadows et al. (2018a) performed a 1D climate comparison with the 3D GCM results

of Turbet et al. (2016) and demonstrated that differences in globally averaged temperatures between 1D and 3D models were small. For N₂- and CO₂-dominated atmospheres, the difference was less than 20 K when the planet was synchronously rotating, and 5 K or less when the planet was in a 3:2 spin-orbit resonance state. In slower, synchronously rotating planets, enhanced day-night temperature contrasts (which cannot be spatially resolved by 1D models) may induce atmospheric collapse (Turbet et al. 2016, 2018). However, even if synchronously rotating, the TRAPPIST-1 planets, with orbital periods of 1.5–19 days, are in an orbital regime closer to rapid rotators, with the possibility of sufficient Coriolis force to drive zonal circulation and help prevent atmospheric collapse (Yang et al. 2014; Kopparapu et al. 2016). For the desiccated planets that we model here, we also assume dense (≥ 10 bar) atmospheres that will have smaller day-night contrast and are more likely to be stable against collapse (Hu & Yang 2014; Meadows et al. 2018a; Turbet et al. 2018). Although our habitable planet example for TRAPPIST-1 e has only a 1 bar atmosphere, Hu & Yang (2014) showed that day-night temperature contrasts for synchronously rotating planets with oceans were much smaller when a full dynamical ocean model, which strongly augments atmospheric heat transport, was used in a 3D GCM. With a dynamical ocean, even a relatively thin atmosphere was more stable against collapse.

The VPL Climate model components are summarized below and described in more detail in Appendix A. The inputs are described in Section 2.6.

2.3. Atmospheric Chemistry Model

To self-consistently model the effects of M dwarf host-star UV radiation on our modeled atmospheres, we couple VPL Climate to a publicly available atmospheric chemistry model.⁶ This code is based on Kasting et al. (1979) and Zahnle et al. (2006) and can simulate a range of planetary redox states, including high-oxygen atmospheres (Arney et al. 2016; Schwertner et al. 2016; Meadows et al. 2018a). This photochemical model is described in detail in Meadows et al. (2018a). Briefly, it divides the nominal model atmosphere into plane-parallel layers and assumes hydrostatic equilibrium. A vertical transport scheme includes molecular and eddy diffusion. Boundary conditions can be set for all species at the top and bottom of the atmosphere, including initial gas mixing ratios, outgassing fluxes, and surface deposition velocities. We describe the specific boundary conditions for each type of atmosphere in Section 3.

Here, we updated the photochemistry model by extending the photochemically active wavelength range considered by the model to include Ly α for a wide range of species. Updates to the model are described in Appendix B, and validations for Earth and Venus are given in Appendix C.

2.4. Coupled Climate–Chemistry Model Convergence

The climate and chemistry models can be run independently or as a coupled model. When the climate model is run independently, the convergence criterion is met when all atmospheric layers are flux-balanced within 1 W m⁻² and the heating rate for each layer is less than 10⁻⁴ K per day. When run independently, the atmospheric chemistry model tracks

changes in gas concentrations in each time step and computes the relative error. It adjusts the next time step based on the largest error. The model checks the time step length, and when it reaches 10¹⁷ s in less than ~ 100 time steps, we consider the model to be converged.

To run coupled climate–photochemistry experiments, we pass the converged profile from VPL Climate (temperature and gas mixing profiles) to the chemistry code, which is run to convergence. The modified gas mixing ratios from the chemistry code are then passed back to VPL Climate to compute a new equilibrium temperature structure and condensable gas mixing profiles. These profiles are then passed back to the chemistry model, and this process is repeated until global convergence is achieved.

2.5. Atmospheric Escape Model

Plausible upper limits of water and oxygen inventories of postrunaway atmospheres are modeled using the atmospheric escape framework introduced by Luger et al. (2015) and Luger & Barnes (2015). Briefly, we compute the XUV-driven, energy-limited escape rate of hydrogen modified by the hydrodynamic drag of oxygen as in Hunten (1973), assuming photolysis is fast enough that it is not the rate-limiting factor. As in Luger & Barnes (2015), we assume surface sinks are inefficient at removing photolytically produced oxygen, yielding a strict upper bound on the amount of oxygen retained in the atmosphere. Unlike Luger & Barnes (2015), we model the decrease in the efficiency of the flow due to the increase in the mixing ratio of oxygen, which causes the flow to transition to diffusion-limited escape (Schaefer et al. 2016). We also relax the assumption of constant escape efficiency ϵ_{xuv} , instead modeling it as a function of the incident XUV flux as in Bolmont et al. (2017). For the TRAPPIST-1 planets, ϵ_{xuv} varies between about 0.01 (at high XUV flux) and 0.10 (at moderate XUV flux).

2.6. Model Inputs

Our climate, photochemical, and atmospheric escape models require a number of inputs that tailor the model to the planetary atmosphere studied. Inputs include planetary properties (e.g., orbit and radius), atmospheric gas mixing ratios for each constituent in each layer, gas absorption properties (i.e., cross section data and line lists), thermodynamic data for condensable gases, particle optical properties for aerosols, wavelength-dependent surface albedo data, and stellar spectral energy distribution (SED), including an estimate of total XUV flux over time.

2.6.1. Planetary Properties and Model Atmospheres

Here we adopt the current best-fit orbital periods, radii, and masses of the TRAPPIST-1 planets (see Table 1 and Gillon et al. 2016, 2017; Luger et al. 2017b; Grimm et al. 2018). We assume the planets are in fixed, circular orbits. For all seven known planets, we simulate post-runaway-greenhouse, O₂-dominated atmospheres with and without continuous outgassing and Venus-like CO₂-dominated atmospheres. These atmospheres are modeled with surface pressures of 10 and 100 bar for O₂-dominated cases and 10 and 92.1 bar (surface pressure of Venus) for Venus-like cases. We also model a potentially habitable aqua planet for TRAPPIST-1 e for comparison, both with the uninhabitable cases that we present

⁶ <https://github.com/VirtualPlanetaryLaboratory/atmos>

here and with other studies of TRAPPIST-1 planetary climates (Wolf 2017; Turbet et al. 2018) and observables (Morley et al. 2017). The particulars of each case are presented in detail in Section 3.

The nominal planetary atmospheres are one-dimensional and plane-parallel, consisting of 64 pressure levels, half of which are linear intervals of pressure from the surface to 10% of surface pressure, followed by logarithmic spacing in pressure to 0.01 Pa at the top of the atmosphere.

2.6.2. Gas Absorption Data

Gas absorption cross sections are calculated from three sources: vibrational–rotational transitions at visible and infrared wavelengths, continuum absorption from electronic transitions and predissociation bands at UV wavelengths, and dimer- and pressure-induced absorption bands at visible to infrared wavelengths. Absorption lines associated with vibrational–rotational transitions are calculated using the line-by-line model LBLABC (see Appendix A) with the HITRAN2012, HITEMP2010, or Ames line databases (Rothman et al. 2013, 2010; Huang et al. 2017). These line lists assume Earth-like isotopic abundances. We include foreign broadening by the dominant gases in the atmosphere (CO_2 , N_2 , or O_2).

Collision-induced absorption data are used for CO_2 – CO_2 (Moore 1972; Kasting et al. 1984; Gruszka & Borysow 1997; Baranov et al. 2004; Wordsworth et al. 2010; Lee et al. 2016), N_2 – N_2 (Schwieterman et al. 2015 based on Lafferty et al. 1996), and O_2 – O_2 (Greenblatt et al. 1990; Hermans et al. 1999; Maté et al. 1999).

UV–visible cross section data are incorporated from a variety of primary sources available from the MPI-Mainz UV/VIS Spectral Atlas of Gaseous Molecules of Atmospheric Interest⁷ (Keller-Rudek et al. 2013). Updated sources are listed in Appendix B.

2.6.3. Aerosol Optical Properties

The single-scattering optical properties of clouds and aerosols are defined in precomputed tables for a range of specific particle types. Each particle type is defined by its composition, its associated wavelength-dependent refractive indices, and its particle size and shape distributions. Given these properties, a single-scattering model is used to compute the wavelength-dependent extinction and scattering efficiencies (Q_{ext} and Q_{abs}) and the phase function moments (for Mie scattering) or the particle asymmetry parameter (g for some nonspherical particles) used in our radiative transfer calculations.

For the cloudy aqua planet, we specify Earth-like cirrus (water–ice) and stratocumulus (liquid water) clouds, each of cumulative optical depth $\tau = 5$. For cirrus clouds, the optical properties from B. Baum’s Cirrus Optical Property Library (Baum et al. 2005)⁸ are used. The particles consist of a distribution of 45% solid columns, 35% plates, and 15% 3D bullet rosettes, spanning 2–9500 μm with a cross section weighted mean diameter of 100 μm . Stratocumulus cloud optical properties are based on refractive indices of water from Hale & Querry (1973) and calculated using Mie scattering,

with a two-parameter gamma distribution ($a = 5.3$, $b = 1.1$) and mean particle radius 4.07 μm .

For Venus-like sulfuric acid aerosols, we use refractive indices for a range of specific acid concentrations between 25% and 100% from Palmer & Williams (1975). The sulfuric acid concentration is computed assuming vapor pressure equilibrium of the H_2O and H_2SO_4 gases with the condensed solution. The effective optical properties are then calculated by spline interpolation of the tables. Our photochemical model calculates the monodisperse aerosol radii at every atmospheric layer given the coagulation, sedimentation, and diffusion timescales (see, e.g., Pavlov et al. 2001) in phase equilibrium. For climate and spectral modeling, we convert the monodisperse distributions into log-normal distributions with the modal radii equal to the monodisperse particle radii and geometric standard deviation equal to 0.25, similar to the particle distribution findings for individual Venus aerosol modes as described in Crisp (1986). The differential optical depth profile used in the radiative transfer calculations for each planet is calculated from the log-normal distribution, assuming that the total mass in each layer is the same as in the monodisperse distribution. The optical depth $d\tau$ is calculated by

$$d\tau = dz \int_{R_{\min}}^{R_{\max}} \pi r^2 Q_{\text{ext}}(\lambda, r) n(r) dr, \quad (1)$$

where Q_{ext} is the extinction efficiency at a reference wavelength and n is the number density distribution.

2.6.4. Thermodynamic Data

The thermodynamic data required for condensables in VPL Climate (e.g., H_2O) consist of saturation vapor temperature, pressure, and enthalpy of formation. For water, above 273 K we use data sourced from NIST.⁹ Below 273 K, we use the saturation vapor temperature and pressure from Wagner et al. (1994). The enthalpy of condensation is from a fit to data provided in Rogers & Yau (1989). For sulfuric acid (H_2SO_4), we use a fit calculated by Gao et al. (2015, see references therein).

2.6.5. Surface Spectral Albedo

We use different surface compositions based on the type of climate we are simulating. Basalt was used for the volcanic Venus-like planets, and a desert surface (primarily kaolinite) was used for the post-ocean-loss O_2 -dominated atmospheres. For the aqua planet, we used open ocean. Surface reflectance data are from the U.S.G.S. spectral library (Clark et al. 2007),¹⁰ except for the ocean longward of 2 μm , which is from the ASTER spectral library (Baldridge et al. 2009)¹¹ (see Figure 1). The integrated, energy-flux-weighted surface albedos for these surfaces for our TRAPPIST-1 stellar spectrum are 0.09 (basalt), 0.37 (desert), and 0.02 (ocean). For comparison, this albedo for snow used in the VPL Spectral Earth Model (Robinson et al. 2011) is 0.16.

⁹ <http://webbook.nist.gov/chemistry/fluid/>

¹⁰ <http://speclab.cr.usgs.gov/spectral.lib06>

¹¹ <https://speclib.jpl.nasa.gov/>

⁷ http://satellite.mpic.de/spectral_atlas

⁸ http://www.ssec.wisc.edu/~baum/Cirrus/Solar_Spectral_Models.html

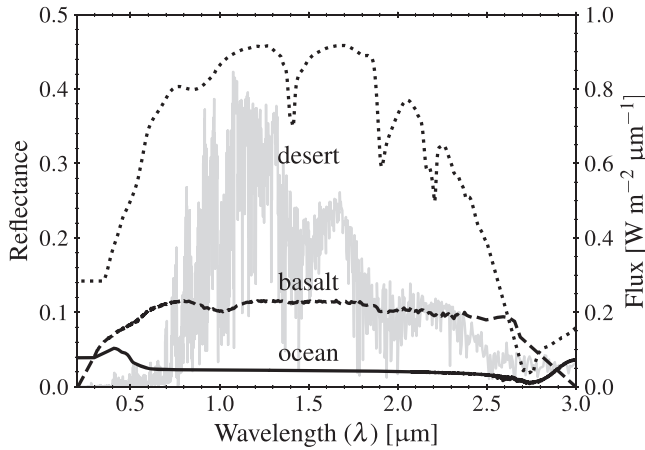


Figure 1. Wavelength-dependent surface reflectance for modeled planetary environments with stellar irradiation plotted for comparison. The desert surface is primarily kaolinite and was used for the desiccated O₂-dominated climates. The basaltic surface was used for Venus-analog climates. The ocean surface was used for the habitable aqua planet. These data are from the U.S.G.S. spectral library (Clark et al. 2007, see footnote 10), except for the ocean longward of 2 μm, which is from the ASTER spectral library (Baldridge et al. 2009, see footnote 11).

2.6.6. Stellar Spectra

Characterizing the climate and computing spectra require the stellar spectrum of TRAPPIST-1 (2MASS J23062928-0502285). The available data on this star in the UV to IR are limited to photometry and to measurements of Ly α from the *Hubble Space Telescope* (Bourrier et al. 2017). TRAPPIST-1 has an effective temperature of 2559 ± 50 K, [Fe/H] = 0.04 ± 0.08 , $M_* = 0.0802 \pm 0.0073 M_\odot$, and $R_* = 0.117 \pm 0.0036 R_\odot$ (Gillon et al. 2017). To model the panchromatic UV–NIR stellar spectrum necessary for line-by-line climate-photochemical modeling, we use the 2500 K, [Fe/H] = 0.0, log g = 5.0 spectral model of the PHOENIX v2.0 spectral database, which spans from 0.25 to 5.5 μm and has been shown to faithfully reproduce the visible–NIR spectra of M dwarfs (France et al. 2013). We compared this PHOENIX model to the photometric observations (Gillon et al. 2016) and found that the model SED, binned to available photometric bands, is within 3σ .

The intensity and wavelength dependence of the stellar UV spectrum is a critical factor affecting atmospheric chemistry and the subsequent atmospheric composition and climate. For example, Grenfell et al. (2007) noted changes in the atmospheres of planets around F-G-K stars as a function of orbital distance, including the impact of outgassed species on climate, while Grenfell et al. (2014) noted that UV changes within 200–350 nm have the largest effect on ozone levels for planets around late-type M dwarfs. In the absence of complete UV observations of TRAPPIST-1, we fit a UV spectrum compiled for Proxima Centauri (Meadows et al. 2018a). We scaled Proxima’s UV spectrum to the Ly α flux ratio of TRAPPIST-1 to Proxima Centauri, a factor of one-sixth at 1 au (Bourrier et al. 2017). The UV flux was stitched to the PHOENIX SED at around 0.3 μm, where photospheric emission began to dominate (i.e., where the flux from the PHOENIX model began to rise above the UV). This method provides only a possible UV flux environment for the planets of TRAPPIST-1 and does not represent the star’s actual activity (except the reconstructed Ly α). Given the variable activity of M dwarfs, UV observations of TRAPPIST-1 are needed to properly

characterize its planets. Our compiled spectrum is shown in Figure 2 and is available for download online using the VPL Spectral Explorer.¹²

2.6.7. XUV Flux

We model the evolution of stellar XUV luminosity as in Luger & Barnes (2015). We use the power law of Ribas et al. (2005) with exponent $\beta = -1.23$, a saturation fraction $L_{\text{xuv}}/L_{\text{bol}} = 2.5 \times 10^{-4}$ (based on the measurements of Wheatley et al. 2017), and a saturation time of 1 Gyr. We use the Baraffe et al. (1998) stellar evolution tracks to model the pre-main-sequence phase of TRAPPIST-1 and the habitable zone boundaries of Kopparapu et al. (2013) to decide whether the planets are experiencing hydrogen escape, as in Luger & Barnes (2015). Like Schaefer et al. (2016), we assume energy-limited escape transitions to diffusion-limited escape due to the accumulation of oxygen atoms.

3. Results

We first describe the potential atmospheric evolution, including water loss and oxygen production, for the seven TRAPPIST-1 planets due to the pre-main-sequence evolution of their host star. These results inform our chosen O₂ levels for the subsequent environmental modeling. We present calculated climates and compositions for O₂- and CO₂-dominated atmospheres and their spectra and observational discriminants. To span plausible pressure and compositional ranges for these evolved atmospheres, we model 10 and 100 bar O₂-dominated atmospheres, with and without trace constituents due to surface outgassing or volatile delivery; and 10 and 92.1 bar CO₂-dominated Venus-like atmospheres, with and without Venus-like haze/cloud aerosols. As a potentially habitable comparison case, we also calculate climate and trace composition of a 1 bar atmosphere for an ocean-covered TRAPPIST-1 e aqua planet. We show simulated pressure–temperature structures and mixing ratio profiles. A summary of our experiments is shown in Table 2.

A number of assumptions underlie our modeling in this work. Our atmospheres are assumed to be in hydrostatic equilibrium, though hydrodynamic processes could be occurring on planets b, c, and d, inward of the inner edge of the habitable zone. We assume the modeled atmospheres are stable against collapse on the night side, due to sufficiently high atmospheric mass (10–100 bar) to reduce day–night temperature contrasts (Turbet et al. 2018) or ocean circulation for the 1 bar aqua planets (Hu & Yang 2014). We assume these planets began in a warm state due to the superluminous pre-main-sequence phase, and that their secondary atmospheres were formed during this time. We ignore ion and particle effects, though these nonthermal processes may be important drivers of atmospheric loss (Airapetian et al. 2017; Garcia-Sage et al. 2017) and atmospheric chemistry (Segura et al. 2010; Airapetian et al. 2017; Tilley et al. 2017). The recent densities inferred from transit timing variation (TTV) measurements by Grimm et al. (2018) currently indicate planets with high volatile content, perhaps with the exception of planet e, which suggests that the most desiccated atmospheres are less probable and supports ocean-bearing surfaces or large outgassing fluxes. However, the error bars on the planet densities remain quite

¹² <http://depts.washington.edu/naipl/content/vpl-spectral-explorer>

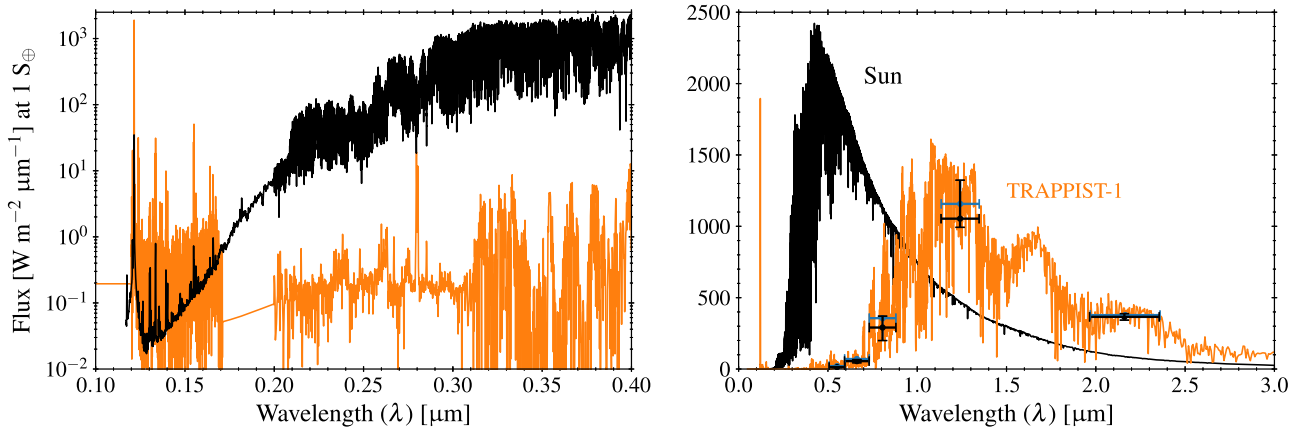


Figure 2. Input stellar spectral energy distribution (shown in orange) for TRAPPIST-1, an M8V star (Liebert & Gizis 2006), using the PHOENIX v2.0 spectral database (France et al. 2013), normalized to $1S_{\oplus}$. The UV is from Proxima Centauri (Meadows et al. 2018a), scaled to the measured Ly α flux (Bourrier et al. 2017). The solar spectrum is shown in black for comparison. Photometric bands (VRIJK) are shown as points with error bars (black are from Gillon et al. 2016; blue are band-integrated PHOENIX model fluxes), where the horizontal bars are the FWHM of the filter bands, and the observed flux errors are 3σ . Late-type M dwarf stars like TRAPPIST-1 have different effects on planetary photochemistry and climate than G-type stars, due to the different UV flux distribution and energy peak in the NIR. These spectra are available online using the VPL Spectral Explorer (see footnote 12) or upon request.

large and do not rule out more refractory compositions, supporting the possibility of desiccated atmospheres.

3.1. Atmospheric Escape and Oxygen Build-up

To determine plausible oxygen inventories for our O₂-dominated atmospheres, we computed the loss of hydrogen and oxygen during the pre-main-sequence phase of TRAPPIST-1 (see Figure 3). The maximum initial water inventory considered was 20 Earth oceans (by mass), the approximate maximum ocean loss for planets b, c, and d under our assumptions. Planets e, f, and g may each lose between three and six Earth oceans of water, while h may lose less than one ocean. This ocean loss results in the generation of dense O₂ atmospheres with maximum pressures (assuming no sinks) from 22 to 5000 bar.

The amount of water each planet may have lost and the subsequent surface pressure of atmospheric oxygen vary due to instellation, atmospheric scale height, and planetary surface area. The degree of H₂O loss is a strong function of instellation and time spent interior to the HZ inner edge. For example, as the host star dims, within 50–400 Myr after formation, planets h, g, f, and e successively enter the habitable zone and cease to lose significant amounts of H₂O, while planets b, c, and d continue to lose H₂O (Figure 3). Although the orbits (and levels of instellation received) for these planets are well spaced in resonance chains (Luger et al. 2017b), they exhibit variations in H₂O loss not related to their instellation levels. Under diffusion-limited escape, we assume that H₂O loss is proportional to the inverse of scale height (Hunten 1973), which is in turn proportional to temperature and inversely proportional to gravity and mean molecular mass. The small variations in H₂O loss among b–d and e–h are in part due to the different scale heights for each planet.

In comparison to ocean loss, the resultant surface pressure of equivalent atmospheric oxygen generated by water photolysis does not show a similar increasing trend with instellation; the sequence we calculated for the TRAPPIST-1 system (from highest to lowest O₂ surface pressure) is c, d, b, e, g, f, h. Compared to planet b, c loses similar amounts of H₂O and is similar in size, but because c has a much larger mass and

stronger surface gravity, it builds up a higher surface pressure of equivalent atmospheric O₂. That is, c can accrue a similar mass of remaining O₂, but the stronger surface gravity results in a larger surface pressure (since surface pressure is the product of surface gravity and the integrated atmospheric mass per unit area). The sequence of e, g, f, and h is also affected by each planet’s respective gravitational acceleration, as opposed to an effect of radius; while f and g are similar in radius, their nominal surface gravities are very different, which results in a higher surface pressure of oxygen for g.

3.2. Planetary Environmental States

In the following subsections, we describe our input assumptions and resultant environmental states (atmospheric temperature profiles as a function of pressure, and vertical profiles of principal atmospheric constituent abundances) for each atmosphere. Globally averaged surface temperatures for all modeled climates are given in Figure 4, and O₃ column densities are given in Table 3.

3.2.1. O₂-dominated Atmospheres: Desiccated

In Figure 5, we present environmental states for completely desiccated, oxygen-dominated atmospheres for the seven TRAPPIST-1 planets, assuming 10 or 100 bar of surface pressure. These surface pressure values were chosen as representative of possible states, because although TRAPPIST-1’s pre-main-sequence evolution may produce up to thousands of bar of O₂ in the most extreme case (Figure 3), much of this O₂ is likely to be reincorporated into the land surface, ocean, lithosphere, or mantle (e.g., Hamano et al. 2013; Schaefer et al. 2016; Wordsworth et al. 2018) or, depending on each planet’s magnetic field, lost to nonhydrodynamic, top-of-atmosphere processes over time (e.g., Khodachenko et al. 2007; Lammer et al. 2007, 2011; Ribas et al. 2016), such as the “electric wind” on Venus (Collinson et al. 2016). While an abiotic O₂-dominated planetary atmosphere has yet to be discovered, and Venus does not retain significant quantities of atmospheric oxygen, it may be possible to test the existence of this hypothesized ocean-loss-generated atmosphere with JWST.

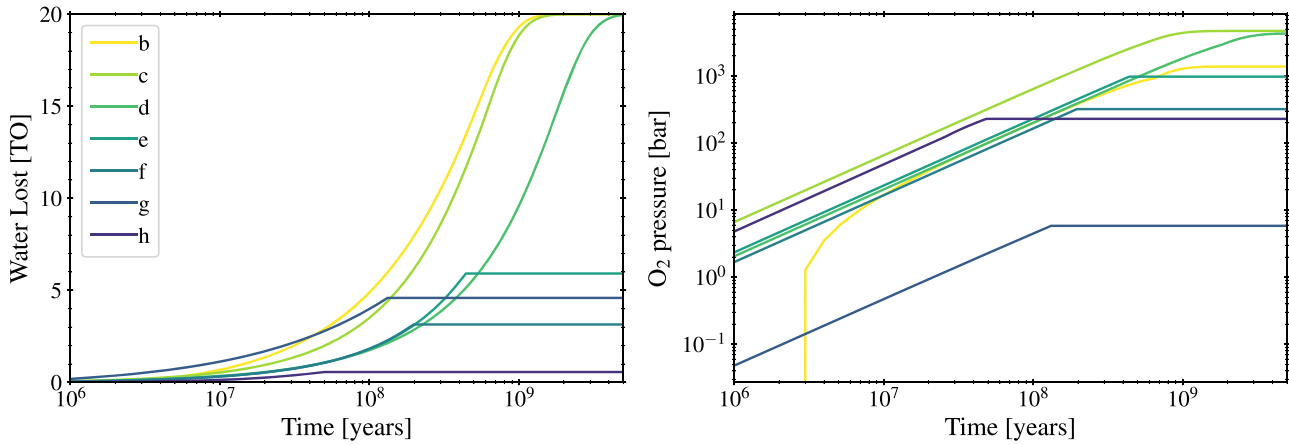


Figure 3. Computed pre-main-sequence evolution of water loss and oxygen production for the TRAPPIST-1 planets assuming inefficient surface sinks. These results represent the maximum build-up of oxygen in the atmosphere. The maximum ocean inventory assumed was 20 Earth oceans, all of which may be lost for planets b, c, and d. Planet h may lose less than one ocean of water.

Table 2
Modeled Planetary States and Their Environmental Parameters

| Planetary state | Surface | Clouds | Gases | Surface pressure |
|-----------------------------|---------|--------------------------------|--|------------------|
| Aqua planet, clear sky | Ocean | None | 80% N ₂ , 20% O ₂ , trace H ₂ O, CO ₂ , SO ₂ , H ₂ S, OCS, NO, CH ₄ | 1 bar |
| Aqua planet, cloudy | Ocean | 50% water, 50% ice | 80% N ₂ , 20% O ₂ , trace H ₂ O, CO ₂ , SO ₂ , H ₂ S, OCS, NO, CH ₄ | 1 bar |
| O ₂ , desiccated | Desert | None | 95% O ₂ , 4.5–4.95% N ₂ , 0.5 bar CO ₂ | 10, 100 bar |
| O ₂ , outgassing | Desert | None | 95% O ₂ , 4.5–4.95% N ₂ , 0.5 bar CO ₂ , trace H ₂ O, SO ₂ , OCS, H ₂ S | 10, 100 bar |
| Venus-like, clear sky | Basalt | None | 96.5% CO ₂ , 3.5% N ₂ , trace H ₂ O, SO ₂ , OCS, H ₂ S, NO, HCl | 10, 92 bar |
| Venus-like, cloudy | Basalt | H ₂ SO ₄ | 96.5% CO ₂ , 3.5% N ₂ , trace H ₂ O, SO ₂ , OCS, H ₂ S, NO, HCl | 10, 92 bar |

We initialized these atmospheres with 95% O₂, 0.05 bar CO₂ (consistent with Meadows et al. 2018a), and the remainder N₂, each specified as a fixed surface mixing ratio, with no outgassing. Since this case assumes a planet that was severely depleted in volatiles in both its atmosphere and mantle, these atmospheres are considered completely desiccated (i.e., they contain no water, nor any other hydrogen-bearing species). The remaining composition is dominated by photochemically produced trace gases.

The composition of photochemically produced trace gases, principally O₃ and CO, increases monotonically as a function of irradiation from the parent star (i.e., as a function of semimajor axis). The equilibrium concentration of ozone is due to the competing effects of vertical transport and the Chapman cycle, whereby photolysis of O₂ produces atomic oxygen that can combine with O₂ to form O₃, which is directly lost by photolysis if atomic oxygen combines to form O₂. For the hotter planets (b–d), O₃ photolysis is efficient down to the surface from absorption in the broad Chappuis band. However, the colder planets receive less UV flux as a result of distance from the star, so the photolysis rates are slower. In the coldest atmospheres (f, g and h), eddy transport can overwhelm photolysis and reaction rates for O₃, resulting in well-mixed vertical profiles and saturated O₃ absorption bands. Furthermore, photolysis of O₂ drops faster with semimajor axis because its cross section is limited to the FUV and easily saturates compared to O₃, which includes a strong NUV band and the weak Chappuis band in visible wavelengths, which are not easily saturated.

The monotonic increase in CO with semimajor axis in these atmospheres is due to CO₂ photolysis and lack of recombination. In the terrestrial solar system atmospheres, the

recombination to CO₂ is efficient due to photolytic water products (e.g., OH[−]). Since this environment is devoid of hydrogen, CO can only recombine with atomic oxygen under a slow, density-dependent three-body reaction (Gao et al. 2015).

These modeled environments exhibit surface temperatures (152–406 K, from h to b) that are similar to their equilibrium values (173–400 K; Gillon et al. 2017; Luger et al. 2017b), largely due to low greenhouse gas abundances. The 100 bar cases are cooler at the surface than the 10 bar cases, which indicates an antigreenhouse effect is occurring. The atmospheric structures for these completely desiccated planets each exhibit a stratospheric temperature inversion, like Earth, due to the radiative effects of the photochemically produced O₃ and O₂–O₂ collision-induced absorption (CIA), which is significant in these dense O₂ atmospheres. A sensitivity test removing each constituent to determine the radiative effect suggests that O₃ and O₂–O₂ contribute equally to this heating structure, but via different mechanisms: O₂–O₂ directly absorbs M dwarf NIR irradiation, while O₃ traps outgoing thermal radiation.

The pressure level at which the stratosphere peaks is different than on Earth due to the O₂–O₂ CIA. Earth's stratosphere is caused by O₃ NUV absorption and peaks around ∼0.001 bar, while the pressure level at which the peak in these O₂ atmospheres occurs is much closer to the surface, around 1–10 bar, due to the density dependence of CIA. This stratospheric absorption induces heating in the atmosphere, exceeding heating at the planetary surface, causing a surface temperature inversion similar to Earth and Mars at night (e.g., André & Mahrt 1982; Hinson & Wilson 2004) and inhibiting a troposphere from forming. The causes for these conditions on Earth and Mars at night are due instead to rapid cooling of the surface, rather than warming of the atmosphere.

| | b | c | d | e | f | g | h |
|-------------------------------------|-----|-----|-----|-----|-----|-----|-----|
| Aqua planet, clear | | | | 279 | | | |
| Aqua planet, cloudy 1 bar | | | | 282 | | | |
| O ₂ , desiccated 10 bar | 406 | 343 | 284 | 244 | 208 | 183 | 152 |
| O ₂ , desiccated 100 bar | 386 | 329 | 273 | 237 | 201 | 180 | 153 |
| O ₂ , outgassing 10 bar | 560 | 438 | 343 | 271 | 225 | 200 | 166 |
| O ₂ , outgassing 100 bar | 556 | 476 | 407 | 314 | 261 | 201 | 163 |
| Venus, cloudy 10 bar | | 616 | 398 | 304 | 263 | 243 | 200 |
| Venus, clear 10 bar | 714 | 633 | 593 | 496 | 407 | 336 | 259 |
| Venus, cloudy 92 bar | | 779 | 634 | 551 | 527 | 491 | 398 |
| Venus, clear 92 bar | 927 | 816 | 743 | 689 | 642 | 572 | 465 |

Figure 4. Surface temperatures [K] for every modeled planet and environment combination. Colors represent surface climate: blues are significantly below the freezing point of water, reds are above the runaway greenhouse temperature, and greens are within potentially habitable surface temperatures. The aqua planet environment was only modeled for TRAPPIST-1 e. Venus trace gases have lower boundary values of 30 ppm H₂O, 28 ppm SO₂, 1 ppm OCS, and photochemical abundances of CO and H₂S. Temperate surfaces do not imply habitability due to the inhospitable character of the environmental states, including very low water abundance. Planets in the habitable zone may not necessarily have habitable temperatures.

3.2.2. O₂-dominated Atmospheres: Outgassing

Here we consider the case where a planet has lost its oceans but continues to outgas from a volatile-rich mantle, as is likely the case on Venus (e.g., Bullock & Grinspoon 2001). For other planetary systems, including TRAPPIST-1, this could also be due to delivery by impactors (Chyba 1990; Kral et al. 2018). For all seven planets, we specify Earth-like outgassing fluxes (F), which are relatively well known: $1.68 \times 10^{11} \text{ cm}^2 \text{ s}^{-1}$ H₂O (Burton et al. 2000, $\sim 10F_{\text{CO}_2}$), $1.0 \times 10^8 \text{ cm}^2 \text{ s}^{-1}$ H₂S, $1.35 \times 10^9 \text{ cm}^2 \text{ s}^{-1}$ SO₂ (Carn et al. 2017), $6.88 \times 10^9 \text{ cm}^2 \text{ s}^{-1}$ CO₂ (Williams et al. 1992, $\sim 3.5F_{\text{SO}_2}$), and $3.7 \times 10^5 \text{ cm}^2 \text{ s}^{-1}$ OCS (Belviso et al. 1986, $\sim 10^{-4}F_{\text{CO}_2}$). These fluxes represent volcanic outgassing, so they are distributed within one scale height of the surface ($\sim 6\text{--}20 \text{ km}$). We specify minimal nonzero dry deposition rates of $10^{-8} \text{ cm s}^{-1}$ for all outgassed species to prevent a “runaway” state.

As shown in Figure 5, identical outgassing fluxes result in different levels of trace gases across the seven planets. Some species vary monotonically with irradiation (H₂O, O₃, CO₂), while others do not (CO, SO₂). These trends are modulated by surface gravity (planets b, d, and h have low surface gravity) and atmospheric temperature. There are several interacting chemical networks: carbon, ozone, and sulfur. First consider the carbon network: the primary carbon species are CO₂ and its photolytic product, CO. The CO profiles demonstrate the competing effects of photolysis and vertical transport. The hotter planets have a steep CO gradient, driven by strong photolysis, while the colder planets have well-mixed CO profiles, where vertical transport overcomes photolysis rates and the peak abundance drops. The CO₂ levels are not wholly a function of photolysis; for a given surface pressure, they have different atmospheric column masses (as discussed in Section 3.1 on atmospheric escape). Even though the hotter planets have larger *mixing ratios* of CO₂, because of hotter temperatures their atmospheres are less dense and have smaller *number densities*. Photolysis of CO₂ from identical outgassing fluxes results in lower CO₂ inventories (i.e., number densities) in the more irradiated atmospheres. These CO₂ results differ from the fully desiccated environments because of the Earth-like active surface fluxes we assumed here.

The ozone profiles are very similar to the desiccated O₂-dominated planets. The production of O₃ is the same, but the outgassing planets have more sinks, primarily water vapor. As a result, the outgassing cases overall have lower column densities of O₃. Since the outer planets can be very cold, they cannot maintain much water vapor (Figure 5), so they too can accumulate substantial quantities of O₃, particularly g and h.

The abundance and vertical distribution of species in the sulfur network (SO₂, SO₃, and H₂SO₄) are a balance between water vapor availability, temperature, and photolysis rates. The colder atmospheres are water-limited due to condensation and lower photolysis rates, so atmospheric SO₂ inventories are highest. The formation of SO₃ is from the combination of SO₂ with free oxygen atoms. Sulfuric acid is a primary sink for SO₃ and is formed by (Krasnopolsky 2012)



and can either thermally decompose or condense and rain out. The inner planets receive sufficient irradiation to permit efficient conversion of SO₂ to SO₃ and H₂SO₄.

Volatiles in these atmospheres have a large effect on planetary climate and bridge the results of the O₂-desiccated and Venus-like atmospheres. The coldest planets (g and h) maintain temperature profiles similar to the desiccated cases, including near-surface temperature inversions, because they are too cold to maintain quantities of water vapor sufficient to heat the lower atmospheres. Conversely, the remaining planets generate sufficient water abundances to maintain a positive lapse rate. To prevent a full runaway greenhouse, we have limited the stratospheric water relative humidity to 0.1% for b and 1.0% for c, while the remaining planets are limited to 10%. Planets b, c, and d show the tendency to continue into a runaway greenhouse state, which is supported in our results by their abundances of water vapor well mixed throughout the atmospheric column. Reducing the outgassing of H₂O in our model would more closely approximate the Venus-like H₂O abundance. Only TRAPPIST-1 e has a moderate surface temperature (271–314 K) in this outgassing case, which supports the possibility for it to outgas an ocean and recover habitability.

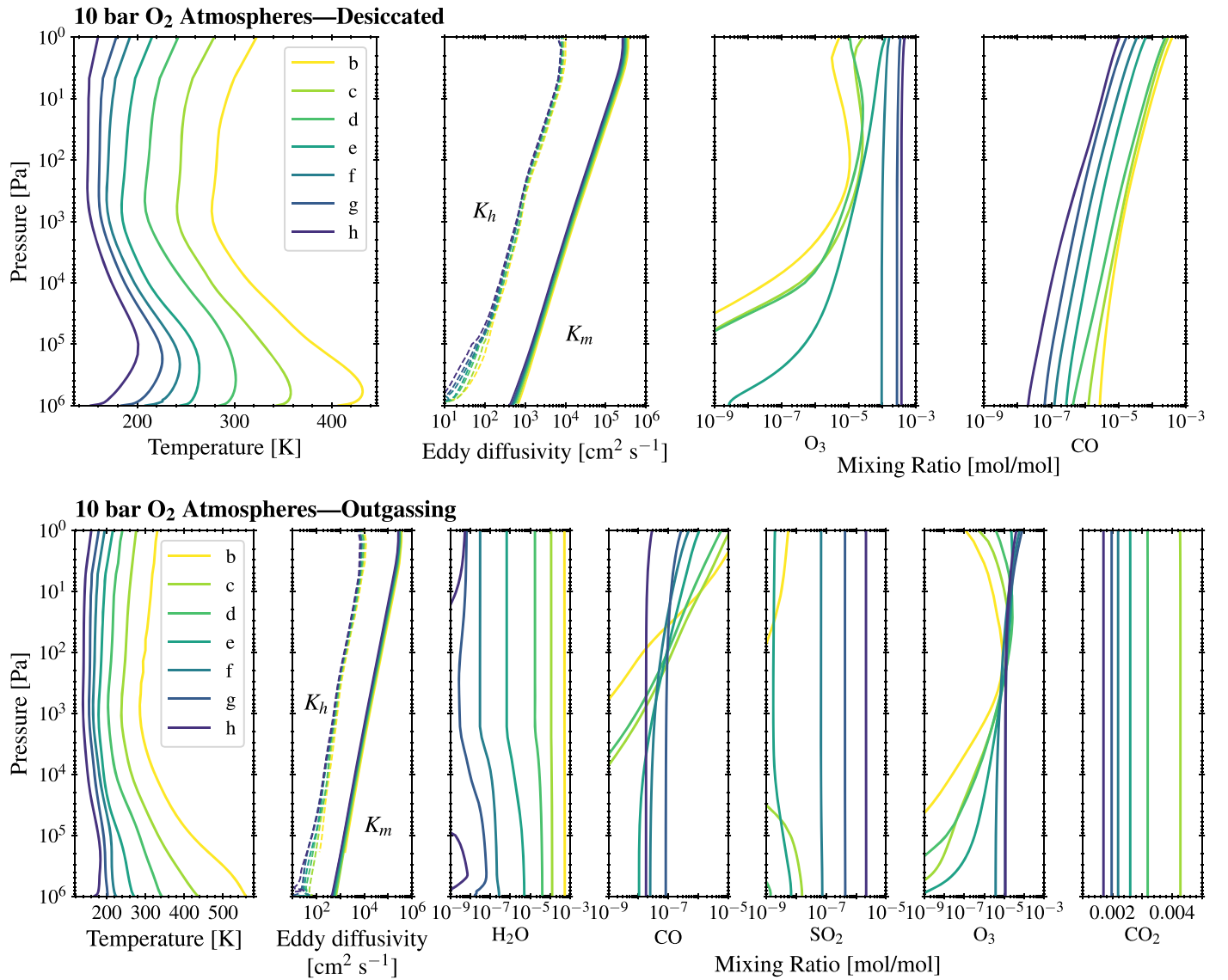


Figure 5. Converged structures for the 10 bar desiccated (upper panel) and outgassing (lower panel) O₂-dominated TRAPPIST-1 atmospheres. The 10 bar atmospheres are similar in structure to the 100 bar atmospheres above 10 bar (10⁶ Pa). The desiccated atmospheric structures exhibit a strong temperature inversion in the lower atmosphere due to absorption by O₃ and O₂-O₂. The outgassing atmospheric structures and associated surface temperatures exhibit a continuum from Venus-like hotter atmospheres to colder temperature profiles similar to the desiccated cases.

3.2.3. Venus-like Atmospheres

Here we model Venus-like environments, which may be common around M dwarfs (Kane et al. 2014). For this environmental state, we assume that the complete loss of oceans during the superluminous pre-main-sequence phase removed a potentially strong sink for soluble gases (e.g., CO₂ and SO₂). Subsequent loss or sequestration of oxygen over time (Schaefer et al. 2016), and initial and subsequent outgassing of volatiles, may have allowed a Venus-like high-CO₂ atmosphere to develop. Even though planet h may not have lost an entire Earth ocean (see Figure 3), it could have initially outgassed significant amounts of CO₂. We modeled Venus-like atmospheres for all seven planets (Figure 6) using the 10 bar boundary conditions used to validate observations of Venus, following Krasnopolsky (2012; see Appendix C). Venus atmospheric chemistry is typically modeled in sections: by thermochemistry, which dominates the lower atmosphere below the cloud deck (e.g., Krasnopolsky 2013), and by

photochemistry, which is responsible for the directly observable altitudes at and above the cloud deck (e.g., Krasnopolsky 2012; Zhang et al. 2012). We use photochemistry to model these atmospheres but do not include thermochemical reactions, which could be a useful improvement in future work for the planets with the highest surface temperatures.

Our Venus atmospheres are initiated as either 10 or 92 bar of total pressure with Venus-like levels of CO₂ (96.5%) and N₂ (3.5%). For the 92 bar cases, we assumed a constant mixing ratio for every species from 10 bar to the surface. We initiated the photochemical model with the trace-gas lower boundary conditions required to reproduce observations of Venus following the modeling of Krasnopolsky (2012), consisting of fixed mixing ratios at 10 bar of 30 ppm H₂O, 4.5 ppm H₂, 5.5 ppm NO, 28 ppm SO₂, 1 ppm OCS, and 400 ppm HCl. We calculate the photochemical–kinetic equilibrium profiles of these and other trace gases subject to these boundary conditions. These trace gases absorb at wavelengths that are

Table 3
Ozone Column Densities [cm⁻²]

| Planets | b | c | d | e | f | g | h |
|--------------------------------------|----------------------|----------------------|----------------------|----------------------|----------------------|----------------------|----------------------|
| Aqua planet, clear, 1 bar | | | | 3.1×10^{18} | | | |
| Aqua planet, cloudy, 1 bar | | | | 2.9×10^{18} | | | |
| O ₂ , desiccated, 10 bar | 2.5×10^{18} | 6.3×10^{18} | 1.1×10^{19} | 4.7×10^{19} | 2.2×10^{22} | 6.0×10^{22} | 1.3×10^{23} |
| O ₂ , desiccated, 100 bar | 7.2×10^{17} | 2.4×10^{18} | 6.4×10^{18} | 8.8×10^{18} | 6.1×10^{22} | 2.7×10^{23} | 1.4×10^{24} |
| O ₂ , outgassing, 10 bar | 1.6×10^{18} | 5.2×10^{18} | 9.9×10^{18} | 2.7×10^{19} | 8.5×10^{20} | 2.4×10^{21} | 4.0×10^{21} |
| O ₂ , outgassing, 100 bar | 1.7×10^{19} | 2.1×10^{20} | 2.7×10^{21} | 2.4×10^{22} | 7.2×10^{23} | 6.6×10^{24} | 1.8×10^{25} |
| Venus-like, clear, 10 bar | 2.3×10^{15} | 2.1×10^{15} | 5.4×10^{15} | 1.0×10^{15} | 6.9×10^{15} | 8.6×10^{15} | 1.5×10^{16} |
| Venus-like, cloudy, 10 bar | | 1.0×10^{15} | 1.1×10^{16} | 4.6×10^{15} | 7.6×10^{15} | 9.1×10^{15} | 1.5×10^{16} |
| Venus-like, clear, 92 bar | 1.8×10^{15} | 1.9×10^{15} | 5.1×10^{15} | 1.3×10^{15} | 6.7×10^{15} | 9.1×10^{15} | 1.6×10^{16} |
| Venus-like, cloudy, 92 bar | | 1.0×10^{15} | 9.5×10^{14} | 4.2×10^{15} | 7.8×10^{15} | 9.8×10^{15} | 1.6×10^{16} |

Note. Compare to global-average Earth ozone column depth of 8×10^{18} cm⁻² (<https://ozonewatch.gsfc.nasa.gov/>).

complementary to CO₂ and can have a substantial effect on climate (Bullock & Grinspoon 2013; Lee et al. 2016).

For purposes of climate-photochemical modeling for observational discriminants, we separately model both clear-sky and cloudy Venus-like atmospheres, except for planet b, which does not condense sulfuric acid aerosols in our photochemistry model. Both clear-sky and cloudy atmospheres display a similar, Venus-like profile (dashed black line in Figure 6), despite being irradiated by a very different SED than the Sun. The temperature profiles are characterized by long adiabats from the surface each to a ~ 0.05 –1.0 bar tropopause. The surface temperatures are the hottest of the environments we simulated, ranging from 259–465 K (200–398 K cloudy) for planet h (outside the outer edge of the HZ) to 714–927 K for b, which receives approximately twice the stellar flux of Venus.

As in the O₂-outgassing cases, the Venus-like atmospheric photochemistry is dominated by the formation of sulfuric acid from the combination of water with SO₃, a photolytically derived product of SO₂. This sulfur chemistry is not driven as strongly as that of Venus due to lower MUV–NUV flux from TRAPPIST-1, so the rates of both SO₂ and SO₃ photolysis are much lower than for Venus. However, SO₂ is still susceptible to photolytic destruction, which results in the trend seen in Figure 6, that SO₂ is more abundant farther from the star. The abundance of SO₃ is a balance between its formation rate via SO₂ photolysis and the rate at which it combines with water to form H₂SO₄. In our simulations, water vapor decreases as a function of semimajor axis in both clear-sky and cloudy cases due to this condensation into H₂SO₄ aerosols, as well as into water and water-ice in the cooler planets (e, f, g, and h, although we do not model the water clouds that would form as a result of this process).

The prevalence of H₂SO₄ vapor depends on its chemical formation, where and whether it condenses, and its destruction via thermal decomposition in the lower atmosphere. In our simulations, H₂SO₄ formed in abundances similar to that on Venus (up to 17 ppm versus 8.5 ppm for Venus; Krasnopolsky 2015) for the hotter TRAPPIST-1 planets and drops in abundance with semimajor axis due to the reduced availability of H₂O at lower temperatures. The highest abundances of H₂SO₄ and SO₃ are seen in the stratospheres of the hotter planets (b and c), with peak vapor concentrations decreasing with semimajor axis and at lower altitudes. Similarly, the peak optical depths of the clouds drop with semimajor axis due to less effective formation processes. Since H₂SO₄ can persist closer to the surface in the colder atmospheres, the

semimajor-axis-dependent total optical depth peaks for planet d, due to the competing effects of formation/condensation and thermal decomposition/rainout (see Figure 7). Notably, for planet b, the modeled atmosphere was too hot for condensation. Planet d exhibited the highest aerosol optical depth due to its low surface gravity, which allows aerosols to be more easily lofted in the atmosphere.

The sulfuric acid aerosols in our cloudy Venus atmospheres substantially reduced the surface temperatures. The net top of atmosphere stellar irradiance was reduced by $\sim 50\%$ –60%, resulting in temperature ranges of 200–616 K (10 bar) and 398–779 K (92 bar), h to c. As a caveat, it is possible that sulfuric acid production in Venus’s atmosphere may vary by orders of magnitude (Gao et al. 2014), and it is unknown how an alien M dwarf spectrum may affect the more uncertain aspects of Venus-like atmospheric chemistry, particularly of the unknown UV absorber, which we exclude.

3.2.4. Aqua Planet

For TRAPPIST-1 e only, we modeled a potentially habitable, ocean-covered planet. Our initial work and that of recent 3D GCM studies (Wolf 2017; Turbet et al. 2018) suggest that the other habitable zone planets (f and g) require CO₂-dominated atmospheres for stability and cannot be Earth-like. This temperate, Earth-like atmosphere could exist if e had a sufficient volatile inventory to survive the stellar pre-main-sequence or had subsequent outgassing or water delivery, or if these planets migrated after formation (Luger et al. 2015; Meadows et al. 2018a). We simulated this environment with an atmosphere of 80% N₂ and 20% O₂, similar to Earth. We assume the O₂ could be either biogenic or have resulted from early ocean loss. In addition to the fluxes assumed for the outgassing O₂ cases, we specify an Earth-like geological source of CH₄ (6.8×10^8 cm² s⁻¹; Guzmán-Marmolejo et al. 2013). Water vapor is calculated self-consistently using our mixing-length convection and condensation routine, described in Appendix A.3, assuming 100% surface relative humidity.

We model both cloudy and clear-sky atmospheres for the aqua planet, shown in Figure 8 with Earth for comparison. In the cloudy case, we specify cirrus and altostratus clouds, each of cumulative optical depth $\tau = 5$. These are based on the VPL 3D Spectral Earth Model, which used Earth observing data with our SMART radiative transfer model to faithfully reproduce Earth’s spectrum (Robinson et al. 2011).

We use a wavelength-dependent open-ocean surface albedo for this planet. We found that typical snow-covered ice surfaces

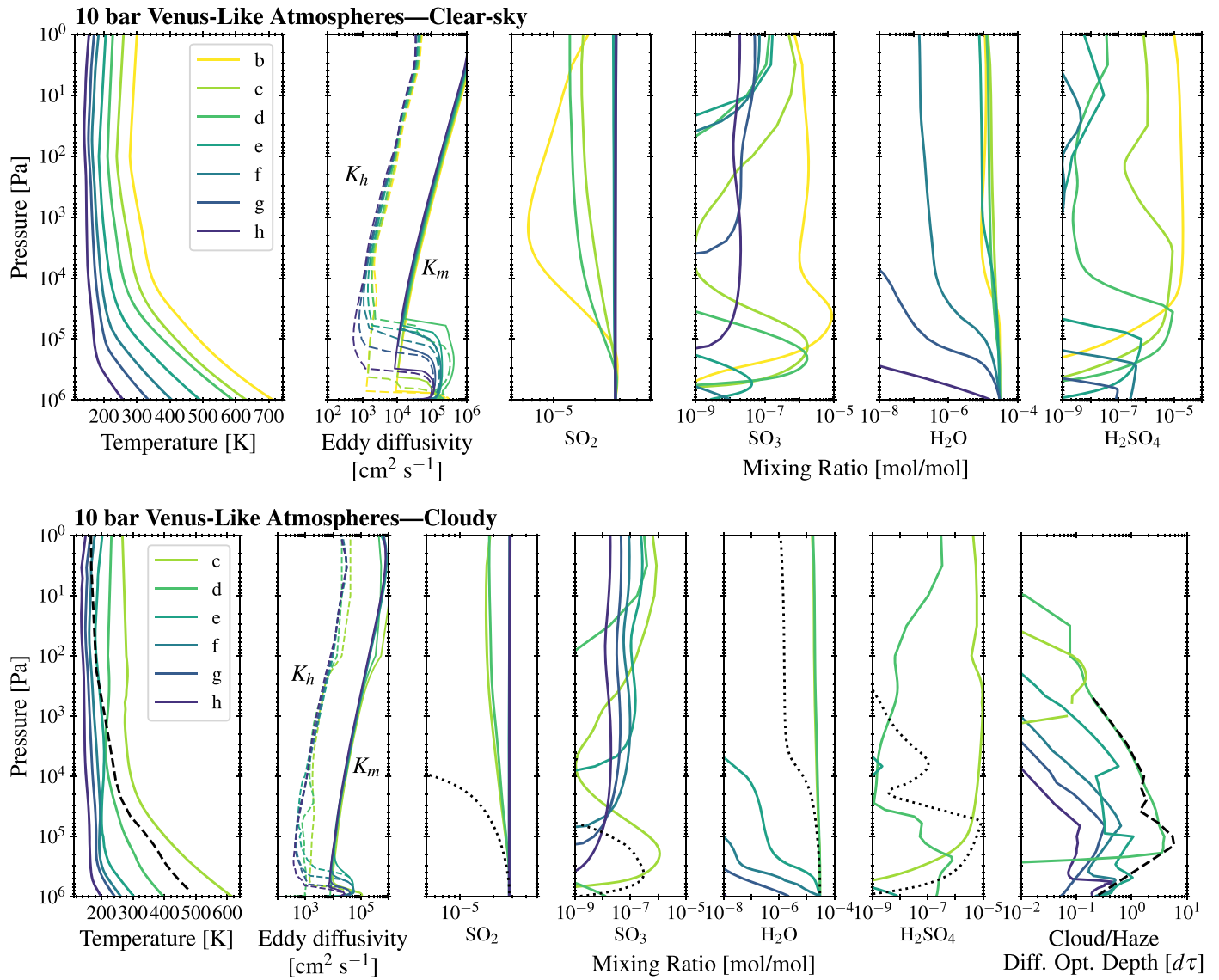


Figure 6. Converged structures of the 10 bar clear-sky (upper panel) and cloudy (lower panel) Venus-like TRAPPIST-1 atmospheres. Note: b is not included in the cloudy case, as aerosols were not formed. The Venus International Reference Atmosphere (VIRA) temperature structure is shown in the cloudy panel (black dashed line). The 92 bar atmospheres are not shown here but show a structure similar to the 10 bar cases. Here we show H_2O , SO_2 , SO_3 , and H_2SO_4 gases only, being the most relevant to climate and cloud formation. The bulk gases CO_2 and N_2 are 96.5% CO_2 and 3.5% N_2 . With a (clear-sky) Venus-like atmosphere, TRAPPIST-1 b may exhibit surface temperatures in excess of Venus (due to higher insolation) and is too hot to form sulfuric acid aerosols in our model, even though it was most effective at forming high-altitude H_2SO_4 vapor. Sulfur dioxide survives more readily in these atmospheres, due to the lower MUV–NUV flux compared to the Sun.

with albedo up to 0.73 in the visible had little impact on surface temperature, since the SEDs of TRAPPIST-1 and other late-type M dwarfs emit most of their radiation longward of $1 \mu\text{m}$, and both ice and water are efficient absorbers in the NIR (Shields et al. 2013).

These aqua planet cases are able to maintain temperate surfaces (279 K clear, 282 K cloudy). The clouds have a slight greenhouse effect, as the energy lost by scattering incoming stellar light is more than balanced by a colder emission temperature. The cloudy environment exhibits a much cooler tropopause and weak stratosphere but similar tropospheric profile, since the troposphere is driven by moist convective processes in both cases.

With Earth-like outgassing, the aqua planets exhibit preindustrial Earth-like abundances of CO_2 , but different profiles of other trace gases. The stratospheric water abundance is reduced by a cold tropopause, more so for the cloudy case. The ozone profile is different than Earth’s, with a broader,

higher altitude (lower pressure) peak abundance, although the column density is only slightly lower (Table 3). Ozone failed to produce a significant stratosphere, because the stellar spectrum provides very little flux at NUV–visible wavelengths absorbed by O_3 . For this modeled environment, we limited CO to photochemical production, so the tropospheric levels are significantly less than Earth’s CO, which is primarily from biologically related sources (Seinfeld & Pandis 2006). Similarly, the geological fluxes result in a correspondingly lower tropospheric methane abundance but similar abundance in the upper stratosphere.

3.3. Spectra and Observational Discriminants

Here we show simulated transit transmission and emission spectra for our evolved worlds to support observation planning with *JWST* for this planetary system. These are noiseless spectra generated using SMART, sampled at 1 cm^{-1} and

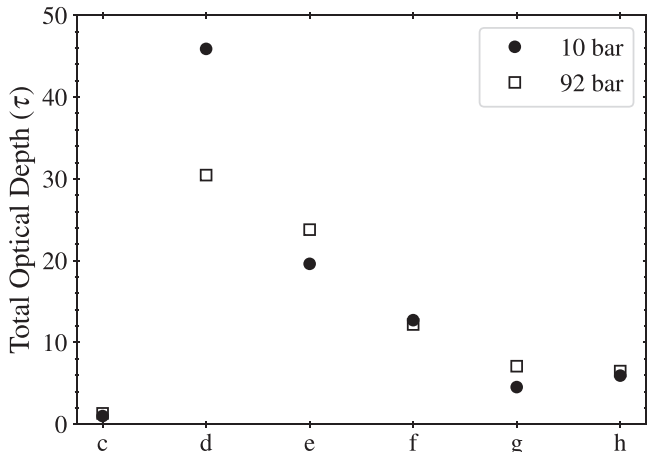


Figure 7. Sulfuric acid cloud total optical depths for each cloudy Venus atmosphere. TRAPPIST-1 b did not condense sulfuric acid in our models. TRAPPIST-1 c maintained only thin clouds, because sulfuric acid absorption warms the cloud layer and the local warming can cause the clouds to evaporate. Optical depths peak for planet d, which has vigorous sulfuric acid formation and has lower surface gravity, so it can more easily loft aerosols. The planets generally decline in optical depth with distance from the star due to lower photolysis rates and, for the 10 bar atmospheres, the lower abundance of water vapor. Note the 92 bar atmosphere photochemistry and cloud formation were truncated at 10 bar. Planets f, g, and h had cloud formation to 10 bar and so could also form thicker clouds deeper toward the surface.

convolved with a 1 cm^{-1} half-width at half-maximum slit function, which can be used as the model input for instrument and observation simulators that calculate noise sources and instrument sensitivity. These spectra can also be compared with known or anticipated instrument noise floors to determine zeroth-order signal detectability. In a subsequent paper (J. Lustig-Yaeger et al., in preparation), these spectra will be used to quantify the detectability of our simulated atmospheres with *JWST* and assess optimum observing techniques for identifying key planetary characteristics.

We have also produced direct-imaging reflectance spectra. Reflectance spectra of late-type M dwarfs may first be observed by large ground-based instruments, or later by HabEx/LUVOIR. The spectra we simulated, including those not presented here, are available online using the VPL Spectral Explorer¹³ or upon request.

3.3.1. Transit Transmission Spectra

In Figures 9–11, we show transit transmission spectra of our modeled TRAPPIST-1 planetary environments, covering nearly the entire wavelength range of potential *JWST* exoplanet observations (0.5–20 μm). These spectra are presented as “relative transit depth,” that is, the signal originating from the atmosphere as compared to the solid planetary body. Note in this paper we do not account for stellar limb darkening, so “transit depth” here refers to $(R_p/R_*)^2$, where R_p is the radius of the solid body and R_* the radius of the star. To assess the signal originating from the atmosphere, we can expand the transit depth,

$$\frac{dF}{F} = \left(\frac{R_p + R_a}{R_*} \right)^2 = \left(\frac{R_p}{R_*} \right)^2 + \frac{2R_p R_a}{R_*^2} + \left(\frac{R_a}{R_*} \right)^2, \quad (3)$$

and define the relative transit depth of the atmosphere, valid for atmospheres with small scale height:

$$\frac{dF_a}{F} \approx \frac{2R_p R_a}{R_*^2}, \quad (4)$$

where R_a is the vertical extent of the atmosphere. Although the radius of the solid body and altitude of the atmosphere for exoplanets cannot be separately measured, this equation allows us to relate predicted variations in transit depth of the modeled spectra for different-sized bodies to the physical extent of the modeled atmospheres.

The seven planets exhibit a variety of features in transmission, the strengths of which depend on each planet’s characteristics. TRAPPIST-1 b displays the strongest features, owing to its higher temperature and moderately low surface gravity, both of which increase the atmospheric scale height and therefore its transmission signal. Planet b shows molecular signals exceeding 200 ppm, which is well above the putative 20, 30, and 50 ppm noise floors for *JWST* NIRISS SOSS, NIRCam grism, and MIRI LRS, respectively (Greene et al. 2016). Planet d exhibits molecular signals nearly as strong as b, in large part because d has the lowest surface gravity of these planets. Due to geometry and the effects of refraction (Misra et al. 2014; Meadows et al. 2018a), the surface and near-surface atmospheres of the 10–100 bar atmospheres cannot be probed with *JWST* transmission spectroscopy. All of the modeled atmospheres we present include CO₂, and despite a broad range of abundances, they all exhibit strong CO₂ absorption at 2.0, 2.8, 4.3, and 15 μm , though the hotter or higher abundance CO₂ atmospheres have additional CO₂ features, particularly shortward of 2 μm . In the following subsections, we present the spectra for each environment.

O₂-Dominated Atmospheres, Desiccated: Transit transmission spectra for the desiccated, high-O₂ atmospheres are presented in Figure 9. As in Schwertner et al. (2016) and Meadows et al. (2018a), the characteristic spectral features of a high-O₂ atmosphere are strong O₃ and O₂–O₂ CIA bands together. The CIA bands are strongest at 1.06 and 1.27 μm . A mixture of O₂, O₃, and O₂–O₂ is present at 0.5–1.3 μm , and a mixture of CO₂, CO, and O₃ at 1.5–6 μm . The strongest O₃ features are the Chappuis band at \sim 0.6 μm and the 9.6 μm feature, with weaker bands at 2.5, 3.3, 3.6, 4.75, and 5.6 μm . These weaker bands are generally only available here because of high levels of O₃ combined with relatively low levels of CO₂. Most of this wavelength range could be accessible to *JWST* NIRISS and NIRSpec instruments. Features of CO₂ and O₃ are also present at 6–20 μm , which could be probed by the *JWST* MRS instrument. In addition to the complete lack of any water features, the presence of CO features (2.35 μm and 4.6 μm) is characteristic of this severely desiccated atmosphere (e.g., Gao et al. 2015), though these will be very challenging to observe with *JWST*.

O₂-Dominated Atmospheres, Outgassing: The transmission spectra of the outgassing atmospheres are shown in Figure 9. The detectability of outgassed trace species varies by planet, particularly for H₂O and SO₂. Water features at 1.4, 1.9, 2.6, 3.0–3.3, and 6.3 μm rival the strength of CO₂ bands for the hottest planets (b, c, and d), due to stratospheric water vapor in excess of the moist greenhouse limit, indicative of planets experiencing water loss. The colder planets have insufficient H₂O to generate H₂SO₄, so they maintain higher levels of SO₂,

¹³ <http://depts.washington.edu/naipl/content/vpl-spectral-explorer>

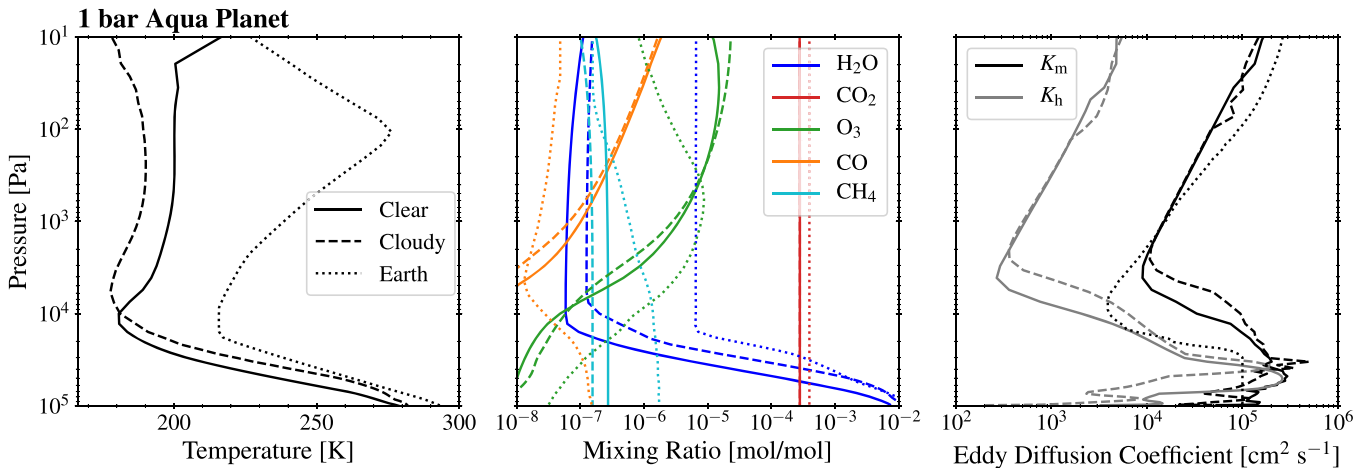


Figure 8. Climates, gas mixing ratios, and eddy diffusion profiles for TRAPPIST-1 e, clear-sky, and cloudy aqua planets. Included are data from Earth: the temperature and mixing ratio profiles are from case 62 of the Intercomparison of Radiation Codes in Climate Models (ICRCCM), and the eddy diffusion rate is that retrieved by Massie & Hunten (1981). The temperatures of our modeled atmospheres are somewhat colder than that of modern Earth, but they are still able to maintain surface water. The mixing ratios of trace constituents differ from modern Earth, except CO₂.

which shows small features of less than 60 ppm at 4.0, 7.3, 8.7, and 19 μm . Much larger SO₂ fluxes or lower water vapor abundances would be required to generate SO₂ features above the putative noise floor of *JWST* (20–50 ppm; Greene et al. 2016).

Venus-like Atmospheres: Clear-sky and cloudy Venus-like transmission spectra are shown in Figure 10. With a clear sky, Venus-like atmospheres exhibit deep absorption features, primarily from CO₂. Water vapor is present in the clear-sky spectra at 0.9–2.0 μm and at 6.3 μm . Sulfuric acid aerosols truncate the minimum altitude probed by the transmission measurement, severely reducing the strength of the absorption features. These Venus-like planets may have absorption features in transmission approaching ~90 ppm.

Aqua Planet: Clear-sky and cloudy aqua planet transmission spectra for TRAPPIST-1 e are shown in Figure 11. Due to the large angular size of TRAPPIST-1 as seen from the planet, the clear-sky atmosphere can be probed nearly to the surface, while the cloud deck truncates the spectrum at 11 km. A number of molecular absorption bands are present, including O₃ (~0.6, 4.7, 9.6 μm), O₂ (0.76, 1.27 μm), CH₄ weakly (3.3 and 7.7 μm), and H₂O (6.3 μm). Even with an abundance of only ~290 ppm, CO₂ is the most observable molecule in these atmospheres (1.6, 2.0, 2.7, 4.3, 15 μm). The bulk atmospheric constituent, nitrogen, exhibits a 4.1 μm CIA band, which could provide a sensitive probe of its partial pressure (Schwieterman et al. 2015).

3.3.2. Emission Spectra

We present thermal emission spectra as normalized flux (Figures 12 and 13). Below ~5 μm , stellar flux reflected from the surface or scattered in the atmosphere contributes significantly to the spectra.

O₂-Dominanted Atmospheres, Desiccated: The desiccated, O₂-dominated atmospheres (Figure 12) are distinctive in emission spectra, due to lower temperatures, lack of water bands, and their unusual temperature structures. The stratospheric temperature peak causes some bands to be seen in emission rather than absorption, depending on how cool the particular planet is. In the colder atmospheres, the O₃ band at 9.6 μm exhibits varying hot wing emission at 10.4 μm from

the stratospheric temperature peak. In the hotter atmospheres with lower O₃ abundance, part of the 9.4 μm CO₂ “hot band” also emerges in emission at 9.0 μm . CO₂ varies between absorption and emission at ~10–18 μm . As a potential insight into isotope fractionation for ¹⁸O/¹⁶O, the fundamental asymmetric stretch $v_1 = 1 \rightarrow 0$ transition of the ¹⁶O¹²C¹⁸O isotopologue at 7.3 and 7.9 μm (Rothman et al. 2013) appears in emission. The O₂ band at 6.4 μm exhibits strong emission, but it is very narrow and is present only because of the complete lack of water vapor. Carbon monoxide is not observable.

O₂-Dominated Atmospheres, Outgassing: The emission spectra of the O₂-dominated, outgassing atmospheres are given in Figure 12. The radiative–convective processes and resultant emission spectra are largely dominated by water vapor in the atmosphere. The warmer planets, with larger quantities of water vapor throughout the atmospheric column, exhibit massive H₂O absorption in the 6.3 μm band. Conversely, the colder, drier planets exhibit SO₂ absorption at 7.3, 8.8, and 19 μm . These outgassing atmospheres have much less ozone than the desiccated ones, due to destruction catalyzed by the presence of water vapor, so their O₃ features are much weaker, particularly for the warmer planets.

Venus-like Atmospheres: The Venus-like atmospheres (Figure 12) emit very little flux, except through narrow windows between strong absorption bands, similar to Venus. This suppression of emitted flux is due to the combined Venus greenhouse of primarily CO₂, H₂O, and SO₂. The emission windows in the hotter atmospheres are at 2.4, 3.5, and 5.5–7.0 μm . The cooler, clear-sky planets emit some flux around 10 μm , between CO₂ hot bands. In the clear-sky case, water vapor absorbs weakly in the 5.5–7.0 μm window, and SO₂ absorbs at 7–9 μm , but these are obscured in the cloudy case. The remaining emission is reduced by CO₂ absorption. The cloudy spectra exhibit more shallow absorption features and are more similar to a blackbody spectrum because the thermal emission is primarily from the cloud deck, though the colder planets also emit above the cloud deck from the 15 μm CO₂ band.

Aqua Planets: The potentially habitable aqua planet atmospheres (Figure 13) have emission spectra very similar to that of Earth (see Robinson et al. 2011). The near-surface

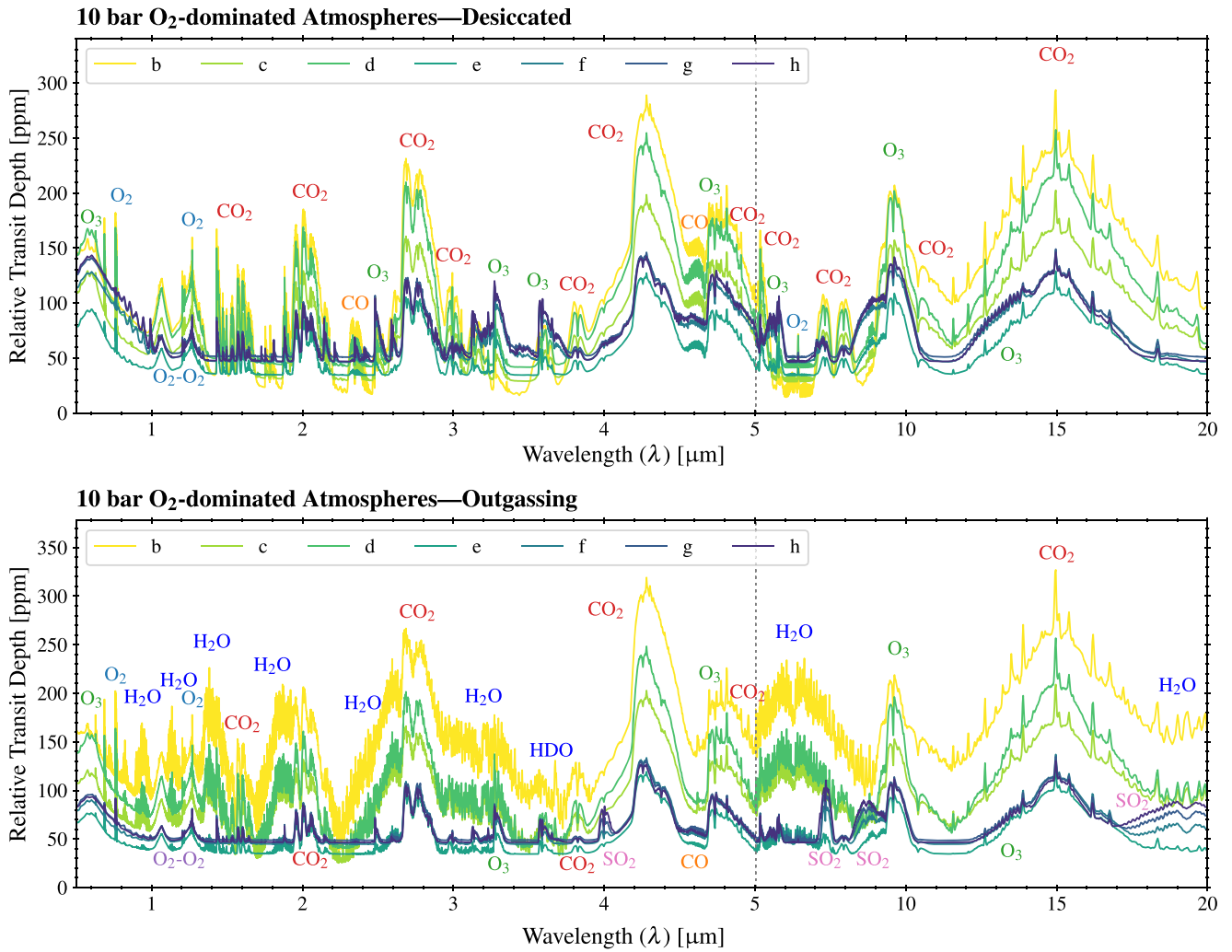


Figure 9. Simulated transit transmission spectra for the O₂ desiccated (upper panel) and O₂ outgassing (lower panel) atmospheres. The y axes are the relative transit depths and show the modeled atmospheric signal. We show only the 10 bar atmospheres, as the 100 bar atmospheres are qualitatively similar. The desiccated atmospheres are dominated by CO₂ and O₂-O₂. The presence of weaker O₃ bands and CO are indicative of the desiccated environment. The outgassing atmospheres have additional features from H₂O and SO₂. The hotter atmospheres maintain substantial stratospheric H₂O, and the outer planets, too cold to maintain H₂O, build up SO₂, which would otherwise condense with H₂O to form sulfuric acid.

absorption from the water vapor continuum is apparent in the clear-sky case, particularly at 10–13 μm , and the cloudy case emits from its global cloud deck at a colder temperature. Both cases exhibit absorption from H₂O (6.3 μm), O₃ (9.6 μm), and CO₂ (15 μm).

4. Discussion

We have used a new, versatile coupled climate-photochemical model to generate environmental states for the TRAPPIST-1 planets for different assumed evolved atmospheres, including desiccated and water-rich. These atmospheric states are climatically and photochemically self-consistent with the spectral energy distribution from the parent star and show a diversity of characteristics as a function of bulk composition, orbital distance, and outgassing rates. These characteristics are very different from those expected for H₂-dominated atmospheres. We have shown that the non-Earth-like atmospheric compositions that may result from M dwarf stellar evolution strongly impact planetary climate and surface temperature, potentially reducing habitability within the HZ. Hot temperatures modeled beyond the outer edge require additional study to determine if the habitable zone could be

extended with additional trace gases. These different environments produce spectral features that can be observed by upcoming observatories, including *JWST*, to discriminate among the environments. Here we discuss important implications of this work for M dwarf terrestrial planets in the areas of atmospheric evolution and escape, climate and photochemistry, observational discriminants, and prospects for future observations of these environments.

4.1. Atmospheric Escape, Ocean Loss, and Oxygen Accumulation

We conducted a study of H₂O loss and O₂ accumulation for the TRAPPIST-1 system using an update to the model of Luger & Barnes (2015), and we found that ocean loss affects the entire HZ. Even planets that are beyond the outer edge during the main sequence phase (e.g., TRAPPIST-1 h) have the potential to lose a significant ocean fraction and generate O₂. These results are broadly consistent with a study on ultracool dwarf stars conducted by Bolmont et al. (2017). Note that Bolmont et al. based their TRAPPIST-1 work on earlier system parameters (Gillon et al. 2016), which included only planets b,

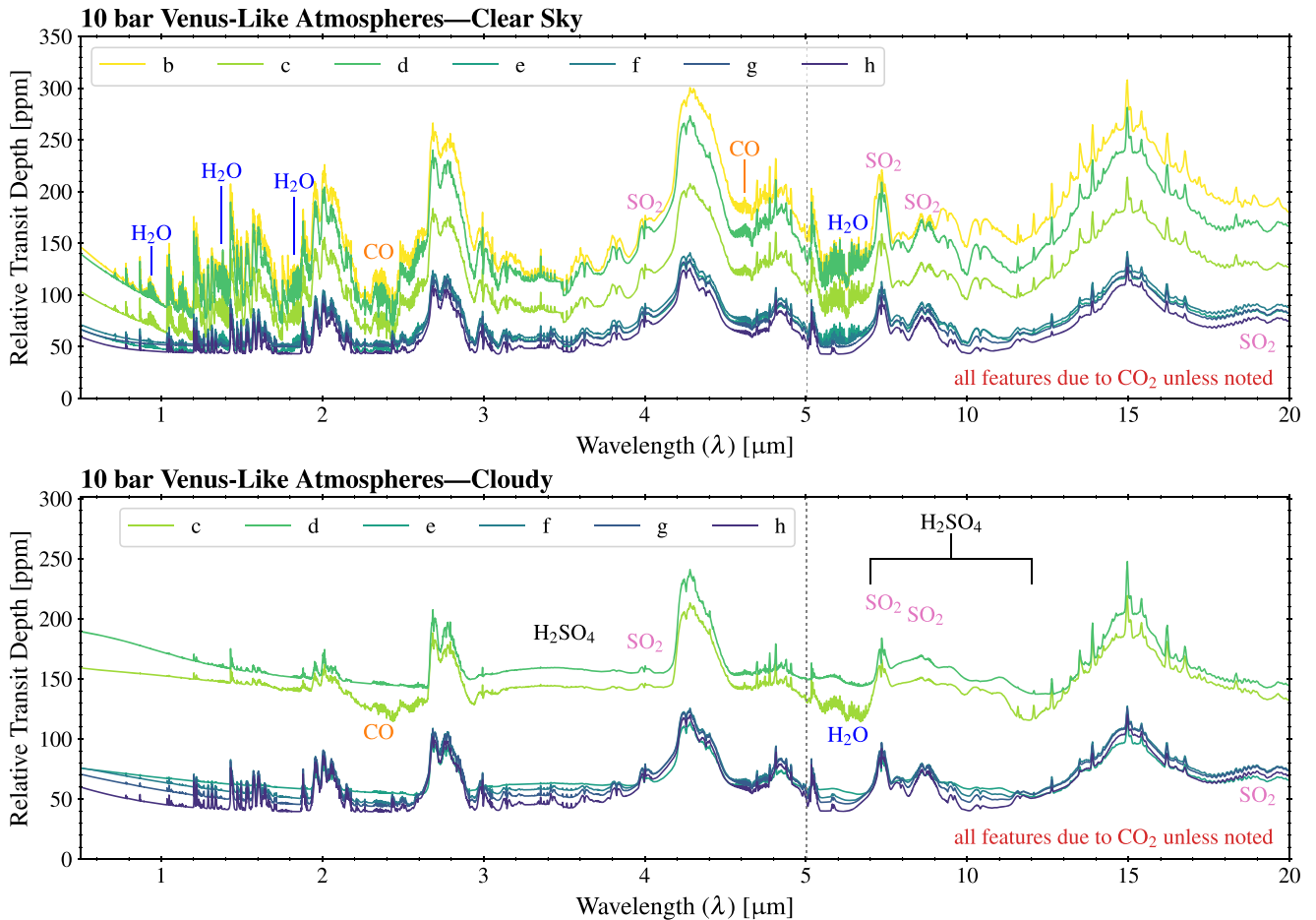


Figure 10. Simulated transit transmission spectra for the Venus-like clear-sky (upper panel) and cloudy (lower panel) atmospheres. The y axes are the relative transit depths and show the modeled atmospheric signal. We show only 10 bar atmospheres, as the 92 bar atmospheres are quantitatively similar. All unlabeled features are CO_2 , which dominate these spectra. The generally flat, higher transit depths of the cloudy Venus-like spectra are due to the sulfuric acid aerosols. TRAPPIST-1 b is not included because it did not condense H_2SO_4 in our model. The colder cloudy atmospheres have lower cloud decks (see Figure 6), revealing deeper relative transit depths.

c, and a range of semimajor axes for d. Where we can compare, we predict up to an order of magnitude larger amounts of H loss and O_2 accumulation, likely due to our much older stellar age (5 Gyr, Burgasser & Mamajek 2017, versus 850 Myr, Bolmont et al. 2017) and assumptions for the planetary radii and masses, which we based on additional observations (Grimm et al. 2018).

Our model and calculation of the escape efficiency ϵ_{xuv} are consistent with the value inferred for low-mass planets in the *Kepler* population, considering their sizes and densities as a function of irradiation (Owen & Wu 2013). Another metric, the “cosmic shoreline,” supports our use of thermally driven hydrodynamic escape. The “cosmic shoreline” is an empirically derived relationship between planetary irradiation and escape velocity that divides planets with atmospheres from airless rocks and appears to apply broadly to the solar system and the population of exoplanets with known densities (Zahnle & Catling 2017).

A thorough discussion of caveats for assessing H escape and O_2 accumulation was given by Bolmont et al. (2017). We do not include the effects of O_2 loss processes other than thermal escape, such as surface sinks (Schaefer et al. 2016; Wordsworth et al. 2018) and nonthermal atmospheric loss (Collinson et al. 2016; Airapetian et al. 2017), which are important and warrant further

detailed study. At the location of Proxima Centauri b for an Earth twin, the calculated nonthermal escape rate may not currently exceed Earth-like outgassing replenishment rates, which may allow a secondary atmosphere to accumulate (Garcia-Sage et al. 2017). However, nonthermal escape could have contributed to net O_2 loss during the pre-main-sequence phase. Therefore, the O_2 generated by our evolution models represents maximum possible inventories, using nominal parameters for stellar and planetary properties. We reduced the O_2 abundance for our climate-photochemistry and spectral models in consideration of these loss mechanisms, which we did not include in our models. Given the importance of oxygen as a biosignature, the generation of abiotic, O_2 -rich post-ocean-loss atmospheres should be considered when interpreting future observations of M dwarf terrestrial planets.

4.2. Climate and Photochemistry in the TRAPPIST-1 Planetary System

These diverse environments produce a wide range of habitable and uninhabitable surface temperatures (Figure 4), suggesting that the region around a star where Venus-like planets may be common evolutionary outcomes (Kane et al. 2014) may extend into and beyond the classical habitable zone for late-type M dwarfs. Even though some of these modeled

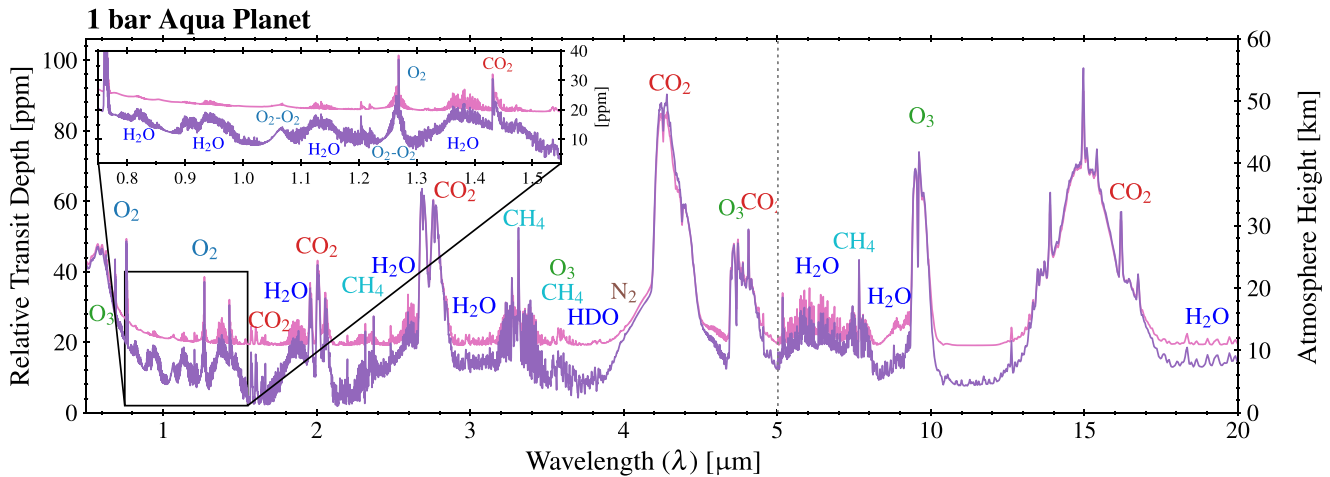


Figure 11. Transit transmission spectrum for clear-sky and cloudy TRAPPIST-1 e aqua planets. Most of this simulated planet’s important and abundant gases, including H_2O , O_2 , CH_4 , and O_3 , have features in this spectral range. These cloudy and clear spectra demonstrate that a potentially habitable planetary atmosphere, some of its trace outgassed constituents, and the photochemical by-products are accessible using transmission spectroscopy, which could be attempted with *JWST*.

environments do not support surface liquid water, if dense CO_2 atmospheres do form on terrestrial planets after an early runaway greenhouse phase, our results suggest that surface temperatures in the habitable range or hotter may occur beyond the classical maximum greenhouse limit of the HZ outer edge (where warming from additional CO_2 is offset by higher Rayleigh scattering in a temperate $\text{H}_2\text{O}-\text{CO}_2$ greenhouse; Kasting et al. 1993). Even TRAPPIST-1 h, beyond the HZ outer edge ($S_h = 0.148S_\oplus$), could have a surface temperature as hot as 465 K if early atmospheric evolution resulted in a clear-sky Venus-like atmosphere, and 398 K with the expected sulfuric acid clouds. These high temperatures may be stable over long time periods, because known sinks for CO_2 —such as deposition to an ocean and carbonate–silicate weathering (Walker et al. 1981)—will not be available, although a surface carbonate buffer may form and keep the atmosphere at an equilibrium CO_2 value that is less than 92 bar (Hashimoto et al. 1997). Figure 4 also shows that across the diversity of atmospheres considered, the instillation at the modeled TRAPPIST-1 e’s distance from the star was most likely to maintain a habitable surface temperature. This suggests that the habitable zone concept is still useful as an initial means of narrowing down the search for habitable conditions on terrestrial planets, even when planetary atmospheres are not truly Earth-like.

For late-type M dwarf stars in particular, our work indicates that the maximum greenhouse limit may not apply, or may apply at a distance much farther from the star than previously calculated (Kopparapu et al. 2013). We have shown that the $\text{H}_2\text{O}-\text{CO}_2$ greenhouse used in traditional habitability calculations can be enhanced significantly by other greenhouse gases, including SO_2 . While SO_2 is a greenhouse gas in desiccated atmospheres like that of Venus (e.g., Lee et al. 2016), it is less likely to be present in the atmosphere of a habitable planet with an ocean because it is highly soluble. If an initially desiccated planet beyond the HZ were to recover habitability via outgassing and maintain a warm temperature, other gases would be needed to support a strong greenhouse. Greenhouse gas abundances can also be affected by energetic particle events, which can drive chemistry that generates trace amounts of greenhouse gases (Airapetian et al. 2016). These events are likely to remove greenhouse gases, by the destruction of O_3 in

Earth-like atmospheres by repeated flaring (Tilley et al. 2017) or by the destruction of CH_4 , which may form hydrocarbon hazes if oxygen radicals are not present (Arney et al. 2017). In the absence of sufficient greenhouse gases, the coldest atmospheres (particularly the 10 bar cloudy, Venus-like h) may be subject to collapse, but most will be resistant, as the condensation temperature for O_2 is very low and day–night temperature contrasts are lower in thicker atmospheres (Turbet et al. 2018).

Our results indicate that the interplay between stellar irradiation, photochemistry, chemical kinetics, and condensation shaped our simulated planetary atmospheric compositions, with water vapor, ozone, sulfur species, and aerosols displaying the greatest variation. The decreases in H_2O (largely due to temperature) and increases in O_3 abundance (due to an interplay between photolysis rates, water abundance, and vertical transport) as a function of orbital distance are consistent with trends found by previous studies (e.g., Grenfell et al. 2007). The water vapor profile in the warmer atmospheres is representative of planets in a moist greenhouse state, with substantial water vapor well mixed throughout the atmosphere and with no cold trap. Consequently, these atmospheres may suffer severe water loss over gigayears, unless the escape rate is balanced by outgassing. Unless they begin with warm, Venus-like atmospheres, the outer planets are too cold to recover from freezing temperatures without a brightening star or larger inventories of greenhouse gases, which may eventually accumulate from outgassing or impactor delivery.

Ozone and CO both exhibit characteristic patterns across our modeled atmospheres. In those containing $\gtrsim 0.2$ bar O_2 , at ~ 200 Pa, O_3 is about 10^{-5} mol/mol in all of the simulated atmospheres, despite different levels of irradiation, H_2O , and O_2 . Above this layer, the O_3 abundance is controlled by photolysis, while below, mixing and other temperature- and water-dependent loss mechanisms dominate. In desiccated atmospheres, CO abundance is controlled by the slow three-body CO_2 recombination reaction (Gao et al. 2015), while in atmospheres with water vapor, the abundance of CO is controlled by the availability of H-bearing recombination catalysts, which are more prevalent near the planetary surface, removing the CO at lower altitudes. Large amounts of CO in the presence of O_2/O_3 are a false positive discriminant

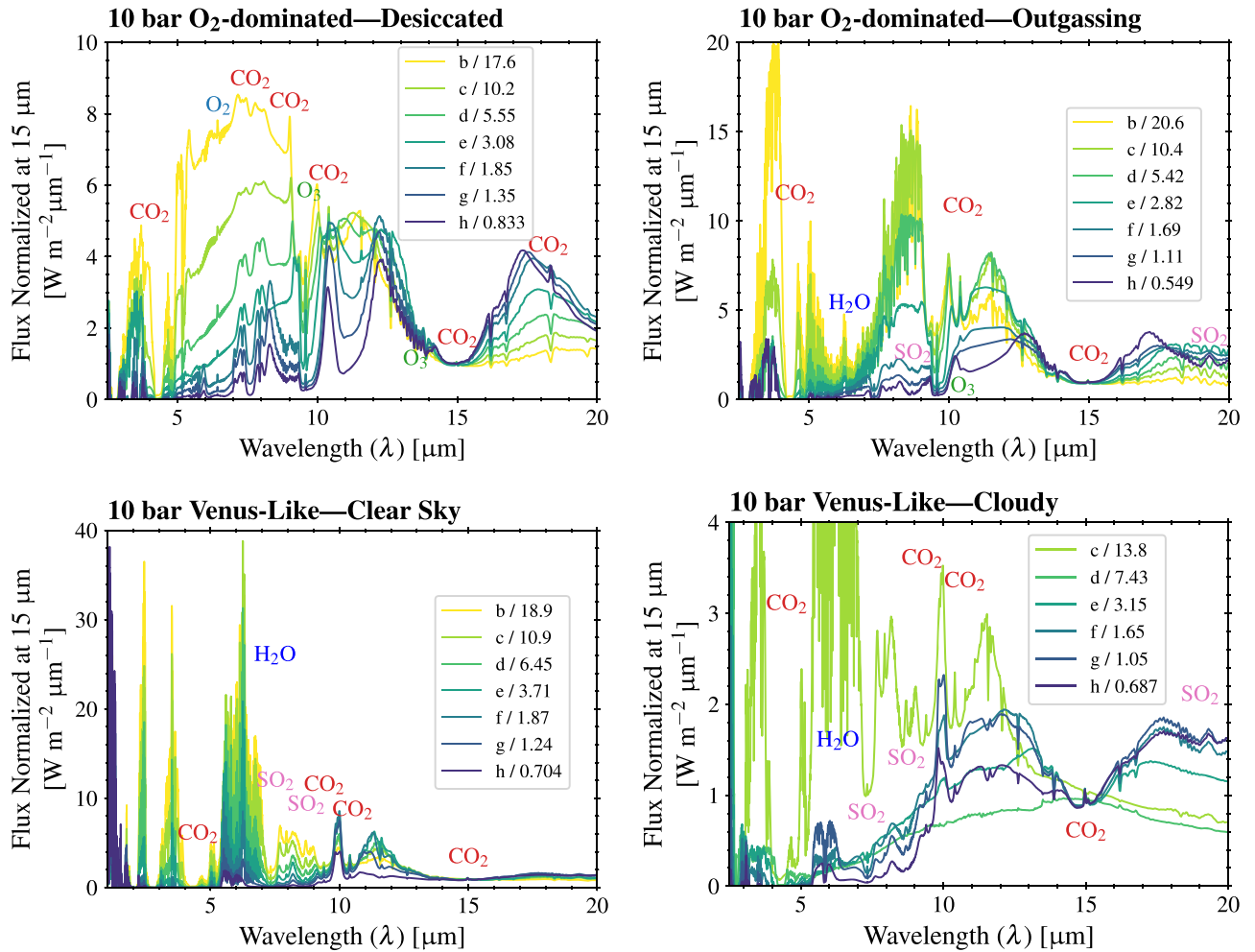


Figure 12. Normalized emission (outgoing flux) spectra for the desiccated atmospheres. The legends provide the factors by which the spectra were reduced to normalize the flux to 15 μm for each. The emission spectra are dominated by CO₂ features in both absorption and emission, but also include H₂O, O₃, and SO₂.

(Schwieterman et al. 2016), indicating that oxygen is more likely to have been generated by photolysis of CO₂ (Gao et al. 2015) rather than photosynthesis.

Aerosols affect the planetary climates by reflecting incoming stellar radiation and either absorbing, emitting, or scattering thermal radiation. Sulfuric acid aerosols can reduce the surface temperatures of hot, partly desiccated planets, which caused the cloudy Venus-like atmospheres we modeled to drop by up to nearly 200 K (Figure 4) compared to the clear-sky cases. Sulfuric acid production also varied as a function of irradiation. The warmer planets more easily formed H₂SO₄ due to higher water vapor abundances and more rapid SO₂ photolysis. This production was offset at lower altitudes by thermal decomposition. TRAPPIST-1 b did not condense sulfuric acid in our model because atmospheric temperatures were too high. If any of the TRAPPIST-1 planets have Venus-like atmospheres, we expect that b will not form sulfuric acid clouds, but the other planets likely would. Although we did not model the radiative effects of aerosols for the O₂ outgassing environments, sulfuric acid condensation occurred in the photochemical model, so their climates could also be affected by these clouds. Water and water-ice clouds impacted the temperature structure of the aqua planet, but had little effect on surface temperature (Figure 8). This was due to competing effects as stellar radiation interacted with the cloud properties: the upper tropospheric cirrus clouds

effectively scatter stellar radiation, but the absorption properties of water and water-ice in the NIR also make them effective absorbers of M dwarf peak stellar radiation, especially given the spectral energy distribution of TRAPPIST-1. Exoplanet aerosols for terrestrial planets are a rich field for future study.

The parameter space for possible planetary characteristics is large, so the assumptions regarding atmospheric surface pressure, surface material, atmospheric bulk composition, geological or biological surface fluxes, and atmospheric transport can have a large impact on the equilibrium atmospheric state. The differences between our O₂ desiccated and outgassing atmospheres demonstrate the effects of surface fluxes on the planetary environment. These factors are important when considering what atmospheres may be possible on a given exoplanet, and for comparing possible planetary states and among different models. Wolf (2017) found that TRAPPIST-1 e requires more CO₂ than Earth to sustain temperate conditions, but that work underestimated the reduction in bolometric albedo due to the late M dwarf SED (Turbet et al. 2018). It is possible that Turbet et al. (2018) also overestimated the surface albedos of ocean-dominated TRAPPIST-1 planets, as they calculated a mean water-ice albedo of 0.21. We used wavelength-dependent surface albedos in our climate calculations that depend on the planetary environment (Figure 1). We found that both pure ocean and melting ice

Table 4
Observational Discriminants

| Planetary state | Molecules and wavelengths [μm] | Notes |
|---------------------------|---|---|
| Aqua planet, clear sky | CO_2 (1.6, 2.0, 2.8, 3.6, 3.8, 4.3, 4.8, 9.5, 10.5, 15), H_2O (0.94, 1.4, 1.9, 2.6, 3, 3.3, 6.3), HDO (3.7), O_2 (0.67, 0.76, 1.27), O_2-O_2 (1.06, 1.27), O_3 (0.6, 4.75, 9.6), CH_4 (2.35, 3.3, 7.6), N_2-N_2 (4, 4.6) | Earth-like worlds may be discriminated by CH_4 in conjunction with oxidized species |
| Aqua planet, cloudy | CO_2 (1.6, 2.0, 2.8, 3.6, 3.8, 4.3, 4.8, 9.5, 10.5, 15), H_2O (1.4, 1.9, 2.6, 3, 3.3, 6.3), HDO (3.7), O_2 (0.67, 0.76, 1.27), O_2-O_2 (1.06, 1.27), O_3 (0.6, 4.75, 9.6), CH_4 (2.35, 3.3, 7.6), N_2-N_2 (4, 4.6) | Tropospheric water/water-ice clouds are problematic for observing Earth-like planets |
| O_2 , desiccated | CO_2 (1.6, 2.0, 2.8, 3.0, 3.2, 3.6, 3.8, 4.0, 4.3, 4.8, 7.3, 7.9, 15), O_2 (0.67, 0.76, 1.27, 6.4), O_2-O_2 (1.06, 1.27), CO (2.35, 4.6), O_3 (0.6, 2.5, 3.3, 3.6, 4.75, 9.0, 9.6, 13) | A lower limit of O_2 abundance can be constrained with the O_2-O_2 bands at 1.06 and 1.27 μm . CO and O_3 levels can indicate desiccation. Complete lack of water vapor |
| O_2 , outgassing | CO_2 (1.6, 2.0, 2.8, 3.0, 3.2, 3.6, 3.8, 4.0, 4.3, 4.8, 15), H_2O (1.4, 1.9, 2.6, 3, 3.3, 6.3), HDO (3.7), O_2 (0.67, 0.76, 1.27, 6.4), O_2-O_2 (1.06, 1.27), O_3 (0.6, 3.3, 3.6, 4.75, 9.6, 13), SO_2 (4.0, 7.3, 8.8, 19) | Water vapor is prominent in the hotter atmospheres |
| Venus-like, clear sky | CO_2 (1.05, 1.3, 1.6, 2.0, 2.8, 3.0, 3.2, 3.6, 3.8, 4.0, 4.3, 4.8, 7.3, 7.9, 9.5, 10.5, 15), H_2O (1.4, 1.8, 2.6, 6.3), CO (2.35, 4.6), SO_2 (4.0, 7.3, 8.8, 19) | High CO_2 abundance may be constrained by the weakest bands (e.g., 1.05 and 1.3 μm) |
| Venus-like, cloudy | CO_2 (1.5, 2.0, 2.8, 3.0, 3.2, 3.6, 3.8, 4.0, 4.3, 4.8, 7.3, 7.9, 9.5, 10.5, 15), H_2O (6.3), SO_2 (4.0, 7.3, 8.8, 19), H_2SO_4 (3.1–4, 7.5–10) | Sulfuric acid cloud absorption may be the best discriminant for outgassed conditions with no surface water |

Note. Spectral features present in transmission or emission spectra are listed for our modeled environments.

surfaces had very low stellar flux-weighted average albedos (0.02 and 0.03 respectively), while a typical snow surface averaged only 0.16 around TRAPPIST-1. Wolf (2017) found that 0.1 bar of CO_2 with 1 bar N_2 is required for a surface temperature of ~ 270 K, while modern Earth CO_2 levels of ~ 400 ppm yield 240 K. Turbet et al. (2018) calculated 250 K under similar conditions, while we find that with or without clouds, only preindustrial Earth CO_2 abundance of 280 ppm is required in a 1 bar N_2/O_2 atmosphere on an ocean-covered planet to reach an Earth-like globally averaged surface temperature. It is crucial to note that surface albedo is one of the primary drivers of climate state (Godolt et al. 2016), particularly in an atmosphere transparent to its host star’s radiation.

4.3. Observational Discriminants of Evolved Terrestrial Atmospheres

Here we compare spectra derived from the complete set of simulated atmospheres for TRAPPIST-1 b, c, and d, whose higher temperatures make them more easily observable, and e, which is a potentially habitable candidate, to identify observational characteristics that could be used to discriminate between these environments and their evolutionary histories. Spectral features that can be used to discriminate between the modeled environments are given in Table 4. Figure 14 shows spectra for the atmospheres we modeled for TRAPPIST-1 b, c, and d. The stronger carbon dioxide bands are prominent in all of our planetary spectra, regardless of whether CO_2 is a bulk constituent or a trace gas, and these CO_2 bands are therefore a good indicator of the presence of a terrestrial atmosphere, but are not as useful for discriminating among different environments. However, if the weaker CO_2 bands are also present, this does indicate a higher, more Venus-like abundance. As seen in planet d’s transmission spectra in Figure 14, cloudy, Venus-like atmospheres are well discriminated by sulfuric acid absorption longward of 3 μm (though these clouds could also form in O_2 -dominated atmospheres with outgassing).

The massive O_2 atmospheres may reveal themselves in transmission via the presence of O_2-O_2 collision-induced absorption at 1.06 and 1.27 μm (Schwieterman et al. 2016), a wavelength region strongly backlit by the host star. Note that

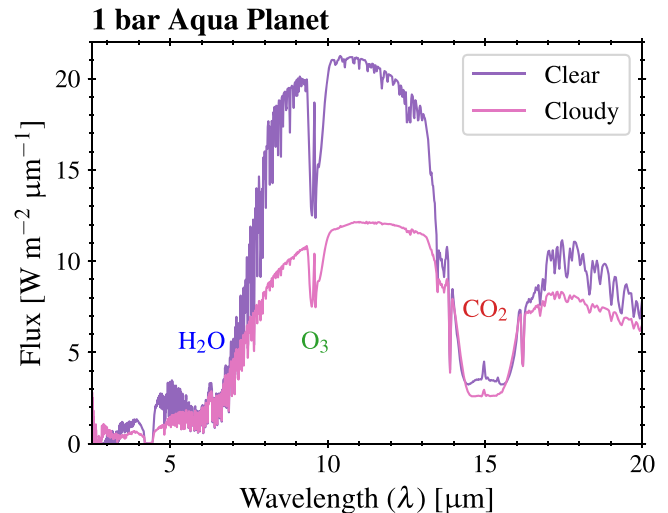


Figure 13. Outgoing flux spectra for clear-sky and cloudy 1 bar TRAPPIST-1 e aqua planets. These closely resemble Earth’s emission spectrum (see Robinson et al. 2011), characterized by the 6.3 μm water band and weak water features throughout and the 15 μm CO_2 band. The weak water features mostly disappear in the cloudy case, and the overall emission spectrum is reduced in magnitude by half.

our photochemical model suggests that cloud formation in the outgassing atmosphere is likely due to sulfuric acid condensation (at ~ 1 ppb concentration). However, this will not affect the visibility of the O_2-O_2 features since the aerosol scattering properties and geometry of the TRAPPIST-1 system permit transmission shortward of 2.5 μm for the innermost planets. The favorably compact geometry of the TRAPPIST-1 system allows transit transmission to probe relatively deep into the atmosphere, where O_2-O_2 absorption is strongest, producing transit signals as high as 70 ppm (versus ~ 3 ppm for an early-type M dwarf; Schwieterman et al. 2016). However, as demonstrated in the inset in Figure 14, the broad O_2-O_2 bands at 1.06 and 1.27 μm overlap with CO_2 bands at 1.05, 1.13, 1.24, 1.29, and 1.32 μm in high CO_2 atmospheres. An atmosphere with high levels of both CO_2 and O_2 may be common if a planet that experienced complete ocean loss retained a large fraction of the CO_2 that was dissolved in the

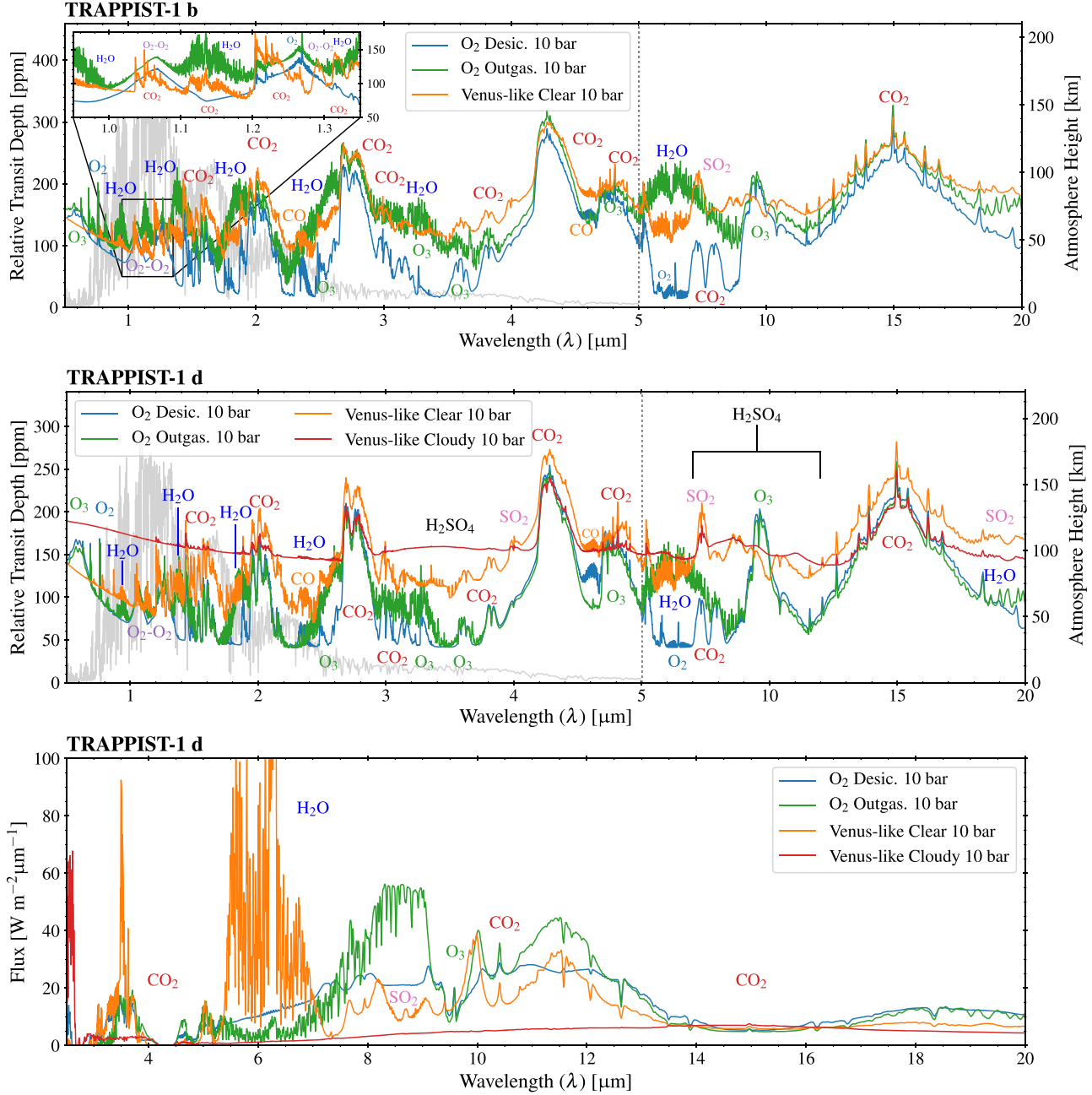


Figure 14. TRAPPIST-1 b (top panel) and d (center panel) transit transmission spectra, and TRAPPIST-1 d thermal emission spectra (bottom panel) of the 10 bar atmospheres, for all environments simulated. The higher mass environments exhibit similar spectral features, but different strengths and temperatures. We include the stellar spectrum (gray) in the transmission plots to illustrate the spectral regions with the most available photons for backlighting the atmosphere in transmission. As shown in the previous figures, CO₂ dominates all of these environments. Absorption by O₂-O₂, O₃, SO₂, CO, H₂O, and weaker CO₂ bands can distinguish these environmental states in both transmission and emission. Note the inset for b that shows the overlapping CO₂ and O₂-O₂ bands that could be confused at low resolution. The H₂O feature of the clear-sky, Venus-like atmosphere in emission peaks at $\sim 420 \text{ W m}^{-2} \mu\text{m}^{-1}$. TRAPPIST-1 b is scheduled to be observed by *JWST* and has the strongest features, due to lower gravity and hotter temperatures. Planet d also has a strong signal in transmission, even with high-altitude sulfuric acid aerosols. TRAPPIST-1 b, c, and d exhibit strong features in emission due to high temperatures; d is shown here in emission to demonstrate the large difference due to aerosols.

oceans or subsequently outgassed from the interior. These weak CO₂ features could confuse retrieval and interpretation of the O₂-O₂ features without sufficient resolution, signal-to-noise ratio, or corroboration from stronger CO₂ features elsewhere in the spectrum.

These O₂-dominated spectra also show strong features from O₃ and SO₂. A strong ozone Chappuis band around $\sim 0.6 \mu\text{m}$ may indicate desiccation, as it traces ozone deep in the atmosphere, where water vapor would normally destroy it

(Meadows et al. 2018a). As clearly shown in Figure 14 in all three panels, the $9.6 \mu\text{m}$ O₃ feature is strong and broad for both O₂-rich atmospheres, but not present in the Venus-like spectra primarily due to the lack of O₂ in the atmosphere. Detection of SO₂ absorption in either transmission or emission would be indicative of an outgassing interior, and possibly an atmosphere and surface with low water abundance, due either to early desiccation or temperatures below freezing. The O₂ outgassing case is unique among the environments considered for the

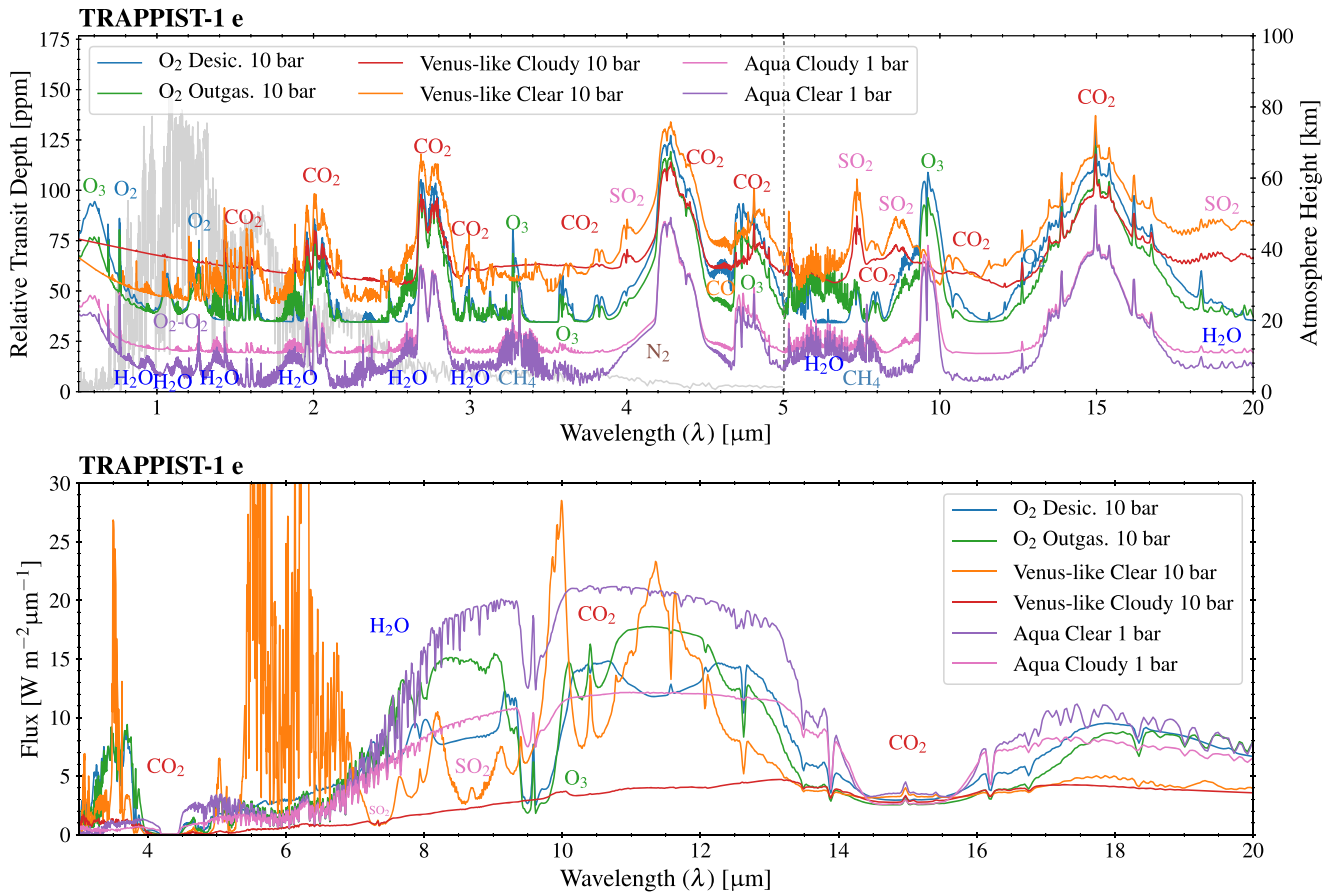


Figure 15. TRAPPIST-1 e transit transmission (top panel) and thermal emission (bottom panel) spectra of the 10 bar atmospheres for the four simulated evolved environments and the two aqua planet environments. The higher mass environments exhibit similar spectral features, but different strengths and temperatures. We include the stellar spectrum (gray) in the transmission plot to illustrate the spectral regions with the most available photons for backlighting the atmosphere in transmission. As shown in the previous figures, CO₂ dominates all of these environments. Absorption by O₂–O₂, O₃, H₂O, and weaker CO₂ bands can distinguish these environmental states in both transmission and emission. The H₂O feature of the clear-sky Venus-like atmosphere in emission peaks at $\sim 60 \text{ W m}^2 \mu\text{m}^{-1}$.

hotter planets in showing very strong water features, especially near 1.4 and 6.3 μm . This is because these planets have high levels of water vapor (up to 0.1% mol/mol) in their stratospheres, so they are in a moist greenhouse state, approaching a runaway greenhouse. These strong H₂O bands are indicative of a planet in the process of losing water vapor, rather than indicating habitable, ocean-bearing conditions.

The bottom panel of Figure 14 demonstrates the differences between the evolved environments in emission using TRAPPIST-1 c as an example of the hotter planets. The water band at 6.3 μm is the primary discriminant. At high temperatures and high abundance (e.g., the O₂ outgassing case), H₂O absorption can dominate over absorption from other interesting molecules at 5–9 μm , such as O₂, SO₂, and CO₂. For the Venus-like, clear-sky atmosphere, the low abundance of H₂O $\lesssim 1$ ppm fails to suppress the outgoing radiation from the hot lower atmosphere, resulting in an emission peak at these wavelengths. The cloudy Venus case shows that clouds can adversely affect both outgoing flux and the strength of molecular features by truncating the atmosphere at higher, colder altitudes.

Figure 15 compares the spectra of the O₂- and CO₂-dominated atmospheres with the clear and cloudy aqua planets for TRAPPIST-1 e. The relative transit depths are naturally offset by the truncating effects of clouds, which allow transmission to probe only altitudes above the cloud deck, and the obscuring effect of atmospheric opacity for atmospheres of different total atmospheric

pressure (i.e., 1 versus 10 bar). In the thermal infrared, clouds reduce the overall outgoing flux by emitting at colder temperatures. The O₂ desiccated and Venus-like atmospheres for TRAPPIST-1 e display features and corresponding observational discriminants similar to the hotter planets. However, the O₂ outgassing environment was not hot enough to maintain high levels of stratospheric H₂O, so it exhibits a more Earth-like, modestly absorbing 6.3 μm feature. The overall emission spectrum of that environment is very similar to that of aqua planets, but with additional CO₂ bands due to the higher levels of CO₂ we assumed.

Water is not a good discriminant among some of these atmospheres, so discriminating the habitable aqua planet from the uninhabitable environments is not straightforward. The aqua planet has water vapor features in the near-infrared in transmission at 0.94, 1.15, 1.4, 1.9, 2.6, 3.7, and most strongly at 6.3 μm . Unfortunately, these water features have comparable signals among the clear-sky atmospheres (except the completely desiccated case), and among the cloudy cases, despite vastly different levels of tropospheric H₂O, due to the cold trapping of water in the aqua planet atmosphere.

The bulk composition of these atmospheres can potentially be distinguished by weak spectral effects of their dominant gases O₂, CO₂, and N₂. The Earth-like aqua planet atmosphere exhibits absorption from the collision-induced N₂–N₂ band at 4.1 μm , which is sensitive to the partial pressure, and could be diagnostic of atmospheric pressure if this challenging

observation could be made (Schwieterman et al. 2015). At high abundances of CO₂ (as low as 0.5 bar here), the wings of the 4.3 μm CO₂ band overpower the N₂–N₂ CIA. The presence of the weak NIR–MIR CO₂ bands (including the numerous bands shortward of 2 μm , the ¹⁶O¹²C¹⁸O isotopologue absorption bands at 3.6, 3.8, 4.0, 7.3, and 7.9 μm , and hot bands at 9.5 and 10.5 μm) is indicative of a warm, CO₂-rich atmosphere. As in Earth’s atmosphere, O₂–O₂ CIA is weakly present in the aqua planet atmospheres, but the bands are considerably stronger at higher O₂ abundance, which would suggest that an abiotic, post-ocean-loss source for the oxygen was more likely.

Potentially habitable environments may be constrained by indicators of desiccation, such as O₃, SO₂, and CO, as these gases react with water vapor and its photolytic by-products. Both the modeled O₂-dominated and aqua planet atmospheres exhibit ozone absorption at 0.6 and 9.6 μm . However, a strong indication of desiccation is high ozone abundance, as constrained by the presence of a long wavelength tail of the Chappuis band (out to 1 μm), the 2.5 and 3.6 μm features, and additional weak bands at 9 and 13 μm , which arise in the O₂ cases, particularly the colder and desiccated environments. Retrievals of ozone abundances in conjunction with climate and photochemical modeling could help constrain the likely abundances of tropospheric water vapor. The detection of SO₂ would also suggest a desiccated atmosphere, because SO₂ easily combines with H₂O to form sulfuric acid. The presence of CO, if not masked by CO₂ or O₃, would indicate desiccation because H₂O photolytic by-products such as hydroxyl are efficient catalysts at recombining CO₂ from CO and free oxygen. While the absence of water vapor absorption does not necessarily indicate the lack of tropospheric water vapor or surface water, desiccation indicators from O₃, SO₂, and CO, even with weak water vapor features, would suggest a desiccated and likely uninhabitable environment.

Signs of atmospheric escape and ocean loss may be probed by observing isotopologue bands HDO and ¹⁸O¹²C¹⁶O. Measuring the D/H ratio in H₂O and the ¹⁸O/¹⁶O ratio in CO₂ could be used to probe isotopic fractionation, which occurs during atmospheric escape and ocean loss because lighter elements are preferentially lost over heavy elements (e.g., Hunten 1982). D/H fractionation from atmospheric loss has been measured for both Venus (D/H \sim 120 versus Earth; De Bergh et al. 1991) and Mars (D/H \sim 4 versus Earth; Encrenaz et al. 2018). In particular, such D/H fractionation would indicate an environment that had the majority of its ocean reservoir depleted (Hunten 1982). Future work should assess oxygen fractionation due to massive ocean loss in an environment with some retained atmospheric oxygen.

4.4. Planetary System Effects on Terrestrial Atmospheres and Spectra

Our results and those of others demonstrate that the atmospheres and surfaces of M dwarf terrestrials have likely been strongly shaped by several factors, including stellar evolution, atmosphere and ocean loss, photochemistry, and geological (and biological) surface fluxes (Segura et al. 2005; Grenfell et al. 2014; Rugheimer et al. 2015; Meadows & Barnes 2018; Meadows et al. 2018a). In particular, interior outgassing and photochemistry are key processes for modeling terrestrial exoplanets, as both drive disequilibria in the atmosphere. Our results show a strong effect from outgassing, such as

from SO₂ and H₂O, which, together with their photochemical by-products and reactions with other species, shape the temperature inversions and lapse rates as well as produce radiative greenhouse (and antgreenhouse) effects. Although our environments do not explicitly contain biogenic fluxes, surface fluxes from life processes also drive disequilibria, and this is one of the principal means that will be used to search for life on exoplanets (Simонcini et al. 2013; Krissansen-Totton et al. 2016; Meadows 2017). Photochemistry is critically important in assessing planetary composition and in understanding the formation and destruction of key species, some of which may be outgassed or biogenic. As we have shown, this is especially true for planets at different orbital distances, including those orbiting M dwarfs, where the alien UV spectrum can drive chemistry that the Sun does not induce in the Earth’s atmosphere. The species outgassed or generated from photochemistry may be directly observed, and their vertical distribution may affect other gas absorption features because of their effects on climate.

To illustrate the effects of modeling factors—including outgassing and photochemistry—on predicted spectra, we directly compare a sampling of our spectra for TRAPPIST-1 d and e with Morley et al. (2017), who used radiative transfer and thermochemical equilibrium models to conduct a broad assessment of spectroscopic observables for the TRAPPIST-1 planets. For planet d, we compare our radiative–convective/photochemical equilibrium 10 bar clear-sky and cloudy Venus-like atmospheres with the Venus-like atmospheres from Morley et al., identified by their albedos ($A = 0.0, 0.3$, and 0.7), which correspond to clear-sky to global cloud coverage (Figure 16). The spectra of clear-sky, Venus-like atmospheres modeled in both approaches are similar in both transmission and emission, except for stronger SO₂ features from the thermochemical model, which are reduced in our model (and Venus’s true atmosphere) by H₂SO₄ formation. The SO₂ in the thermochemical model suppresses outgoing flux at wavelengths of 7–10 μm when compared to both our clear and cloudy atmospheres. Although the integrated flux of the $A = 0.0$ atmosphere is very close to that of our clear-sky Venus, the distribution of flux is different. Our absorption features are not as deep (e.g., 7–9 μm), which is likely due to our atmospheres having warmer stratospheres. Our atmospheres also show higher emission near 6 μm because weaker water vapor absorption permits escape of radiation from the hot lower atmosphere. This is likely due to different assumptions about the water vapor profile between the two models.

Our spectra differ considerably from Morley et al. (2017) for cloudy Venus-like cases. Photochemical models produce results tailored to the spectrum of the host star, whereas thermochemistry is driven purely by the atmospheric temperature profile at a given orbital position and so is more generic. The cloudy Venus differs significantly from the clear-sky case in both transmission and emission due to the truncation of the atmospheric column by cloud scattering and absorption at higher, colder altitudes, which reduce the outgoing thermal flux and can raise the tangent height when observed in transmission. Although the effects of clouds on surface temperature can be approximated by changing the Bond albedo in the thermochemical models, this process does not take into account the radiative effect of the clouds on the temperature profile or on transmission and emission spectra. Sulfuric acid scattering and absorption in the cloudy Venus-like transmission spectrum, and emission from the cloud deck in direct

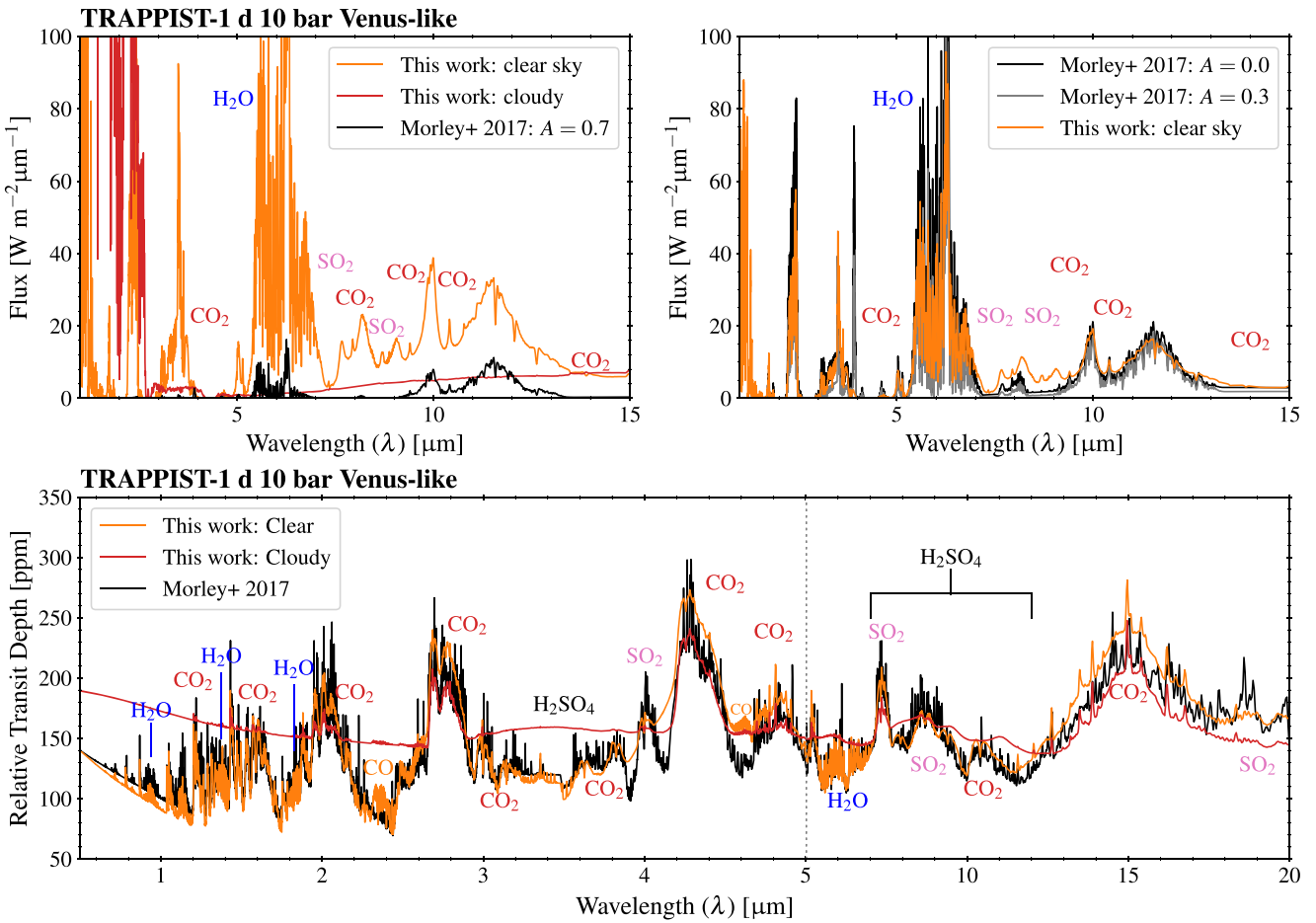


Figure 16. Comparison spectra of the 10 bar TRAPPIST-1 d Venus analogs. To directly compare, Morley et al. (2017) spectra were sampled at 1 cm^{-1} and convolved with a 1 cm^{-1} half-width at half-maximum slit function. Upper left panel: our clear-sky and cloudy Venus spectra compared to the high-albedo ($A = 0.7$) thermochemical equilibrium Venus of Morley et al. (2017). The radiative effects of sulfuric acid aerosols are much more complex than their effect on planetary albedo. The planet effectively emits from the cloud deck, which is not captured in models that assume a higher surface albedo to account for clouds. Upper right panel: Our clear-sky Venus is qualitatively similar to the lower albedo ($A = 0.0\text{--}0.3$) of Morley et al. (2017). Lower panel: transmission spectra showing relative transit depth. Clouds substantially impair the ability to observe gas absorption features. The strong SO_2 features in the Morley et al. spectra are likely due to uniform vertical gas profiles and colder emission temperatures.

imaging or secondary eclipse, are distinctive features of a Venus-like planet not captured in models without vertical cloud distributions.

As shown in Figure 17, the Earth-like atmospheres also show significant differences in composition between the two modeling approaches, primarily because we include the effects of water vapor clouds, photochemically produced gases such as O_3 , and outgassed species such as CH_4 . These characteristic features of Earth’s spectrum are not seen in the spectra generated by Morley et al. (2017) using a thermochemical equilibrium model. Our photochemically consistent clear-sky aqua planet atmosphere also produces significantly stronger water vapor absorption bands (likely due to the inclusion of HDO isotopologue absorption at 3.6 and $9\text{ }\mu\text{m}$), although the cloudy case is perhaps the more realistic model.

4.5. Assessing Current and Future Observations

Several preliminary observational constraints on atmospheric composition have been obtained of planets in the TRAPPIST-1 system, to which we can compare our modeling results. Spectra taken with the *Hubble Space Telescope* (de Wit et al. 2016, 2018) ruled out low-molecular-weight atmospheres, although

these spectra were also consistent with flat spectra within the error bars of $\sim 200\text{--}350\text{ ppm}$. For TRAPPIST-1 b, Delrez et al. (2018) observed a signal difference of $208 \pm 110\text{ ppm}$ between the 3.6 and $4.5\text{ }\mu\text{m}$ *Spitzer* bands, which they suggest is due to CO_2 absorption. These results, and the *K2* photometry from the Gillon et al. (2017) discovery paper, are shown with error bars in Figure 18, along with the band-integrated transit depths for our modeled spectra. We have adjusted the assumed solid body radius in these spectra to fit the observations for the solid body and wavelength-dependent atmospheric absorbing radius. Our simulated spectra are consistent with these data within 2σ error, and the O_2 -dominated atmospheres fit within 1σ . The $3.6\text{ }\mu\text{m}$ filter bandpass contains absorption by the CO_2 isotopologue bands at 3.6 , 3.8 , and $4.0\text{ }\mu\text{m}$, plus the wings of the main isotopologue $4.3\text{ }\mu\text{m}$ band, whereas the $4.5\text{ }\mu\text{m}$ filter bandpass contains the 4.3 and $4.9\text{ }\mu\text{m}$ CO_2 , $4.6\text{ }\mu\text{m}$ CO , and $4.75\text{ }\mu\text{m}$ O_3 bands. Rayleigh scattering and ozone absorption may contribute to the larger transit depth measured by *K2*. A different distribution of UV flux than assumed in this work could enhance ozone levels, further increasing the transit depth in the *K2* band and the *Spitzer* $4.5\text{ }\mu\text{m}$ band.

Our simulated atmospheres are consistent with the observed data, but do not agree with the atmospheric scale height and

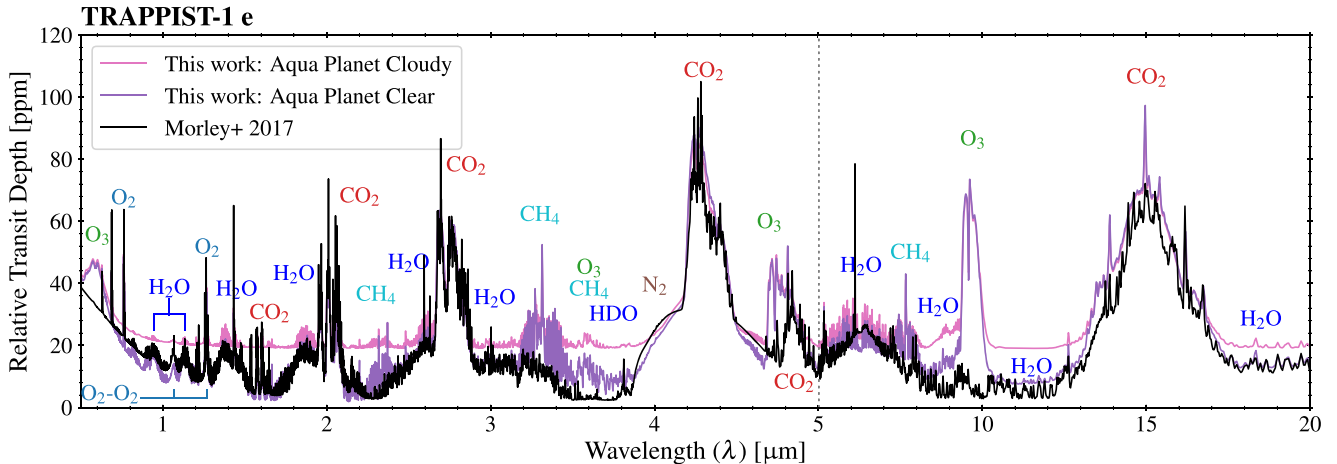


Figure 17. Transmission spectra of the 1 bar TRAPPIST-1 e Earth analogs: our aqua planet with Earth geological outgassing compared to the thermochemical equilibrium Earth of Morley et al. (2017; sampled at 1 cm^{-1} and convolved with a 1 cm^{-1} half-width at half-maximum slit function, scaled to 30% and offset for this plot). The Morley et al. atmospheres do not have O_3 , an abundant stratospheric photochemical by-product of O_2 , or CH_4 , which together are the most distinctive observational features of Earth (Selsis et al. 2002; Schwierman et al. 2018).

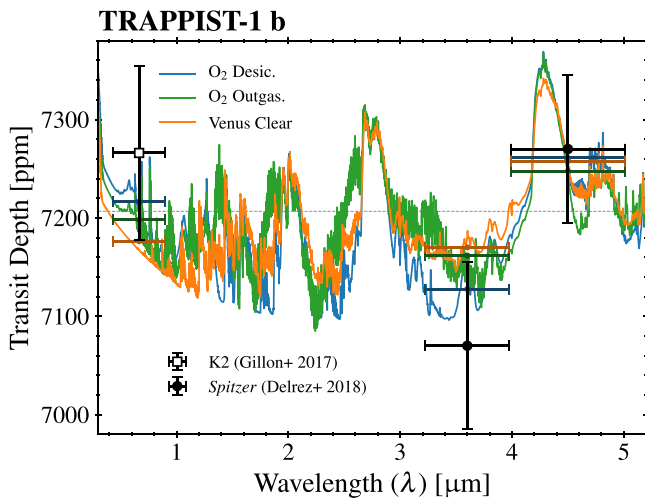


Figure 18. Comparison of available photometric transit data from *K2* and *Spitzer* (Gillon et al. 2017; Delrez et al. 2018) with our 10 bar model spectra for TRAPPIST-1 b. The colored points correspond to our model spectra convolved with the appropriate photometric filters. A vertical offset is applied to each model transmission spectrum so that the models optimally overlap the observations. These offsets correspond to the difference between our assumed radius for TRAPPIST-1 b and the solid body radius assuming a model atmosphere and its associated absorbing radius above the surface. The offsets are -293 km for the desiccated O_2 , -308 km for O_2 with outgassing, and -312 km for the clear-sky Venus. The desiccated, O_2 -dominated atmospheres fit the *Spitzer* data within 1σ , while the Venus-like atmosphere fits within 2σ .

temperature derived by Delrez et al. (2018) for TRAPPIST-1 b. Delrez et al. assumed that the 208 ppm transit signal between the observed *Spitzer* bands was due to two scale heights from the CO_2 signal in an Earth-like atmosphere—with mean molecular mass 28 g mol^{-1} , CO_2 as the only absorbing gas, and excluding CH_4 and H_2O , which have transitions in the $3.6\text{ }\mu\text{m}$ band. However, their derived temperature of 1400 K and scale height of 52 km (1800 K and 100 km with water vapor included) are not consistent with the assumption of an Earth-like atmosphere. Our self-consistent modeled environments, which include a case with a greenhouse comparable to that of Venus, have emission temperatures that vary with wavelength ($325\text{--}575\text{ K}$; Figure 19) but overall stay close to

the equilibrium temperature ($\sim 400\text{ K}$; Gillon et al. 2017), even though they have surface temperatures spanning $406\text{--}714\text{ K}$.

In Figure 20, we show that the scale heights at the effective transit altitude for our modeled atmospheres vary considerably as a function of wavelength and are within values typical of solar system terrestrials (i.e., $8\text{--}16\text{ km}$ for Venus and Earth; Meadows & Crisp 1996), spanning $\sim 9\text{--}11$ scale heights (3–5 scale heights when convolved with the *Spitzer* bands), and are consistent with the *Spitzer* observations. Scale height inferences from the size of potential features are degenerate with temperature, species, abundances, aerosols, and opacities, and so are difficult to accurately assess without properly accounting for a range of atmospheric possibilities within a retrieval framework (e.g., Line et al. 2013).

If the existence of an exoplanetary M dwarf terrestrial atmosphere is confirmed, near-term observations will provide constraints on the environmental effects of M dwarf stellar evolution on orbiting planets as a function of distance from the star and position in the habitable zone. Our modeling work provides hypotheses for planetary states as a result of evolution and composition that could be tested by these upcoming observations, which may constrain atmospheric temperatures and species abundances using the discriminants we have presented. In a subsequent paper, we will use the modeled planetary states and spectra with instrument noise models to predict observational requirements to distinguish the current composition and evolutionary histories of the TRAPPIST-1 planets.

5. Conclusions

We have calculated the possible ocean loss and oxygen accumulation for the seven known TRAPPIST-1 planets, modeled potential O_2/CO_2 -dominated and potentially habitable environments, and computed transit transmission and emission spectra. These evolved terrestrial exoplanet spectra are consistent with broad constraints from recent *HST* and *Spitzer* data.

Our evolutionary modeling suggests that the current environmental states can include the hypothesized desiccated, post-ocean-runaway O_2 -dominated planets, with at least

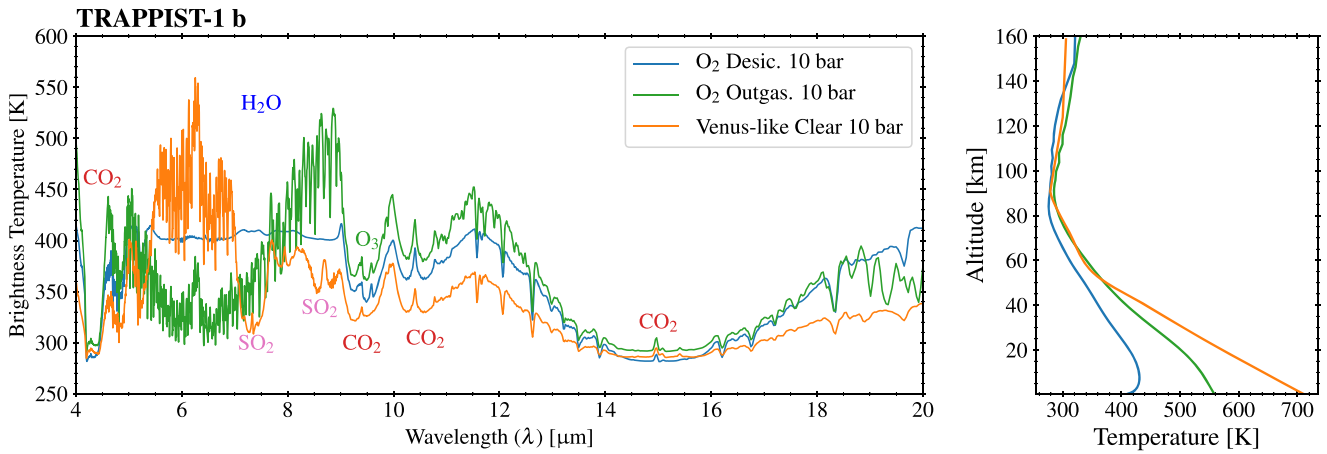


Figure 19. Brightness temperature of emergent flux for all four environments modeled for TRAPPIST-1 b (10 bar). The atmospheric structures are plotted on the right for comparison. Brightness temperature represents emergent flux plotted in units of temperature, which demonstrates the emitting layer temperature as a function of wavelength. As shown by comparing to the temperature profiles, higher brightness temperatures are emitted from lower layers, while lower temperatures represent emission from higher, cooler layers.

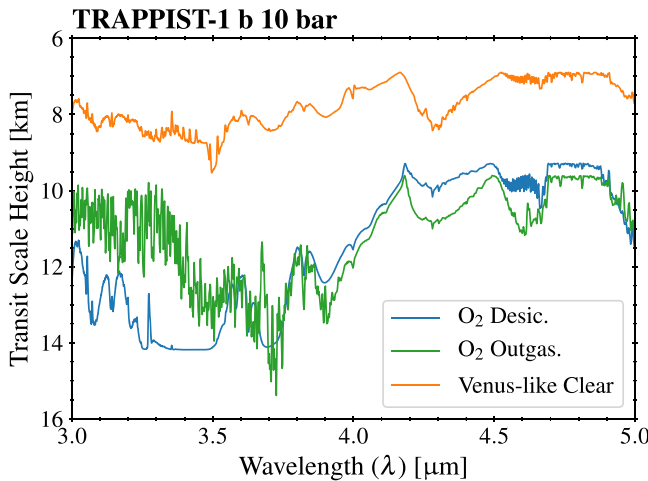


Figure 20. Atmospheric scale heights at the effective transit height in the wavelength range relevant for *Spitzer* for modeled TRAPPIST-1 b atmospheres. The calculated scale heights (7–16 km) are consistent with solar system terrestrials (8–16 km). Transmission spectra sample the stratosphere, where the atmospheres are cooler, so the scale heights are smaller. The O₂-dominated atmospheres are more transparent than the Venus-like atmospheres, so their atmospheres are probed deeper into the hotter regions.

partial ocean loss persisting out to TRAPPIST-1 h. These O₂-dominated atmospheres have unusual temperature structures, with low-altitude stratospheres and no tropospheres, which result in distinctive features in both transmission and emission, including strong collision-induced absorption from O₂.

Alternatively, if early volatile outgassing (e.g., H₂O, SO₂, CO₂) occurred, as was the case for Earth and Venus, Venus-like atmospheres are possible, and likely stable, throughout and beyond the habitable zone, so the maximum greenhouse limit may not apply for evolved M dwarf planets. If Venus-like, these planets could form sulfuric acid hazes, though we find that TRAPPIST-1 b would be too hot to condense H₂SO₄ aerosols.

From analyzing our simulated spectra, we find that there are observational discriminants for the environments we modeled in both transit and emission, with transit signals up to 200 ppm for TRAPPIST-1 b. Detection of CO₂ in all considered

compositions may be used to probe for the presence of a terrestrial atmosphere. We find that the detection of water is not a good indicator of a habitable environment, as Venus-like atmospheres exhibit similar spectral features for water, so the detection of low stratospheric water abundance may be a necessary but not sufficient condition for a habitable environment. The discriminants between these environments involve several trace gases. Careful atmospheric modeling that includes photochemistry and realistic interior outgassing is required to predict the diversity of potentially observable spectral features, to interpret future data, and to infer the underlying physical processes producing the observed features.

Nevertheless, these discriminants may be used to assess the viability of detecting evolutionary outcomes for the TRAPPIST-1 planets with upcoming observatories, particularly *JWST*, and this will be assessed in subsequent work. While specifically applied here to the TRAPPIST-1 system, our results may be broadly relevant for other multiplanet M dwarf systems.

This work was performed as part of the NASA Astrobiology Institute's Virtual Planetary Laboratory, supported by the National Aeronautics and Space Administration through the NASA Astrobiology Institute under solicitation NNN12ZDA002C and Cooperative Agreement Number NNA13AA93A. A.P.L. acknowledges support from NASA Headquarters under the NASA Earth and Space Science Fellowship Program with grant 80NSSC17K0468. This work was facilitated through the use of advanced computational, storage, and networking infrastructure provided by the Hyak supercomputer system at the University of Washington. This work also benefited from our participation in the NASA Nexus for Exoplanet System Science (NExSS) research coordination network. We thank the anonymous reviewer whose thoughtful comments helped us greatly improve the manuscript.

Software: SMART (Meadows & Crisp 1996; Crisp 1997), LBLABC (Meadows & Crisp 1996), VPL Climate (Meadows et al. 2018a; Robinson & Crisp 2018), Atmos Photochem (Kasting et al. 1979; Zahnle et al. 2006; Schwertner et al. 2016), ATMES (Luger & Barnes 2015; Luger et al. 2015), GNU Parallel (Tange 2011).

Appendix A VPL Climate Model Description and Updates

A.1. Radiative Transfer

VPL Climate is based on the line-by-line, multistream, multiple-scattering radiative transfer code SMART (described in Section 2). VPL Climate solves the 1D surface-atmosphere thermodynamic energy equation as an initial value problem using time stepping. To step toward equilibrium in a model atmosphere without incurring the computational penalty of a full radiative transfer calculation at every time step, VPL Climate uses SMART to generate spectrally resolved Jacobians describing the response of the radiative fluxes to changes in temperature and, where applicable, gas mixing ratios. The Jacobians consist of layer-by-layer, line-by-line stellar and thermal source terms and their derivatives, and derivatives of layer reflectivity, transmissivity, and absorptivity. These quantities are used in a linear flux-adding approach to determine heating rates, as developed by Robinson & Crisp (2018). If, at any time step, the atmospheric properties are outside the linear range of the Jacobians, time stepping is suspended, and updated fluxes and layer radiative properties and their Jacobians are recomputed using SMART. High-resolution fluxes from SMART are spectrally binned to 10 cm^{-1} (reflected stellar) or 1 cm^{-1} (emitted thermal) intervals to calculate the stellar heating and thermal cooling in each model layer at each time step.

Spectrally dependent molecular absorption cross sections for rotational–vibrational transitions of gases used by SMART are evaluated using the line-by-line model LBLABC (Meadows & Crisp 1996). LBLABC employs nested spectral grids that fully resolve the narrow cores of individual absorption lines for every atmospheric layer and include the line contributions up to 1000 cm^{-1} from the line center. Cross sections for CO_2 are computed using sub-Lorentzian wings with experimentally determined χ correction factors to simulate the effects of quantum-mechanical line mixing. Lines for H_2O are computed using a line shape model with super-Lorentzian wings to parameterize the far-wing quasi-continuum absorption due to the finite duration of molecule collisions. Opacities for O_2 are computed using super-Lorentzian line wings (Hirono & Nakazawa 1982) with an exponent of 1.958. Line parameters, collision-induced absorption, and UV–visible cross sections are obtained from a variety of sources (see Section 2.6.2).

A.2. Convective Heating

Convective processes transport heat vertically in planetary atmospheres. Convection can result in both sensible heating (related to the energy required to change the temperature of an air parcel due to vertical mixing) and latent heating (related to the energy required to change the phase of a substance, e.g., due to condensation and evaporation). These processes can transport substantial amounts of heat from the surface to the upper troposphere, especially for planets with greenhouse gases, which can prevent the deep atmosphere (or surface) from radiating directly to space. For example, early 1D modeling results showed that convective processes reduce Earth’s surface temperature relative to pure radiative equilibrium conditions by $\sim 50\text{ K}$ (Manabe & Strickler 1964). Convective processes are also responsible for transport of trace species in the atmosphere, substantially altering atmospheric chemistry (e.g., Fleming et al. 1999; Charnay et al. 2015).

In VPL Climate, mixing length theory is used to calculate convective heat fluxes and heating rates, as this approach is more physically rigorous and versatile than the convective adjustment typically used in 1D exoplanet models. Convective adjustment sets the troposphere temperature profile to a moist or dry adiabat defined by Earth’s atmospheric conditions (e.g., Kopparapu et al. 2013; Godolt et al. 2016). In these regimes, convective adjustment does not allow for atmospheric lapse rates that exceed the adiabat, which occurs on planets with more tenuous atmospheres, like Mars (e.g., Hinson & Wilson 2004). Convective adjustment also stabilizes atmospheric layers perfectly at every time step, even if such instantaneous stability is unphysical (e.g., requires convective motions faster than the speed of sound). Furthermore—and especially problematic for coupling to chemistry models—convective adjustment provides no direct insight into the vertical transport of mass in the atmosphere. In contrast, mixing-length theory uses fundamental physical properties of the atmosphere and its constituents (e.g., air parcel temperature, density, specific heat capacities, and static stability) to estimate the vertical heat transport rate, expressed as a vertical “eddy diffusivity,” K . This quantity is then used to calculate the resulting heat and mass fluxes. Mixing-length theory is therefore applicable to a wider variety of atmospheric temperature and composition regimes and can be used to model convection for a diverse range of exoplanet atmospheres.

The convective heating rate is related to the divergence of the convective energy flux:

$$q_c = -\frac{1}{\rho c_p} \frac{\partial F_c}{\partial z}, \quad (5)$$

where z is altitude, c_p is the specific atmospheric heat capacity, and ρ is the air density. The convective energy flux F_c is given by

$$F_c = -\rho c_p K_h \left(\frac{\partial T}{\partial z} + \Gamma_{ad} \right), \quad (6)$$

where K_h is the eddy diffusion coefficient for heat, and the adiabatic lapse rate is $\Gamma_{ad} = g/c_p$, where g is the acceleration due to gravity. The atmosphere is unstable to convection when $\partial T/\partial z > -\Gamma_{ad}$. In this case, the eddy diffusion coefficient for heat K_h is given by

$$K_h = l^2 \left[-\frac{g}{T} \left(\frac{\partial T}{\partial z} + \Gamma_{ad} \right) \right]^{1/2}, \quad (7)$$

where l is the mixing length. The nominal mixing length is given by Blackadar (1962):

$$l = \frac{kz}{1 + kz/l_0}. \quad (8)$$

Here, k is von Kármán’s constant and l_0 is the mixing length in the free atmosphere, which we express as

$$l_0 = f_z H, \quad (9)$$

where H is the pressure scale height, given by

$$H = \frac{RT}{\mu g}. \quad (10)$$

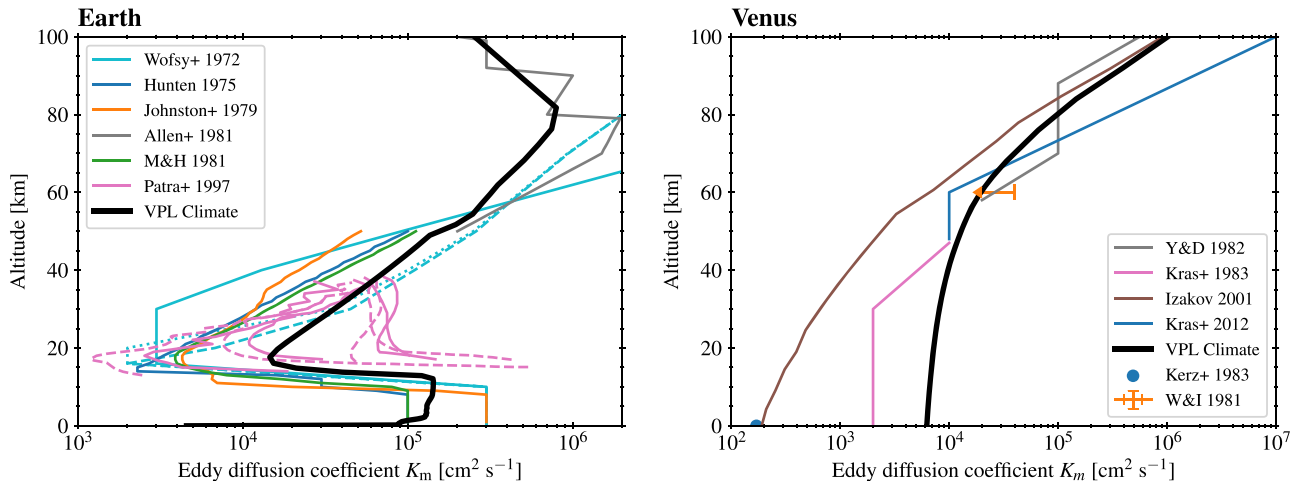


Figure 21. Eddy diffusion profiles for Earth (left panel) and Venus (right panel). For Earth, model fits to observations are shown from Wofsy et al. (1972), Hunten (1975), Johnston et al. (1979), Allen et al. (1981), Massie & Hunten (1981), and Patra & Lal (1997). For Venus, we show two points derived from probes of the atmosphere (Woo & Ishimaru 1981; Kerzhanovich & Marov 1983), profiles used with chemical kinetics modeling to fit tracer species (Krasnopol'sky & Parshev 1983; Krasnopol'sky 2012), and theoretical modeling (Izakov 2001). Observations and studies of eddy diffusion rates vary widely.

Here, R is the ideal gas constant, μ is the mean molar mass, and f_z is the proportionality constant.

The preceding convection parameterization was used by Robinson & Crisp (2018), with $f_z = 1.0$ and with $K_h = 0$ under stable conditions. However, turbulent eddies still provide some vertical mass transport in stable conditions, due to shear instability and gravity wave breaking (e.g., Hodges 1969; Kondo et al. 1978; Lindzen & Forbes 1983; Canuto et al. 2008). Based on measurements of Earth and Venus eddy diffusion rates (see Figure 21), we specify the following parameterization for the eddy diffusion coefficient for mass transport:

$$K_m = K_{m,0}(\rho/\rho_0)^{-1/2}(1 - e^{-P/P_0}) + K_{m,1}\Lambda + K_{m,2}, \quad (11)$$

where Λ is a stability-related parameter that is nonzero only for the aqua planet. To determine Λ , we iterate the following from the surface upward, layer-by-layer:

$$\Lambda_k = \begin{cases} \Gamma/\Gamma_{\text{ad}}, & \text{if } \Gamma/\Gamma_{\text{ad}} > \Lambda_0 \\ \Lambda_{k+1}e^{-z_k/z_{k+1}}, & \text{otherwise} \end{cases}, \quad (12)$$

where $\Gamma = -\partial T/\partial z$. In the first term of Equation (11), the density dependence represents the correlation of eddy diffusion with breaking gravity waves in terrestrial atmospheres (Lindzen & Forbes 1983; Izakov 2001), and the exponential decay term allows the reduction in eddy diffusion as the gravity wave amplitude decreases to zero around pressure P_0 . We do not calculate molecular diffusion in our climate model, but this is calculated in the photochemical model. The second term in Equation (11) is dependent on stability and includes additional eddy diffusion in neutral and unstable conditions, such as in Earth's troposphere. Equation (12) slowly reduces the contribution of stability in the transition between unstable and stable regions. The overall profile is then consistent with Earth examples in Massie & Hunten (1981) and Brasseur & Solomon (2006), and with the eddy diffusion profiles assumed in exoplanet photochemical-kinetics studies by other authors (e.g., Segura et al. 2007; Hu et al. 2012). The evolved environments we simulate have thick atmospheres and no oceans and therefore are more like Mars and Venus, whose eddy diffusivities are well modeled by

breaking gravity waves alone (Izakov 2001), so in those cases $\Lambda = 0$. See Table 5 for nominal values.

In stable conditions, the eddy diffusion coefficient for heat is reduced compared to that for momentum (e.g., Kondo et al. 1978). This reduction occurs gradually as a function of stability; Kondo et al. (1978) provided a fit based on Richardson number (Ri). However, our mixing length code cannot compute Ri in the free atmosphere, because it does not include an explicit description of the vertical shear in horizontal wind, so we use $\Gamma/\Gamma_{\text{ad}}$ as a representative stability parameter for this purpose and reduce the eddy diffusion coefficient for heat by

$$K_h = f_h K_m e^{-\alpha\Gamma/\Gamma_{\text{ad}}}, \quad (13)$$

where we set

$$\alpha \equiv \frac{1}{2} \ln \left(\frac{f_{\min}}{f_{\max}} \right), \quad (14)$$

$$f_h \equiv f_{\max} e^{\alpha}. \quad (15)$$

The minimum and maximum scalings from K_m to K_h are denoted by f_{\min} and f_{\max} , respectively, and given in Table 5.

Equations (5)–(11) are composed almost entirely of fundamental physical properties of the local atmospheric conditions: pressure, temperature, density, gravity, and specific heat capacity. Since the vertical transport of heat, mass, and momentum in terrestrial exoplanet atmospheres is generally unknown, we chose to use this physically motivated approach to convection, rather than convective adjustment to a prespecified lapse rate that can be different from the adiabatic lapse rate (e.g., Earth is $\sim 6.5 \text{ K km}^{-1}$, Mars $\sim 2.5 \text{ K km}^{-1}$, and Venus $\sim 8.0 \text{ K km}^{-1}$; Catling & Kasting 2017). The parameterizations we have chosen are able to reproduce eddy diffusion coefficients for mass consistent with measurements and kinetics studies of Earth and Venus (see Figure 21).

A.3. Condensation and Kinematic Mixing

To simulate a potentially habitable, ocean-covered (aqua) planet, we implemented an option for latent heat exchange and kinematic mixing of a condensable gas. The layer-by-layer vertical mixing of a condensable species is calculated by

Table 5
Adjustable Convection Model Parameters

| Parameter | O ₂ -dominated | Venus-like | Aqua planet | Description |
|---|---------------------------|------------------|------------------|--|
| f_z | 0.01 | 0.01 | 0.01 | Mixing length fraction |
| U [m s ⁻¹] | 0.1 | 0.1 | 10 | Surface wind speed |
| z_0 [m] | 0.005 | 0.005 | 0.0002 | Surface roughness length |
| ρ_0 [kg m ⁻³] | 1 | 1 | 1 | Baseline density for eddy diffusion |
| P_0 [Pa] | 1 | 1 | 1 | Pressure for breaking of gravity waves in eddy diffusion |
| $K_{m,0}$ [m ² s ⁻¹] | 0.5 | 1.0 | 0.5 | Eddy scaling coefficient for mass, gravity waves |
| $K_{m,1}$ [m ² s ⁻¹] | ... | ... | 20 | Eddy scaling coefficient for mass, stability |
| $K_{m,1}$ [m ² s ⁻¹] | ... | 0.5 | ... | Constant minimal eddy diffusion |
| Λ_0 | ... | ... | 0.1 | Minimum stability factor |
| f_{\min} | 10 ⁻⁴ | 10 ⁻⁴ | 10 ⁻⁴ | Minimum stability scaling factor for heat |
| f_{\max} | 0.15 | 0.15 | 0.15 | Maximum stability scaling factor for heat |

solving the continuity-transport equation in 1D:

$$\frac{\partial r}{\partial t} = -\frac{1}{\rho} \frac{\partial F_m}{\partial z}, \quad (16)$$

where the kinematic flux is given by

$$F_m = -\rho K_m \frac{\partial r}{\partial z}. \quad (17)$$

Here, K_m is the eddy diffusion coefficient for mass transport, and r is the mixing ratio of the condensable species. As a result of either radiative cooling or an upwelling condensable species, a gas may become supersaturated (i.e., when the partial pressure at a level exceeds the saturation vapor pressure). We assume sufficient cloud condensation nuclei such that any condensate above the saturation point condenses immediately (i.e., within a single time step). The saturated mass mixing ratio is determined by

$$r_{\text{sat}} = \frac{\mu}{\mu_{\text{atm}}} \frac{P_{\text{sat}}}{P}. \quad (18)$$

At the globally averaged temperatures, it is unlikely that the globally averaged water mixing ratios will approach saturation, though there is nonetheless condensation, evaporation, and latent heat exchange. The simplest solution here is to use a different mixing ratio criterion for saturation. We compute condensation if relative humidity exceeds that maximum humidity using a modified form of Equation (2) from Manabe & Wetherald (1967) for Earth:

$$rh = rh_s \max\left(\frac{p/p_s - 0.02}{1 - 0.02}, 0.2\right), \quad (19)$$

where s refers to the surface value. The modification is our specification of a minimum value that depends on the surface humidity (Manabe & Wetherald 1967 made a similar adjustment to obtain Earth's stratospheric H₂O abundance). While Manabe & Wetherald (1967) use $rh_s = 0.77$, we find that $rh_s = 0.70$ matches our globally averaged Earth data best (see Appendix C).

To determine the heating rate due to condensation, we evaluate the conserved quantity, the specific moist enthalpy:

$$h = (c_p r_a + c_{p,v} r_v + c_{p,c} r_c) T + L r_v, \quad (20)$$

where the subscript c refers to the condensed form, v refers to the vapor phase of the condensable, a refers to the vapor-phase bulk atmosphere, and L is the latent heat of evaporation. The expansion of the layer reduces the net latent heat, as a result of isobaric work (PdV), which per unit mass is equivalent to $(R/\mu) dT$. Including this term with the change in specific moist enthalpy due to a change in condensate and the resultant temperature change, and then solving for the change in temperature of the air parcel, we find the net heating rate during time step Δt is

$$q_{\text{lh}} = \frac{\Delta T}{\Delta t} = \frac{\Delta r_c}{\Delta t} \frac{L - T(c_{p,c} - c_{p,v})}{c_p(1 - r_v - r_c) + c_{p,v}r_v + c_{p,c}r_c - R/\mu}, \quad (21)$$

where the quantity being condensed is $\Delta r_c \equiv r_c - r_{\text{sat}}$, r is the mass mixing ratio, and c_p is the specific heat.

4.4. Surface Fluxes

We compute the surface fluxes of sensible heat, latent heat, and condensable gas using similarity theory (e.g., Pierrehumbert 2011, pp. 395–409), given by

$$F_{c,\text{sh}} = \rho c_p C_D U (T_s - T_{\text{sbl}}) \quad (22)$$

$$F_{c,\text{lh}} = \rho L C_D U (r_s - r) \quad (23)$$

$$F_m = \rho C_D U (r_s - r), \quad (24)$$

where U is the surface wind speed, T_s is the temperature of the surface, T_{sbl} is the temperature of the surface atmospheric boundary layer, r_s is the surface mixing ratio boundary condition (determined from a humidity assumption or fixed mixing ratio), and C_D is the coefficient of drag at the surface, which we calculate as in Pierrehumbert (2011):

$$C_D = \left(\frac{k}{\log z/z_0} \right)^2, \quad (25)$$

where z_0 is the surface roughness height, which we specify as 0.005 m for the desiccated planets (corresponding to flatlands with no vegetation) and 0.0002 m for open ocean (Davenport et al. 2000; Jarraud 2008). As the atmospheres are much thicker than Earth, we assume surface wind speeds of 0.1 m s⁻¹, much less than on Earth but consistent with measurements of Venus's

surface atmosphere (Ainsworth & Herman 1975; Counselman et al. 1979). For the aqua planet, we use 10 m s^{-1} , which is roughly consistent with Earth’s global-average wind speed (7 m s^{-1} ; Meissner et al. 2001).

A.5. Aerosols

We include the radiative effects of aerosols in cloudy cases for both the aqua planet and Venus-like atmospheres. Since this is a 1D climate model, we present end-member cases of global clear and cloudy cases, which can be used to assess the observational discriminants of these atmospheres. We have not yet implemented a cloud microphysics model in our climate model, so we specify altitude-dependent differential optical depths and aerosol optical properties from Earth or Venus, as appropriate. Aerosol parameters are described in Section 2.6.3.

A.6. Convergence

We first approach convergence using four-stream radiative transfer for a single global-average-approximation solar zenith angle of $\sim 60^\circ$. The final convergence of VPL Climate is conducted using eight-stream radiative transfer with four-point Gaussian quadrature integration of the stellar radiance, which increases the accuracy of the convergence result (Cronin 2014; Hogan & Hirahara 2015). In future work, we will quantitatively assess the impact of solar radiance integration in our climate model. Kitzmann (2016) determined that increasing the number of radiative transfer streams from eight to 16 had no effect on the radiative fluxes.

Appendix B Photochemical Model Updates

Here we describe several updates made to our photochemical model to allow more robust modeling of the alien environments in this paper. We modified the wavelength grid to accommodate an input SED with wavelengths shorter than Ly α and have increased the resolution to 100 cm^{-1} , which now includes 750 flux bins versus the standard 118. We updated cross sections for the molecules listed in Table 6. Additionally, based on the recommendations in Burkholder et al. (2015), we updated the quantum yields of O₃ with fits by Matsumi et al. (2002) and Nishida et al. (2004). These updates extended the O₃ photochemistry to the cooler temperatures necessary for modeling the range of planets in this work.

We made several other changes to the photochemical model for this work. First, as a result of the cross sections and grid update, we set the solar zenith angle to the daytime mean of 60° to approximate the global diurnal average when using a two-stream radiative transfer model (e.g., Manabe & Strickler 1964; Li 2017). For the evolved atmospheres, we modified treatment of the water vapor profile so that it was no longer specified to a fixed humidity, moist adiabat, or Earth-like profile, but instead was treated like every other long-lived trace species. This is a requirement to be able to model atmospheres with water abundances significantly less than the Earth’s and is required for modeling a Venus-like atmosphere. Likewise, we also treated CO₂ as a long-lived gas, as in Kopparapu et al. (2011), rather than treating it as an inert species (c.f. Meadows et al. 2018a), though condensation limits still apply. Long-lived gases are included in the Jacobian solved at each time step, and transport between layers is calculated. This modification allowed us to more accurately model the photolysis and longer recombination

Table 6
Updated UV–Visible Cross Sections

| Species | Wavelengths (nm) | References |
|---------------------------------|------------------|----------------------------|
| CO ₂ | 121–169 | Lewis & Carver (1983) |
| | 169–200 | Shemansky (1972) |
| | 200–225 | Power law extrapolation |
| H ₂ O | 120–194 | Mota et al. (2005) |
| | 125–190 | Schürgers & Welge (1968) |
| | 190–350 | Sander et al. (2011) |
| H ₂ O ₂ | 350–557 | Power law extrapolation |
| | 120–160 | Feng et al. (1999) |
| | 160–260 | Wu & Chen (1998) |
| H ₂ S | 260–313 | Power law extrapolation |
| | 120–200 | Lane & Kjaergaard (2008) |
| | 512–745 | Mills et al. (2005) |
| H ₂ SO ₄ | 120–226 | Cooper et al. (1996) |
| | 226–375 | Sander et al. (2011) |
| | 120–184 | Power law extrapolation |
| H ₂ CO | 184–396 | Sander et al. (2011) |
| | 120–192 | Suto & Lee (1984) |
| | 192–350 | Burkholder et al. (1993) |
| NO | 120–207 | Iida et al. (1986) |
| | 120–422 | Vandaele et al. (1998) |
| N ₂ O | 120–160 | QY: Sander et al. (2011) |
| | 160–240 | Zelikoff et al. (1953) |
| | 200–420 | Sander et al. (2011) |
| N ₂ O ₅ | 152–200 | Osborne et al. (2000) |
| | 120–179 | Sander et al. (2011) |
| | 179–203 | Lu et al. (2010) |
| O ₂ | 205–240 | Yoshino et al. (1992) |
| | 120–845 | Yoshino et al. (1988) |
| | 120–210 | Serdychenko et al. (2011) |
| OCS | 210–300 | Limão-Vieira et al. (2015) |
| | 120–403 | Molina et al. (1981) |
| SO ₂ | 403–500 | Manatt & Lane (1993) |
| | 120–140 | Power law extrapolation |
| | 140–180 | Power law extrapolation |
| SO ₃ | 180–330 | Hintze et al. (2003) |
| | 330–350 | Sander et al. (2011) |
| | 350–475 | Power law extrapolation |
| S ₃ | 425–575 | Billmers & Smith (1991) |
| S ₄ | 120–153 | Billmers & Smith (1991) |
| CH ₄ | 205–295 | Lee et al. (2001) |
| CH ₃ O ₂ | 210–405 | Sander et al. (2011) |
| CH ₃ OOH | 120–135 | Sander et al. (2011) |
| HCl | 135–220 | Brion et al. (2005) |
| CIO | 236–312 | Cheng et al. (2002) |
| OCIO | 125–183 | Simon et al. (1990) |
| COCl ₂ | 290–460 | Hubinger & Nee (1994) |
| | 168–305 | Bogumil et al. (2003) |
| SO ₂ Cl ₂ | 190–300 | Sander et al. (2011) |
| | | Uthman et al. (1978) |

Note. Most data were obtained from the MPI-Mainz UV/VIS Spectral Atlas of Gaseous Molecules of Atmospheric Interest (Keller-Rudek et al. 2013, http://satellite.mpic.de/spectral_atlas).

lifetimes of CO₂ in desiccated atmospheres, where CO₂ photolysis can outpace recombination, resulting in a steady-state equilibrium between CO₂, CO, O₂, and O₃ (Gao et al. 2015). Lastly, we adjusted the grid spacing for the atmospheric scale heights necessary to model each planet. Since we used 200 constant-thickness layers with altitude-based grid spacing in the chemistry model and VPL Climate uses a variable grid, we interpolated the atmospheric structure values when passing data from one model to the other. Both model grids extend to 0.01 Pa.

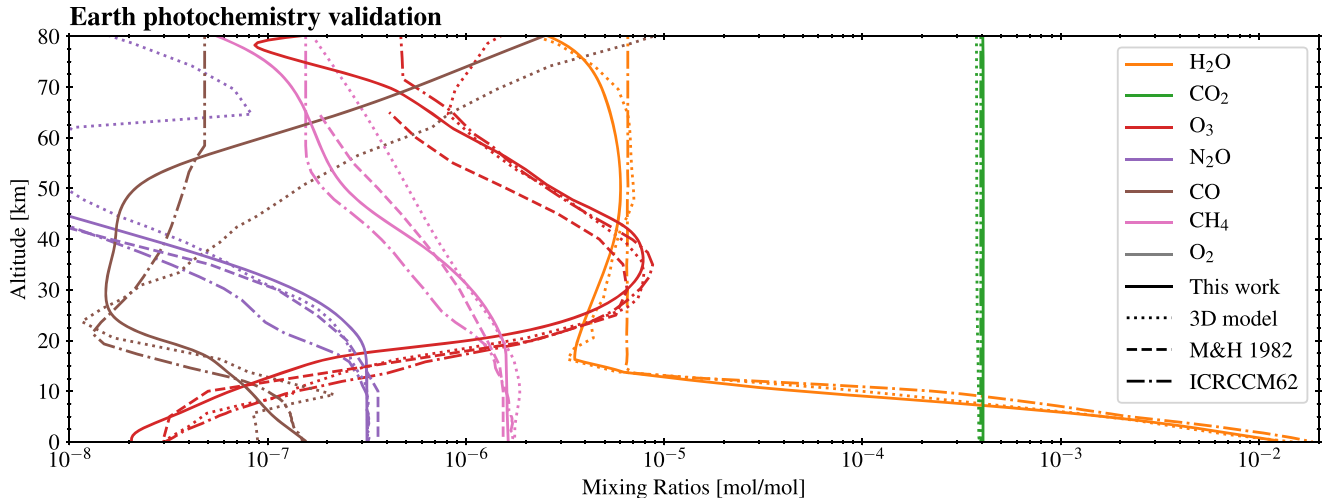


Figure 22. Photochemical equilibrium validation for Earth. Mixing ratio profiles of key species are shown from this work (solid lines), an average derived from the 3D Spectral Earth model (Robinson et al. 2011; dotted lines), measurements from Massie & Hunten (1981; dashed lines), and the ICRCCM Earth midlatitude summer sounding case 62 (dashed-dotted lines).

Appendix C Photochemical Validation of Earth and Venus

With the updates presented in the preceding appendix, we present a new validation of Earth’s and Venus’s atmospheres.

C.1. Earth

In addition to the updates presented in the preceding appendix, we validated Earth using the boundary conditions given in Table 7. In particular, this includes fluxes (not fixed mixing ratios) of the important Earth constituents CO, CH₄, NO, H₂S, H₂SO₄, OCS, N₂O, CS₂, and dimethyl sulfide (C₂H₆S), along with vertically distributed fluxes of SO₂. Oxygen is fixed at the surface at 21% and nitrogen at 78%. Carbon dioxide is fixed at the surface to the current value of 400 ppm. The flux of NO is calibrated to best reproduce the effects of NO_x chemistry, as we do not include chlorine species or other pollutants not listed here. The water vapor profile is from Manabe & Wetherald (1967) using a fixed surface humidity of 70%, assuming the tropopause is at 14 km and that the minimum saturation value in the troposphere is 20% of the surface value. Vertical profiles of important species are shown in Figure 22 along with several sources for comparison.

C.2. Venus

This is the first time our photochemical model has been used for a Venus-like planet. This has required careful selection of boundary conditions, reactions, and the eddy diffusion profile. Specifically for Venus, few additional changes were required to the model itself. In addition to the model updates listed in Appendix B, we updated saturation vapor pressure data, added an additional lower boundary condition, compiled a new Venus input template, and conducted a validation against recent Venus literature.

We updated the saturation vapor pressure and temperature data for sulfuric acid solutions using finer intervals of 1% by fitting splines to published refraction and absorption data, which are available at sulfuric acid concentrations of 25, 38, 50, 75, 84.5, and 95.6% (Palmer & Williams 1975).

Table 7
Earth Validation Lower Boundary Conditions

| Species | Boundary condition |
|--------------------------------------|---|
| O | $v_{\text{dep}} = 1$ |
| O ₂ | $r_0 = 0.21$ |
| H ₂ O | $rh_0 = 0.70$ |
| H | $v_{\text{dep}} = 1$ |
| OH | $v_{\text{dep}} = 1$ |
| HO ₂ | $v_{\text{dep}} = 1$ |
| H ₂ O ₂ | $v_{\text{dep}} = 0.2$ |
| H ₂ | $v_{\text{dep}} = 2.4 \times 10^{-4}$ |
| CO | $v_{\text{dep}} = 0.03, F = 3.7 \times 10^{11}$ |
| HCO | $v_{\text{dep}} = 1$ |
| H ₂ CO | $v_{\text{dep}} = 0.2$ |
| CH ₄ | $F = 1.6 \times 10^{11}$ |
| NO | $v_{\text{dep}} = 1.6 \times 10^{-2}, F = 1.0 \times 10^9$ |
| NO ₂ | $v_{\text{dep}} = 3.0 \times 10^{-3}$ |
| HNO | $v_{\text{dep}} = 1$ |
| H ₂ S | $v_{\text{dep}} = 0.02, F = 2.0 \times 10^8$ |
| SO ₂ | $v_{\text{dep}} = 1, F = 9.0 \times 10^9 \text{ dist. 14 km}$ |
| H ₂ SO ₄ | $v_{\text{dep}} = 1, F = 7.0 \times 10^8$ |
| HSO | $v_{\text{dep}} = 1$ |
| OCS | $v_{\text{dep}} = 0.01, F = 1.5 \times 10^7$ |
| HNO ₃ | $v_{\text{dep}} = 0.2$ |
| N ₂ O | $F = 1.53 \times 10^9$ |
| HO ₂ NO ₂ | $v_{\text{dep}} = 0.2$ |
| CO ₂ | $r_0 = 4.0 \times 10^{-4}$ |
| CS ₂ | $F = 2.0 \times 10^7$ |
| C ₂ H ₆ S(DMS) | $F = 3.3 \times 10^9$ |
| N ₂ | $r_0 = 0.78$ |

Notes. All unlisted species have a lower boundary condition $v_{\text{dep}} = 0$. Deposition velocities (v_{dep}) are given in cm s^{-1} , fluxes (F) are given in $\text{molecules cm}^{-2} \text{s}^{-1}$, r_0 is a fixed surface mixing ratio, and rh_0 is the surface relative humidity.

We drew heavily on recent Venus literature (primarily Krasnopolsky 2012; Zhang et al. 2012) to construct our Venus template, consisting of important species, their boundary conditions, and relevant reactions. The boundary conditions are

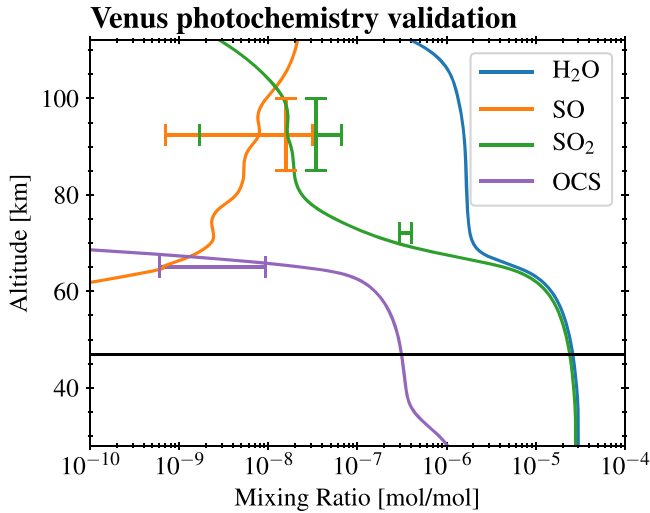


Figure 23. Photochemical equilibrium validation for Venus. Mixing ratios from our model for select species are shown, along with a selection of published measurements. Note that there is considerable variation in these abundances as a function of day vs. night and latitude (e.g., Ignatiev et al. 1999; Arney et al. 2014).

Table 8
Venus Validation Lower Boundary Conditions

| Species | Boundary condition |
|------------------|----------------------------|
| O ₂ | $v_{\text{dep}} = 2v$ |
| H ₂ O | $r_0 = 3.0 \times 10^{-5}$ |
| H ₂ | $r_0 = 4.5 \times 10^{-9}$ |
| NO | $r_0 = 5.5 \times 10^{-9}$ |
| SO ₂ | $r_0 = 2.8 \times 10^{-5}$ |
| OCS | $r_0 = 1.0 \times 10^{-6}$ |
| HCl | $r_0 = 4.0 \times 10^{-7}$ |
| CO ₂ | $r_0 = 0.965$ |
| N ₂ | $r_0 = 0.035$ |

Notes. All unlisted species have a lower boundary condition $v_{\text{dep}} = v = K_m/2H$. Boundary conditions are either deposition velocities (v_{dep}), given in cm s^{-1} , or a fixed surface mixing ratio r_0 . The Venus lower boundary is at 28 km (~ 11.5 bar).

listed in Table 8. As in previous work (e.g., Krasnopolsky 2012; Zhang et al. 2012), we do not extend our photochemical template for Venus to the surface. Instead, we set the lower boundary at 28 km (~ 11.5 bar), as we do not include thermochemical reactions, which are typically treated as a separate regime from the photochemical region (e.g., Krasnopolsky 2013). Because the lower boundary is not the surface, the “deposition velocity” v depends on the scale height and eddy diffusion coefficient (Krasnopolsky 2012):

$$v = \frac{K_m}{2H}, \quad (26)$$

so the model can calculate the associated downward flux. The reactions in our Venus template are primarily reproduced from those given in Krasnopolsky (2012).

The validation for Venus was primarily for major climate and observable species, particularly those involving Venus’s sulfuric acid clouds (e.g., H₂O and SO₂; see Figure 23). We find good agreement with recent modeling by Krasnopolsky (2012), on which our reaction and boundary condition template

is based. However, there are still disagreements between Venus photochemical modeling in the literature among the abundances retrieved from different observations, particularly observed oxygen abundances and in the features of the SO₂ profile. Future improvements to our Venus reactions can be made as those researchers who focus on Venus solve these outstanding issues.

Our photochemical model includes simplistic aerosol formation, including sulfuric acid aerosols, based on production/loss lifetimes (Pavlov et al. 2001). We found this model fails to produce the specific distribution of the multiple aerosol modes of Venus and is unable to generate aerosols as large as the mode 3 ($3.85 \mu\text{m}$) particles. Nonetheless, it does self-consistently generate aerosols at altitudes consistent with the cloud deck of Venus. We find that the transmission spectrum for our model Venus is roughly consistent with the cloud parameterization from Crisp (1986). Therefore, this provides an acceptable starting point for self-consistent climate–chemistry modeling of Venus-like exoplanets with aerosol formation.

ORCID iDs

- Andrew P. Lincowski [ID](https://orcid.org/0000-0003-0429-9487) <https://orcid.org/0000-0003-0429-9487>
 Victoria S. Meadows [ID](https://orcid.org/0000-0002-1386-1710) <https://orcid.org/0000-0002-1386-1710>
 David Crisp [ID](https://orcid.org/0000-0002-4573-9998) <https://orcid.org/0000-0002-4573-9998>
 Tyler D. Robinson [ID](https://orcid.org/0000-0002-3196-414X) <https://orcid.org/0000-0002-3196-414X>
 Rodrigo Luger [ID](https://orcid.org/0000-0002-0296-3826) <https://orcid.org/0000-0002-0296-3826>
 Jacob Lustig-Yaeger [ID](https://orcid.org/0000-0002-0746-1980) <https://orcid.org/0000-0002-0746-1980>
 Giada N. Arney [ID](https://orcid.org/0000-0001-6285-267X) <https://orcid.org/0000-0001-6285-267X>

References

- Ainsworth, J. E., & Herman, J. R. 1975, *JGR*, **80**, 173
 Airapetian, V. S., Glocer, A., Gronoff, G., Hébrard, E., & Danchi, W. 2016, *NatGe*, **9**, 452
 Airapetian, V. S., Glocer, A., Khazanov, G. V., et al. 2017, *ApJL*, **836**, L3
 Alberti, T., Carbone, V., Lepreti, F., & Vecchio, A. 2017, *ApJ*, **844**, 19
 Allen, M., Yung, Y. L., & Waters, J. W. 1981, *JGR*, **86**, 3617
 André, J., & Mahrt, L. 1982, *JAtS*, **39**, 864
 Anglada-Escudé, G., Amado, P. J., Barnes, J., et al. 2016, *Natur*, **536**, 437
 Arney, G., Domagal-Goldman, S. D., Meadows, V. S., et al. 2016, *AsBio*, **16**, 873
 Arney, G., Meadows, V., Crisp, D., et al. 2014, *JGRE*, **119**, 1860
 Arney, G. N., Meadows, V. S., Domagal-Goldman, S. D., et al. 2017, *ApJ*, **836**, 49
 Baldrige, A. M., Hook, S. J., Grove, C. I., & Rivera, G. 2009, *RSEnv*, **113**, 711
 Ballard, S., & Johnson, J. A. 2016, *ApJ*, **816**, 66
 Baraffe, I., Chabrier, G., Allard, F., & Hauschildt, P. H. 1998, *A&A*, **337**, 403
 Baraffe, I., Homeier, D., Allard, F., & Chabrier, G. 2015, *A&A*, **577**, A42
 Baranov, Y. I., Lafferty, W. J., & Fraser, G. T. 2004, *JMoSp*, **228**, 432
 Barnes, R., Deitrick, R., Luger, R., et al. 2018, arXiv:1608.06919v2
 Baum, B. A., Yang, P., Heymsfield, A. J., et al. 2005, *JApMe*, **44**, 1896
 Belviso, S., Nguyen, B. C., & Allard, P. 1986, *GeoRL*, **13**, 133
 Berta-Thompson, Z. K., Irwin, J., Charbonneau, D., et al. 2015, *Natur*, **527**, 204
 Billmers, R. I., & Smith, A. L. 1991, *JPhCS*, **95**, 4242
 Blackadar, A. K. 1962, *JGR*, **67**, 3095
 Bogumil, K., Orphal, J., Homann, T., et al. 2003, *J. Photochem. Photobio. A: Chem.*, **157**, 167
 Bolmont, E., Selsis, F., Owen, J. E., et al. 2017, *MNRAS*, **464**, 3728
 Bourrier, V., Ehrenreich, D., Wheatley, P. J., et al. 2017, *A&A*, **599**, L3
 Brasseur, G. P., & Solomon, S. 2006, *Aeronomy of the Middle Atmosphere: Chemistry and Physics of the Stratosphere and Mesosphere*, Vol. 32 (Berlin: Springer)

- Brion, C., Dyck, M., & Cooper, G. 2005, *JESRP*, 144, 127
- Bullock, M. A., & Grinspoon, D. H. 2001, *Icar*, 150, 19
- Bullock, M. A., & Grinspoon, D. H. 2013, in Comparative Climatology of Terrestrial Planets Vol. 1, ed. S. J. Mackwell et al. (Tucson, AZ: Univ. Arizona Press), 19
- Burgasser, A. J., & Mamajek, E. E. 2017, *ApJ*, 845, 110
- Burkholder, J., Sander, S., Abbatt, J., et al. 2015, NASA Panel for Data Evaluation, Tech. Rep. 18
- Burkholder, J. B., Talukdar, R. K., Ravishankara, A. R., & Solomon, S. 1993, *JGR*, 98, 22937
- Burton, M. R., Oppenheimer, C., Horrocks, L. A., & Francis, P. W. 2000, *Geo*, 28, 915
- Canuto, V. M., Cheng, Y., Howard, A. M., & Esau, I. N. 2008, *JAtS*, 65, 2437
- Carn, S. A., Fioletov, V. E., McLinden, C. A., Li, C., & Krotkov, N. A. 2017, *NatSR*, 7, 44095
- Catling, D. C., & Kasting, J. F. 2017, Atmospheric Evolution on Inhabited and Lifeless Worlds (Cambridge: Cambridge Univ. Press)
- Catling, D. C., Krissansen-Totton, J., Kiang, N. Y., et al. 2018, *AsBio*, 18, 709
- Charnay, B., Meadows, V., & Leconte, J. 2015, *ApJ*, 813, 15
- Cheng, B.-M., Chung, C.-Y., Bahou, M., Lee, Y.-P., & Lee, L. 2002, *JChPh*, 117, 4293
- Chyba, C. F. 1990, *Natur*, 343, 129
- Clark, R. N., Swayze, G. A., Wise, R., et al. 2007, US Geological Survey, Digital Data Series, 231, <https://speclab.cr.usgs.gov/spectral.lib06/>
- Coleman, G. A. L., Nelson, R. P., Paardekooper, S. J., et al. 2017, *MNRAS*, 467, 996
- Collinson, G. A., Frahm, R. A., Glocer, A., et al. 2016, *GeoRL*, 43, 5926
- Cooper, G., Anderson, J. E., & Brion, C. E. 1996, *CP*, 209, 61
- Counselman, C. C., Gourevitch, S. A., King, R. W., Loriot, G. B., & Prinn, R. G. 1979, *Sci*, 205, 85
- Cowan, N. B., Greene, T., Angerhausen, D., et al. 2015, *PASP*, 127, 311
- Crisp, D. 1986, *Icar*, 514, 484
- Crisp, D. 1997, *GeoRL*, 24, 571
- Cronin, T. W. 2014, *JAtS*, 71, 2994
- Davenport, A. G., Grimmond, C. S. B., Oke, T. R., & Wieringa, J. 2000, in Proc. 12th Conf. on Applied Climatology (Asheville, NC: American Meteorological Society), 96
- De Bergh, C., Bezard, B., Owen, T., et al. 1991, *Sci*, 251, 547
- de Wit, J., Wakeford, H. R., Gillon, M., et al. 2016, *Natur*, 537, 69
- de Wit, J., Wakeford, H. R., Lewis, N. K., et al. 2018, *NatAs*, 2, 214
- Delrez, L., Gillon, M., Triaud, A. H. M. J., et al. 2018, *MNRAS*, 475, 3577
- Des Marais, D. J., Harwit, M. O., Jucks, K. W., et al. 2002, *AsBio*, 2, 153
- Dittmann, J. A., Irwin, J. M., Charbonneau, D., et al. 2017, *Natur*, 544, 333
- Donahue, T. M., & Pollack, J. B. 1983, in Venus (A83-37401), ed. D. M. Hunten et al. (Tucson, AZ: Univ. Arizona Press), 1003
- Dong, C., Lingam, M., Ma, Y., & Cohen, O. 2017, *ApJL*, 837, L26
- Dressing, C. D., & Charbonneau, D. 2015, *ApJ*, 807, 45
- Encrenaz, T., DeWitt, C., Richter, M., et al. 2018, *A&A*, 612, A112
- Feng, R., Cooper, G., & Brion, C. E. 1999, *CP*, 244, 127
- Fleming, E. L., Jackman, C. H., Stolarski, R. S., & Considine, D. B. 1999, *JGR*, 104, 23911
- France, K., Froning, C. S., Linsky, J. L., et al. 2013, *ApJ*, 763, 149
- Fujii, Y., Angerhausen, D., Deitrick, R., et al. 2018, *AsBio*, 18, 739
- Fulton, B. J., Petigura, E. A., Howard, A. W., et al. 2017, *AJ*, 154, 109
- Gao, P., Hu, R., Robinson, T. D., Li, C., & Yung, Y. L. 2015, *ApJ*, 806, 249
- Gao, P., Zhang, X., Crisp, D., Bardeen, C. G., & Yung, Y. L. 2014, *Icar*, 231, 83
- Garcia-Sage, K., Glocer, A., Drake, J. J., Gronoff, G., & Cohen, O. 2017, *ApJL*, 844, L13
- Gillon, M., Jehin, E., Lederer, S. M., et al. 2016, *Natur*, 533, 221
- Gillon, M., Triaud, A. H. M. J., Demory, B.-O., et al. 2017, *Natur*, 542, 456
- Godolt, M., Grenfell, J. L., Kitzmann, D., et al. 2016, *A&A*, 592, A36
- Greenblatt, G. D., Orlando, J. J., Burkholder, J. B., & Ravishankara, A. R. 1990, *JGR*, 95, 18577
- Greene, T. P., Line, M. R., Montero, C., et al. 2016, *ApJ*, 817, 17
- Grenfell, J. L., Gebauer, S. V., Paris, P., Godolt, M., & Rauer, H. 2014, *P&SS*, 98, 66
- Grenfell, J. L., Stracke, B., von Paris, P., et al. 2007, *P&SS*, 55, 661
- Grimm, S. L., Demory, B.-o., Gillon, M., et al. 2018, *A&A*, 613, A68
- Gruszka, M., & Borysow, A. 1997, *Icar*, 129, 172
- Guzmán-Marmolejo, A., Segura, A., & Escobar-Briones, E. 2013, *AsBio*, 13, 550
- Hale, G. M., & Querry, M. R. 1973, *ApOpt*, 12, 555
- Hamano, K., Abe, Y., & Genda, H. 2013, *Natur*, 497, 607
- Hashimoto, G. L., Abe, Y., & Sasaki, S. 1997, *GeoRL*, 24, 289
- Henry, T. J., Jao, W.-C., Subasavage, J. P., et al. 2006, *AJ*, 132, 2360
- Hermans, C., Vandaele, A. C., Carleer, M., et al. 1999, *Environ. Sci. Pollut. Res.*, 6, 151
- Hinson, D. P., & Wilson, R. J. 2004, *JGRE*, 109, E01002
- Hintze, P. E., Kjaergaard, H. G., Vaida, V., & Burkholder, J. B. 2003, *JPCA*, 107, 1112
- Hirono, M., & Nakazawa, T. 1982, *JPSJ*, 51, 265
- Hodges, R. 1969, *JGR*, 74, 4087
- Hogan, R. J., & Hirahara, S. 2015, *GeoRL*, 43, 482
- Hu, R., Cahoy, K., & Zuber, M. T. 2012, *JGR*, 117, E07002
- Hu, R., & Seager, S. 2014, *ApJ*, 784, 63
- Hu, Y., & Yang, J. 2014, *PNAS*, 111, 629
- Huang, X., Schwenke, D. W., Freedman, R. S., & Lee, T. J. 2017, *JQSRT*, 203, 224
- Hubinger, S., & Nee, J. 1994, *CP*, 181, 247
- Hunten, D. M. 1973, *JAtS*, 30, 1481
- Hunten, D. M. 1975, *PNAS*, 72, 4711
- Hunten, D. M. 1982, *P&SS*, 30, 773
- Ignatiev, N. I., Moroz, V. I., Zasova, L. V., & Khatuntsev, I. V. 1999, *P&SS*, 47, 1061
- Iida, Y., Carnovale, F., Daviel, S., & Brion, C. E. 1986, *CP*, 105, 211
- Izakov, M. N. 2001, *P&SS*, 49, 47
- Jarraud, M. 2008, Guide to Meteorological Instruments and Methods of Observation, WMO-No. 8 (Geneva: World Meteorological Organisation)
- Johnston, H. S., Serang, O., & Podolske, J. 1979, *JGR*, 84, 5077
- Kane, S. R., Kopparapu, R. K., & Domagal-Goldman, S. D. 2014, *ApJL*, 794, L5
- Kasting, J. F. 1995, *P&SS*, 43, 11
- Kasting, J. F., Liu, S. C., & Donahue, T. M. 1979, *JGR*, 84, 3097
- Kasting, J. F., Pollack, J. B., & Ackerman, T. P. 1984, *Icar*, 57, 335
- Kasting, J. F., Whitmire, D. P., & Reynolds, R. T. 1993, *Icar*, 101, 108
- Keller-Rudek, H., Moortgat, G. K., Sander, R., & Sørensen, R. 2013, *ESSD*, 5, 365
- Kerzhanovich, V. V., & Marov, M. I. 1983, in Venus (A83-37401 17-91), ed. D. M. Hunten et al. (Tucson, AZ: Univ. Arizona Press), 766
- Khodachenko, M. L., Ribas, I., Lammer, H., et al. 2007, *AsBio*, 7, 167
- Kitzmann, D. 2016, *ApJL*, 817, L18
- Kondo, J., Kanechika, O., & Yasuda, N. 1978, *JAtS*, 35, 1012
- Kopparapu, R. K., Kasting, J. F., & Zahnle, K. J. 2011, *ApJ*, 745, 77
- Kopparapu, R. K., Ramirez, R., Kasting, J. F., et al. 2013, *ApJ*, 765, 131
- Kopparapu, R. K., Wolf, E. T., Haqq-Misra, J., et al. 2016, *ApJ*, 819, 84
- Kral, Q., Wyatt, M. C., Triaud, A. H. M. J., et al. 2018, *MNRAS*, 479, 2649
- Krasnopolsky, V. A. 2012, *Icar*, 218, 230
- Krasnopolsky, V. A. 2013, *Icar*, 225, 570
- Krasnopolsky, V. A. 2015, *Icar*, 252, 327
- Krasnopolsky, V. A., & Parshev, V. A. 1983, in Venus, ed. D. M. Hunten et al. (Tucson, AZ: Univ. Arizona Press), 461
- Krissansen-Totton, J., Bergsman, D. S., & Catling, D. C. 2016, *AsBio*, 16, 39
- Lafferty, W. J., Solodov, A. M., Weber, A., Olson, W. B., & Hartmann, J.-M. 1996, *ApOpt*, 35, 5911
- Lammer, H., Kislyakova, K. G., Odert, P., et al. 2011, *OLEB*, 41, 503
- Lammer, H., Lichtenegger, H. I. M., Kulikov, Y. N., et al. 2007, *AsBio*, 7, 185
- Lane, J. R., & Kjaergaard, H. G. 2008, *JPCA*, 112, 4958
- Lee, A. Y. T., Yung, Y. L., Cheng, B.-M., et al. 2001, *ApJL*, 551, L93
- Lee, Y. J., Sagawa, H., Haus, R., et al. 2016, *JGRE*, 121, 1737
- Lewis, B. R., & Carver, J. H. 1983, *JQSRT*, 30, 297
- Li, J. 2017, *JAtS*, 74, 1669
- Liebert, J., & Gizis, J. E. 2006, *PASP*, 118, 659
- Limão-Vieira, P., Ferreira da Silva, F., Almeida, D., et al. 2015, *JChPh*, 142, 064303
- Lindzen, R., & Forbes, J. 1983, *JGRC*, 88, 6549
- Line, M. R., Wolf, A. S., Zhang, X., et al. 2013, *ApJ*, 775, 137
- Lovis, C., Snellen, I., Mouillet, D., et al. 2017, *A&A*, 599, A16
- Lu, H.-C., Chen, H.-K., Chen, H.-F., Cheng, B.-M., & Ogilvie, J. 2010, *A&A*, 520, A19
- Luger, R., & Barnes, R. 2015, *AsBio*, 15, 119
- Luger, R., Barnes, R., Lopez, E., et al. 2015, *AsBio*, 15, 57
- Luger, R., Lustig-Yaeger, J., Fleming, D. P., et al. 2017a, *ApJ*, 837, 63
- Luger, R., Sestovic, M., Kruse, E., et al. 2017b, *NatAs*, 1, 0129
- Manabe, S., & Strickler, R. F. 1964, *JAtS*, 21, 361
- Manabe, S., & Wetherald, R. T. 1967, *JAtS*, 24, 241
- Manatt, S. L., & Lane, A. L. 1993, *JQSRT*, 50, 267
- Massie, S. T., & Hunten, D. M. 1981, *JGR*, 86, 9859
- Maté, B., Lugez, C., Fraser, G. T., & Lafferty, W. J. 1999, *JGRD*, 104, 30585
- Matsumi, Y., Comes, F. J., Hancock, G., et al. 2002, *JGRD*, 107, 4024
- Meadows, V. S. 2017, *AsBio*, 17, 10
- Meadows, V. S., Arney, G. N., Schwierman, E. W., et al. 2018a, *AsBio*, 18, 133

- Meadows, V. S., & Barnes, R. K. 2018, in Handbook of Exoplanets, ed. H. J. Deeg & J. A. Belmonte (Cham: Springer), 1, <https://link.springer.com/referencework/10.1007/978-3-319-30648-3>
- Meadows, V. S., & Crisp, D. 1996, *JGR*, 101, 4595
- Meadows, V. S., Reinhard, C. T., Arney, G. N., et al. 2018b, *AsBio*, 18, 630
- Meissner, T., Smith, D., & Wentz, F. 2001, *JGRC*, 106, 11731
- Miller-Ricci, E., Seager, S., & Sasselov, D. 2009, *ApJ*, 690, 1056
- Mills, M. J., Toon, O. B., Vaida, V., et al. 2005, *JGRD*, 110, D08201
- Misra, A., Meadows, V., & Crisp, D. 2014, *ApJ*, 792, 61
- Molina, L. T., Lamb, J. J., & Molina, M. J. 1981, *GeoRL*, 8, 1008
- Moore, J. F. 1972, PhD thesis, Columbia Univ.
- Morley, C. V., Kreidberg, L., Rustamkulov, Z., Robinson, T., & Fortney, J. J. 2017, *ApJ*, 850, 121
- Mota, R., Parafita, R., Giuliani, A., et al. 2005, *CPL*, 416, 152
- Nishida, S., Taketani, F., Takahashi, K., & Matsumi, Y. 2004, *JPCA*, 108, 2710
- Osborne, B. A., Marston, G., Kaminski, L., et al. 2000, *JQSRT*, 64, 67
- Owen, J. E., & Wu, Y. 2013, *ApJ*, 775, 105
- Palmer, K. F., & Williams, D. 1975, *ApOpt*, 14, 208
- Patra, P. K., & Lal, S. 1997, *JASTP*, 59, 1149
- Pavlov, A. A., Brown, L. L., & Kasting, J. F. 2001, *JGRE*, 106, 23267
- Pierrehumbert, R. T. 2011, Principles of Planetary Climate (Cambridge: Cambridge Univ. Press)
- Quanz, S. P., Crossfield, I., Meyer, M. R., Schmalzl, E., & Held, J. 2015, *IJAsB*, 14, 279
- Quarles, B., Quintana, E. V., Lopez, E., Schlieder, J. E., & Barclay, T. 2017, *ApJL*, 842, L5
- Ribas, I., Bolmont, E., Selsis, F., et al. 2016, *A&A*, 596, A111
- Ribas, I., Guinan, E. F., Güdel, M., & Audard, M. 2005, *ApJ*, 622, 680
- Robinson, T. D. 2017, *ApJ*, 836, 236
- Robinson, T. D., & Crisp, D. 2018, *JQSRT*, 211, 78
- Robinson, T. D., Meadows, V. S., Crisp, D., et al. 2011, *AsBio*, 11, 0642
- Rodler, F., & López-Morales, M. 2014, *ApJ*, 781, 54
- Rogers, L. A. 2015, *ApJ*, 801, 41
- Rogers, R., & Yau, M. 1989, *Nat. Philos*, 113, 290
- Rothman, L. S., Gordon, I. E., Babikov, Y., et al. 2013, *JQSRT*, 130, 4
- Rothman, L. S., Gordon, I. E., Barber, R. J., et al. 2010, *JQSRT*, 111, 2139
- Rugheimer, S., Kaltenegger, L., Segura, A., Linsky, J., & Mohanty, S. 2015, *ApJ*, 809, 57
- Sander, S., Friedl, R., Barker, J., et al. 2011, JPL Publication, 15-10
- Schaefer, L., Wordsworth, R. D., Berta-Thompson, Z., & Sasselov, D. 2016, *ApJ*, 829, 63
- Schürgers, M., & Welge, K. H. 1968, *ZNatA*, 23, 1508
- Schieterman, E. W., Kiang, N. Y., Parenteau, M. N., et al. 2018, *AsBio*, 18, 663
- Schieterman, E. W., Meadows, V. S., Domagal-Goldman, S. D., et al. 2016, *ApJL*, 819, L13
- Schieterman, E. W., Robinson, T. D., Meadows, V. S., Misra, A., & Domagal-Goldman, S. 2015, *ApJ*, 810, 57
- Segura, A., Kasting, J. F., Meadows, V., et al. 2005, *AsBio*, 5, 706
- Segura, A., Meadows, V. S., Kasting, J. F., Crisp, D., & Cohen, M. 2007, *A&A*, 472, 665
- Segura, A., Walkowicz, L. M., Meadows, V., Kasting, J., & Hawley, S. 2010, *AsBio*, 10, 751
- Seinfeld, J., & Pandis, S. 2006, Atmospheric Chemistry and Physics (New York: Wiley)
- Selsis, F., Despois, D., & Parisot, J.-P. 2002, *A&A*, 388, 985
- Serdychenko, A., Gorshelev, V., Weber, M., & Burrow, J. P. 2011, *Spectrosc. Eur.*, 23, 14
- Shemansky, D. E. 1972, *JChPh*, 56, 1582
- Shields, A. L., Ballard, S., & Johnson, J. A. 2016, *PhR*, 663, 1
- Shields, A. L., Meadows, V. S., Bitz, C. M., et al. 2013, *AsBio*, 13, 715
- Shvartzvald, Y., Yee, J. C., Calchi Novati, S., et al. 2017, *ApJL*, 840, L3
- Simon, F., Schneider, W., Moortgat, G., & Burrows, J. 1990, *J. Photochem. Photobio. A: Chem.*, 55, 1
- Simончини, Е., Virgo, N., & Kleidon, A. 2013, *ESD*, 4, 317
- Snellen, I., de Kok, R., Birkby, J. L., et al. 2015, *A&A*, 576, A59
- Stamnes, K., Tsay, S. C., Wiscombe, W., & Jayaweera, K. 1988, *ApOpt*, 42, 2502
- Stamnes, K., Tsay, S. C., Wiscombe, W., & Laszlo, I. 2000, DISORT, a General-purpose Fortran Program for Discrete-ordinate-method Radiative Transfer in Scattering and Emitting Layered Media: Documentation of Methodology, <ftp://climate.gsfc.nasa.gov/pub/wiscombe/MultipleScatt/>
- Sullivan, P. W., Winn, J. N., Berta-Thompson, Z. K., et al. 2015, *ApJ*, 809, 77
- Suto, M., & Lee, L. C. 1984, *JChPh*, 81, 1294
- Tange, O. 2011, login: The USENIX Magazine, 36, 42
- Tarter, J. C., Backus, P. R., Mancinelli, R. L., et al. 2007, *AsBio*, 7, 30
- Tian, F. 2015, *E&PSL*, 432, 126
- Tilley, M. A., Segura, A., Meadows, V. S., Hawley, S., & Davenport, J. 2017, arXiv:1711.08484
- Tinetti, G., Meadows, V. S., Crisp, D., et al. 2005, *AsBio*, 5, 461
- Turbet, M., Bolmont, E., Leconte, J., et al. 2018, *A&A*, 612, A86
- Turbet, M., Leconte, J., Selsis, F., et al. 2016, *A&A*, 596, A112
- Unterbörrn, C. T., Desch, S. J., Hinkel, N. R., & Lorenzo, A. 2018, *NatAs*, 2, 297
- Uthman, A., Demlein, P., Allston, T., et al. 1978, *JPhCh*, 82, 2252
- Vandaele, A. C., Hermans, C., Simon, P. C., et al. 1998, *JQSRT*, 59, 171
- Wagner, W., Saul, A., & Pruss, A. 1994, *JPCRD*, 23, 515
- Walker, J. C., Hays, P., & Kasting, J. F. 1981, *JGRC*, 86, 9776
- Walker, S. I., Bains, W., Cronin, L., et al. 2018, *AsBio*, 18, 779
- Wheatley, P. J., Louden, T., Bourrier, V., Ehrenreich, D., & Gillon, M. 2017, *MNRAS*, 465, L74
- Williams, S. N., Schaefer, S. J., Calvache, M. L., & Lopez, D. 1992, *GeCoA*, 56, 1765
- Wofsy, S. C., McConnell, J. C., & McElroy, M. B. 1972, *JGR*, 77, 4477
- Wolf, E. T. 2017, *ApJL*, 839, L1
- Woo, R., & Ishimaru, A. 1981, *Natur*, 289, 383
- Wordsworth, R., Forget, F., & Eymet, V. 2010, *Icar*, 210, 992
- Wordsworth, R. D., Schaefer, L. K., & Fischer, R. A. 2018, *AJ*, 155
- Wu, C. Y. R., & Chen, F. Z. 1998, *JQSRT*, 60, 17
- Yang, J., Boué, G., Fabrycky, D. C., & Abbot, D. S. 2014, *ApJL*, 787, L2
- Yoshino, K., Cheung, A. S.-C., Esmond, J. R., Parkinson, W. H., & Freeman, D. E. 1988, *P&SS*, 36, 1469
- Yoshino, K., Esmond, J. R., Cheung, A. S.-C., Freeman, D. E., & Parkinson, W. H. 1992, *P&SS*, 40, 185
- Zahnle, K., Claire, M., & Catling, D. 2006, *Geobio*, 4, 271
- Zahnle, K. J., & Catling, D. C. 2017, *ApJ*, 843, 122
- Zelikoff, M., Watanabe, K., & Inn, E. C. Y. 1953, *JChPh*, 21, 1643
- Zhang, X., Chang, M., Mills, F. P., Belyaev, D. A., & Yung, Y. L. 2012, *Icar*, 217, 714